Tufts UNIVERSITY | School of Engineering

Convection Heat Transfer in the Presence of Apparent Slip

Submitted by
Lisa Steigerwalt Lam

in partial fulfillment of the requirements for the degree of

Doctor of Philosophy
in
Mechanical Engineering

School of Engineering
Tufts University
Medford, Massachusetts

February 2015

Certified By: _____
Associate Professor Marc Hodes
Tufts University

Committee: _____
Associate Professor Scott MacLachlan
Memorial University

Committee: _____
Dr. Ryan Enright
Bell Labs Ireland, Alcatel-Lucent

Committee: _____
Professor Vincent P. Manno
Olin College of Engineering

Committee: _____
Assistant Professor Jeffrey Guasto
Tufts University

Committee: _____
Assistant Professor Nikhil U. Nair
Tufts University

Abstract

Convection Heat Transfer in the Presence of Apparent Slip

by

Lisa Steigerwalt Lam

Chair: Dr. Marc Hodes

Structured surfaces, e.g., superhydrophobic surfaces or superoleophobic surfaces are a class of surfaces engineered on the micro- and nano-scale that resist wetting and decrease hydrodynamic drag. The capacity to design these surfaces with a variety of textures and coatings continues to develop and they are being considered for a wide variety of application areas ranging from retarding frost formation on airplane wings to drag reduction in microchannel flows. This dissertation addresses four problems related to heat transfer to flows over structured surfaces.

We first investigate the problem of heat transfer in a thermally developing, steady, laminar Couette flow in the presence of hydrodynamic and thermal slip. Fluid temperature at the inlet to a parallel plate channel is prescribed, as are various combinations of isothermal and adiabatic boundary conditions along its surfaces. Analytical expressions incorporating arbitrary slip are developed for temperature profiles, and developing and fully developed Nusselt numbers. Representative results show the presence of thermal slip lowers the Nusselt number relative to the no-slip value.

The second problem we consider is liquid cooling in a microgap lined with microscale

ridges oriented parallel to the flow. Using available expressions for Nusselt number and Poiseuille number as a function of hydrodynamic and thermal slip length, thermal resistance expressions for a Poiseuille flow in a parallel plate channel are developed in order at assess the relative contributions of convection and caloric heat transfer. Water and a liquid metal, galinstan, are considered as the working fluids. Notably heat transfer is enhanced with the use of structured surfaces in the selected geometry. We develop a dimensionless expression to evaluate the tradeoff between the pressure stability of a liquid-solid-gas system and hydrodynamic slip. Finally, we consider entrance effects and the temperature dependence of thermophysical properties and quantify their the effect on thermal resistance.

The third problem we consider is evaporation and condensation across menisci between ridge structures. We assume that the gaps between ridges, where the vapor phase resides, are closed systems; therefore, the net rate of heat transfer across menisci is zero. The reduction in apparent thermal slip length due to evaporation and condensation relative to the limiting case of an adiabatic meniscus is quantified. Results suggest that interfacial evaporation and condensation need be considered in the design of microchannels lined with structured surfaces for direct liquid cooling of electronics applications. A quantitative means to do so is elucidated.

The final problem we consider is the effect of meniscus curvature on thermal slip length. Perturbation theory is used to develop expressions that account for the change to temperature that occurs in the limit of small deflections to an adiabatic meniscus. Constant heat flux boundary conditions are considered at the tips of the ridges. Results show that slip length is sensitive to meniscus protrusion angle at low solid fractions. When liquid pressure is higher than that of the gas, a negative protrusion angle exists and heat transfer is enhanced. Conversely, the presence of bubble mattresses formed because the pressure in the gas is higher than that of the liquid reduces heat transfer to the liquid at low protrusion angles.

Acknowledgements

This journey of the past several years has been a fabulous experience for me. It is humbling to consider how little I could have achieved without a large group of wonderful people whom I wish to thank for their support and encouragement.

I first wish to thank my advisor, Marc Hodes, for giving me the opportunity to engage in this work and for his kind, thoughtful and skillful guidance. Marc has one of the finest engineering minds I have encountered. Whether in a formal meeting or a 5 minute hallway conversation, I learn something from every interaction with him. He has been a terrific mentor and teacher.

I thank Scott MacLachlan who has played a very active role in the last two papers. I appreciate not only his guidance in the research but also his advice on my future plans.

I would also like to thank Ryan Enright. It was a pleasure to work with him on the first two papers.

I wish to acknowledge the other members of my committee, Jeff Guasto, Vin Manno and Nikhil Nair, who could find many other important things to do with the time they have given.

I am grateful for several useful discussions with Bruce Boghosian on partial differential equations and conformal mapping.

I wish to acknowledge Durwood Marshall and Shawn Doughty of Tufts Technology Services for their assistance and access to Tufts UIT Research Computing facilities.

Funding for the research in Chapters 4 and 5 was provided in part by the NSF CBET award no. 1402783.

I want to express my appreciation to the Tufts faculty, particularly in the Mechanical Engineering department. Many of them have advised me, taught me, supervised me and provided encouragement. Since day one, I have appreciated the friendly community in this small department.

I want to acknowledge the members of the Heat Transfer Lab: Justin Griffin, Rui Zhang,

Elizabeth Brownell, Ryan Nelson, Georgios Karamanis and Dan Kane for their friendship and for helping me learn new things like Mathematica and Latex.

I would like to thank my office mates, Gabrielle String, Scott Parker, Justin Rodriguez, Xiao Xiao and Francesca Minervini, for lively discussions both technical and non-technical. Together you make a formidable group.

I want to acknowledge my friends, Marge Schmidt and Jane Guzman, who helped out with Peter's logistics at various times and Mary Glover who opened her home.

I wish to thank Susan Scott, Kathleen Liguori and Jeanne Hubbuch who have been particularly supportive these last three years.

I wish to thank Charlie Wright, Lynn Hughes, Betsy Bollier, Susan Lynch, Judy James, Bill Sawyer, Joan Gardner, Marion Hauck, Vicki Davis, Howard Webster, Kathy Weiner and Renee Toomey for our Wednesday night home group.

I am grateful for my dear friends, Clare Johns and Emily Morse, who remind me of the beauty in the world.

To my children who are a constant source of joy to me: Chris for keeping me laughing with his jokes, Marjie for her X-ray eyes and helpful comments and Peter for being flexible and understanding, and for helping me to take my PhD one tomato at a time.

Finally, I wish to thank my husband, Tom, who always has a positive outlook. He is very thoughtful about our family and is constantly supportive. He helps me keep my sense of humor, and always believes in me.

To Tom, Chris, Marjie and Peter

Yet you, Lord, are our Father.
We are the clay, you are the potter;
we are all the work of your hand.

Isaiah 64:8

TABLE OF CONTENTS

List Of Figures

Figure

List Of Tables

Table

Chapter I

Introduction

The ability to manipulate surface structure and chemistry at the micro- and nanoscale allows the designer to tailor the wetting interactions between liquids and solids in unprecedented ways [1]. Understanding the details of these interactions is of importance in the design of micro- and nanofluidic platforms for use in a variety of application areas including: biotechnology [2], thermal management of electronics [3] and energy applications [4]. Structured surfaces, e.g., superhydrophobic surfaces or superoleophobic surfaces, are a class of engineered surfaces on the micro- and nanoscale, that resist wetting and decrease hydrodynamic drag.

In the so-called Cassie-Baxter state [5], interfacial forces along triple contact lines prevent wetting of the surface, and a vapor phase[1] is trapped between the base of the surface and a liquid-vapor interface (or meniscus) as per Fig. 1.1. This introduces a composite boundary condition on the flow composed of no-slip liquid-solid and low-shear menisci [1]. Additionally, heat transfer to the liquid is affected by the details of the composite interface. It occurs primarily across the liquid-solid interface and is restricted at the meniscus due to the low conductivity of the vapor phase. When a channel scale point of view is adopted for flows over structured surfaces, the liquid is observed to slip at the composite interface and the temperature at the surface exhibits a discontinuity with that of the flow.

[1]The cavities may contain a combination of vapor and noncondensable gas depending on the application.

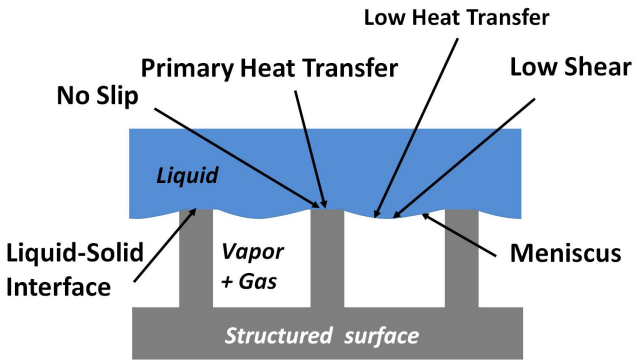

Figure 1.1: Sketch of a composite surface. Liquid is suspended on the tips of the structures and vapor fills the space below.

1.1 Slip in Rarefied Gases

In the study of transport in rarefied gases, slip expressions are used to account for the discontinuities of velocity and temperature at the surface of a tube or duct which result from interactions at the molecular level in the Knudsen layer. The Knudsen number, Kn, is used as the criterion for determining whether corrections for temperature and velocity are required. $\mathrm{Kn} = \lambda/L_c$, where λ is the molecular mean free path length and L_c is the characteristic length of the channel. Gad-el Hak provides criteria for classifying gas flows [6].[2]

The correction for velocity employs Navier's slip boundary condition [7], $u = b(\partial u/\partial n)$, where u is the streamwise velocity, n is the direction normal to the surface pointing into the flow and b is the hydrodynamic slip length. A similar relationship proposed by Poisson[3] corrects for the temperature discontinuity such that $T_\mathrm{k} - T_\mathrm{w} = g(\partial T/\partial n)$, where T_k is the fluid temperature at the surface, T_w is the surface temperature, and g is called the temperature jump distance. Maxwell [9] developed an expression for the hydrodynamic slip length based on the mean free path, thermophysical properties of the gas and a tangential momentum

[2]For $\mathrm{Kn} < 0.001$ the continuum state applies. For $0.001 < \mathrm{Kn} < 0.1$, the gas is treated as a continuum; however, slip conditions for temperature and velocity exist in the Knudsen layer adjacent to the boundary. At $\mathrm{Kn} = 0.1$, transition to free molecular flow begins and neither the Navier-Stokes-Fourier equations nor slip boundary conditions apply.

[3]According to Kennard [8].

accommodation coefficient that captures the interaction of the gas molecules with a particular surface. Similarly, Kennard [8] developed an expression for the temperature jump distance based on the same properties of the gas and a thermal accommodation coefficient, i.e., the fractional extent to which gas molecules colliding with the boundary have their mean energy adjusted as a result of the collision.

Sparrow and Lin [10] used the aforementioned slip expressions in the analysis of low density gas flows in tubes. They computed Nusselt numbers for fully developed Poiseuille flow in tubes subjected to constant heat flux and constant temperature boundary conditions. They showed that hydrodynamic slip increases the Nusselt number and thermal slip decreases it, but the net effect is always a reduction. Their results are applicable for microchannel gas flows. Jiji [11] provided several analytical solutions for both Couette and Poiseuille gas flow through various microchannel geometries with both hydrodynamic and thermal slip. In two cases, velocity and Nusselt number expressions were derived for Couette flows where viscous dissipation is considered. In the case of pressure-driven flows, the effects of increasing mean free path in the streamwise direction were considered, resulting in increasing Knudsen number, axial velocity variation and pressure gradient variation along the channel length. Colin [12] provided a comprehensive review of heat transfer in pressure-driven slip flows of gases in microchannels. He outlined various first-order and second-order forms for velocity and temperature slip expressions. He summarized work which considers viscous heating, axial conduction, viscosity and thermal conductivity which vary as a function of temperature, and thermally developing flow.

1.2 Structured Surfaces

Significantly, molecular slip in rarefied gases and *apparent* slip on structured surfaces are equivalent mathematically under many conditions. In the case of liquid flows over structured surfaces, the phenomenon of slip can be represented as a surface effect [13]. The liquid in contact with the composite surface exhibits velocity slip and temperature jump, henceforth

referred to as *apparent* slip and *apparent* thermal slip, respectively. The slip boundary conditions take the same form as those used in rarefied gases; in structured surfaces an *apparent* hydrodynamic slip length, b, and an *apparent* thermal slip length, b_t, are used.

1.2.1 Hydrodynamics

There is a significant body of theoretical and experimental work which validates Navier's [7] slip model for flow over structured surfaces. Rothstein [14] provided a review of slip on structured surfaces citing the available literature as of 2010, and some of the more relevant studies are discussed here. An idealized surface was considered by Philip [15, 16], who derived velocity profiles for eight cases with flow subject to mixed no-slip and no-shear conditions. He addressed two cases of interest: one with a periodic array of longitudinal no-shear slots and one with a periodic array of transverse no-shear slots. In the first case, he presents an expression for the amount the flow velocity increases far from the surface due to the presence of the no-shear slots. In the second, he presents a modification to the stream function that results from the presence the no-shear slots. Slip lengths can be extracted from both expressions. Building upon the work of Philip [15, 16], Lauga and Stone [17] analytically studied Poiseuille flow in a circular pipe with an idealized surface with two geometries: alternating no-slip/no-shear regions transverse to the flow, and alternating no-slip/no-shear regions parallel to the flow, i.e., ridges oriented perpendicular and parallel to the flow, respectively. They derived slip length expressions for both geometries show dependencies on surface topology and length scale.

Ou et al. [18] and Ou and Rothstein [19] were among the first to experimentally demonstrate drag reduction in the laminar flow of water over a structured surface with a pillar geometry. They visualized the meniscus and showed that meniscus deflection also affected drag reduction. Both studies showed that decreasing solid fraction and/or increasing spacing between structures resulted in drag reduction. Priezjev et al. [20] computed velocity profiles and effective slip lengths for liquid films in a plane Couette flow subject to mixed boundary

conditions where the moving surface is no slip and the stationary surface is patterned with no-slip/no-shear regions. Truesdell et al. [21] experimentally demonstrated drag reduction in a Couette flow between two surfaces, one of which was superhydrophobic with parallel ridges. They reported effective slip lengths extracted from torque data. Lee et al. [22] used a rheometer system to investigate a variety of surfaces structured with pillar and ridge patterns. They reported that gas fraction $(1 - \phi_s)$ and pitch are the key parameters influencing slip length; slip length increases exponentially with gas fraction and linearly with pitch in agreement with previous work [17].

Ybert et al. [23] provided scaling laws for effective slip length based on surface topology and reported the dependence of slip length on solid fraction showing that expressions for slip length have different dependence on solid fraction based on geometry. Using scaling and a numerical method, Ybert et al. [23] were the first to compute a slip expression for a two-dimensional array of pillars in the limit of small solid fraction.

Salamon et al. [24] numerically modeled a 3-dimensional periodically fully developed Poiseuille flow over a structured surface comprised of an array of square pillars. They showed a velocity profile with a slip length derived from numerical data in close agreement to Navier's slip model except in the immediate vicinity of the pillars. Notably, the macroscopic flow behavior is adequately characterized using an *apparent* slip model. Analytical and numerical work has addressed the validity of the shear-free boundary condition at the meniscus for pressure driven flow over parallel ridges [25] and transverse ridges [26]. The effect of curvature of the meniscus on slip length has also been studied numerically by Teo and Khoo [27] and experimentally by Steinberger et al. [28].

1.2.2 Thermal Transport over Structured Surfaces

While structured surfaces can significantly increase volumetric flow rates for a given pumping power, these surfaces can have a significant and potentially detrimental impact on convective heat transfer. When the flow near the structures is in the low Peclet number,

Pe_c,[4] limit, as is the case in the studies presented here, the local heat transfer can be considered purely diffusive. The primary heat transfer occurs across the limited area of the tips of the structures and the meniscus is considered to have low or no thermal conductivity. This diffusion-dominated heat transfer from the liquid-solid area into the flow near the composite interface represents a thermal spreading resistance. In the low Pe_c limit, the thermal slip length can be treated as a redefined conduction spreading resistance that provides a relationship between the mean temperature of the source, which is the solid-liquid interface, the mean temperature of the composite interface and mean heat flux at the composite interface as discussed by Enright et al. [29].

Such diffusive transport only occurs near the surface in a region whose depth into the flow is on the order of the characteristic length scale of the structures. The discontinuity in temperature between the mean temperature of the solid-liquid and composite interfaces may be treated analytically as a boundary condition on the macroscopic flow. This boundary condition takes the same form as Poisson's temperature jump boundary condition for rarefied gases, $T_{\mathrm{sl}} - T = -b_{\mathrm{t}}(\partial T/\partial n)$, where T_{sl} and T are the mean temperatures of the solid-liquid and composite interfaces, respectively, and b_t is the *apparent* thermal slip length based on surface geometry.

The presence of thermal slip was not considered in early studies of heat transfer across SSs. Enright et al. [30] studied the effect of hydrodynamic slip on heat transfer reporting a positive correlation. Maynes et al. [31] numerically studied a fully developed Poiseuille flow in a parallel plate channel with transverse ridges. Their simulations demonstrated a reduction in the Nusselt number, Nu, as the relative size of the meniscus is increased. They report a benefit in heat transfer with respect to pumping power for a certain Reynolds number range. Also Maynes et al. [32] modeled a thermally developing and hydrodynamically periodic fully developed flow over transverse ridges with a constant heat flux boundary condition at the

[4]The Peclet number referred to here is $\mathrm{Pe}_c = \mathrm{Re}_c\mathrm{Pr}$ where $\mathrm{Re}_c = \rho\bar{u}_c l/\mu$ is the Reynolds number at the composite interface, $\bar{u}_c$ is the mean velocity at the composite interface, l is the pitch of the structures and Pr is the Prandtl number of the liquid.

liquid-solid interface. They treated the meniscus as adiabatic and assumed a one-dimensional velocity profile to compute a two-dimensional temperature profile using Duhamel's integral. They reported Nusselt numbers and temperature profiles as a function of Peclet number and ridge/cavity geometry.

Recently, Maynes and Crockett [33] analytically modeled Poiseuille flow between parallel plates lined with ridges oriented parallel to the flow, and they present an expression for *apparent* thermal slip length as a function of Nusselt number and slip velocity in agreement with Inman [34] who derived the same expression in a rarefied gas flow. Notably, in their analysis they found a nearly one-to-one correspondence between hydrodynamic and thermal slip lengths of parallel ridges for a constant heat flux boundary condition. Enright et al. [29] analytically and numerically evaluated a fully developed Poiseuille flow over structured surfaces in a parallel plate channel. They provide expressions for thermal slip lengths for isoflux and isothermal solid-liquid interfaces and adiabatic menisci for ridge- and pillar-type structures based upon expressions for thermal spreading resistances [35]. Numerical simulations validate the use of the thermal spreading resistance based slip lengths when the length scale of the structures is much smaller than the channel height. They derive a relationship between thermal and hydrodynamic slip lengths for parallel ridges, transverse ridges and pillars where $b_t/b \approx 1.0, 2.0$ and 1.5, respectively, for a constant temperature boundary condition. Notably, they derive Poiseuille, Po,[5]and Nusselt number expressions for a pressure-driven flow in the presence of hydrodynamic and thermal slip with arbitrary asymmetric constant heat flux boundary conditions.

Ng and Wang [36] semi-analytically computed thermal slip lengths for isothermal, ridge-type structures as a function of vapor-phase to liquid-phase thermal conductivity and cavity depth when isothermal surfaces bounded the vapor phase. When the cavity depth is shallow compared to structure spacing, conduction through the vapor phase can reduce the thermal slip length relative to the case of an adiabatic meniscus. For cavity depths on the order of

[5] $\mathrm{Po} = f\mathrm{Re}_{D_h}$

the spacing of the structures and larger, conduction through the gas has negligible impact on slip length. Ng and Wang [36] also semi-analytically computed slip lengths for an isothermal surface with adiabatic circular or square holes.

1.3 Secondary Effects at the Meniscus

In order to simplify modeling, secondary effects at the meniscus are often considered negligible. However, in the presence of heat transfer, phase change at the interface and meniscus curvature will alter thermal slip lengths.

1.3.1 Phase Change

A common assumption that is made regarding the meniscus is that it is adiabatic. However, e.g., in the case of water, evaporation and condensation will produce heat and mass transfer across the meniscus. Carey [37] and Schrage [38] provide expressions for mass, momentum and energy transport across an interface which separates a liquid and its vapor; these will be discussed in Chapter 4. Evaporation and condensation of droplets on superhydrophobic surfaces have been studied [39–41], but the effect of evaporation and condensation on *apparent* slip has not been addressed.

1.3.2 Meniscus Curvature

A number of studies have shown that the shape of the meniscus and the degree of protrusion significantly affect drag. Ybert et al. [23] derived expressions for secondary effects such as a finite shear force at the meniscus and pressure-induced curvature of the meniscus. They assumed a meniscus with a positive protrusion angle, i.e., positive pressure in the gas. In the limit of large solid fraction, the correction to slip length is negatively proportional to the cavity fraction and the height of the meniscus. In the limit of small solid fraction, the correction to slip length varies inversely with curvature such that for high curvature the slip length is negatively impacted. They note for small pressure differences or low curvatures,

slip lengths are less sensitive to curvature effects. Bocquet and Barrat [42] discuss the analogy between thermal slip and hydrodynamic slip. We note that these scaling laws are also applicable to thermal slip in the presence of curvature.

Sbragaglia and Prosperetti [43] used perturbation theory to study the effect of small deflections in the meniscus as a function of shear free fraction. They identify two significant effects that result. The first is the effect on the change in the cross-sectional area of the flow due to the deformation at the meniscus, and the second is the change in the velocity field. They provide hydrodynamic slip length expressions for parallel ridges for a pressure driven flow with a finite channel height and for shear flow with an infinite channel height. They use a small parameter ε in their expressions but they do not account for the fact the ε changes with shear-free fraction.

Steinberger et al. [28] studied menisci formed on a surface composed of a square lattice of cylindrical holes. They used a dynamic surface force apparatus to measure viscous damping forces which they correlated to slip lengths. They experimentally studied two cases, liquid in the Cassie and Wenzel states. When the liquid was in the Cassie state, gas bubbles were trapped in the holes with menisci protruding upward in the shape of spherical caps. In the Wenzel state, the surface and cavities were fully wetted. They found a lower effective slip length in the presence of microbubbles than in the wetted state. Notably, roughness caused by the presence of these bubbles increased friction at the surface. They also performed numerical simulations of a Couette flow over menisci with the same geometry at various contact angles. They found that the shape and protrusion angle of the meniscus significantly affected slip length. For negative protrusion angles slip length increased with protrusion angle. The maximum value of slip length was reached at angle of zero. For positive protrusion angles, slip length was degraded as protrusion angle increased and became negative above a critical value.

Hyvaluoma and Harting [44] used a mesoscopic lattice Boltzmann simulation to study Couette flow over structured surfaces with attached gas bubbles. They accounted for de-

formation of the bubbles due to viscous forces. They found slip length had a shear rate dependence. Increasing the shear rate decreased the height of the bubbles therefore reducing the roughness caused by the bubbles. They report slip length as a function of protrusion angle of the bubbles and found the same qualitative relationship between protrusion angle and slip length in agreement with Steinberger et al. [28].

Two analytical studies have addressed the effect of meniscus curvature in the limit of low shear-free fraction. Crowdy [45] used a series of conformal maps to model a meniscus between parallel ridges. He derived an expression for slip length as a function of solid fraction and protrusion angle which is applicable for a periodic distribution of ridges in the limit of large solid fractions. Davis and Lauga [46] used a two-dimensional model of shear flow past an array of bubbles trapped between transverse ridges and provide an expression to calculate the critical protrusion angle. Their results also show the asymmetry between the effects of negative and positive protrusion angles.

Teo and Khoo performed numerical studies of the effect of meniscus curvature on drag for menisci formed between parallel ridges for both Poiseuille and Couette flows [27] and in Poiseuille flow between transverse ridges [47]. For transverse ridges, they report a critical protrusion angle $\theta_c \approx 62 - 65^\circ$ at which the slip length becomes zero that is independent of shear-free fraction, geometry and flow type but which decreases as channel height is reduced for a given shear-free fraction. Above θ_c, friction was enhanced. For parallel ridges, slip length displayed asymmetry with respect to positive and negative protrusion angles; however, there was no critical angle at which drag reduction became zero. Instead the slip length exhibited a monotonic increase with protrusion angle even for large angle values up to 90°. They also found that the ratio of parallel ridge slip length to transverse ridge slip length did not remain constant as protrusion angle was varied. Notably, their results showed a more positive benefit in drag reduction for menisci between parallel ridges than for transverse ridges holding shear-free fraction, protrusion angle and normalized rib spacing constant. Teo and Khoo [47] correlated their results with those of Davis and Lauga [46],

Crowdy [45] and Ng and Wang [48] showing good agreement between the numerical results and the analytical models.

1.4 Liquid Cooling of Electronics

Structured surfaces are being considered for a a variety of applications. We focus here on internal flows across these surfaces where they would line the walls of a microgap or minichannel embedded in an electronic device. As power density and heat load requirements for electronic devices continue to rise, the need for effective cooling alternatives increases. Single-phase direct liquid cooling of electronics in a microchannel configuration was first investigated by Tuckerman and Pease [49] in 1981. Numerous studies have followed, e.g., [50–53].

In mini- and micro- channels friction forces play a more significant deterrent to liquid flow due to the higher ratio of surface area to cross-sectional area. The addition of structured surfaces has the potential to compensate for the added friction by reducing drag. However, heat transfer will also be impacted and as we show in the following chapters, the type of impact and magnitude will be determined by a variety of factors e.g., wetting interactions of the liquid-gas-solid system, the geometry of the channel, the thermophysical properties of the working fluid, boundary conditions on the flow as well effects at the interface such as meniscus curvature and phase change.

1.5 Organization of Thesis

This dissertation contains six chapters, including four journal papers, and addresses heat transfer on two scales. Chapters 2 and 3 address heat transfer to Couette and Poiseuille flows, respectively, on the scale of a microchannel where structured surfaces are assumed on the channel walls. Chapters 4 and 5 address heat transfer near the structures on a scale on the order of the pitch of the structures. They address topics which have heretofore been

considered negligible: evaporation and condensation across the meniscus and curvature of the meniscus. Chapter 6 summarizes results and conclusions.

Chapter II

Nusselt Numbers for Thermally Developing Couette Flow with Hydrodynamic and Thermal Slip[1]

Abstract

The effects of hydrodynamic and thermal slip on heat transfer in a thermally developing, steady, laminar Couette flow are investigated. Fluid temperature at the inlet to a parallel plate channel is prescribed, as are various combinations of isothermal and adiabatic boundary conditions along its surfaces. Analytical expressions incorporating arbitrary slip are developed for temperature profiles, and developing and fully developed Nusselt numbers. The results are relevant to liquid and gas flows in the presence of apparent and molecular slip, respectively.

2.1 Introduction

Developing temperature profiles for Couette flow were first computed in 1951 by Vogelpohl [54], who calculated those generated by viscous dissipation in flow between two insulated parallel plates. Several studies on plane Couette flow and Poiseuille-Couette flow followed and provided Nusselt numbers for various thermal boundary conditions [55–58].

[1]This work has appeared in "Nusselt Numbers for Thermally Developing Couette Flow With Hydrodynamic and Thermal Slip," L. Steigerwalt Lam, C. Melnick, M. Hodes, G. Ziskind, and R. Enright, *Journal Heat Transfer* **136(5), 2014.**

Insight into the entrance behavior was limited by the number of eigenvalues computed. Šesták and Rieger [59] developed temperature profiles and Nusselt number expressions with a sufficient number of eigenvalues to capture entrance behavior for the four sets of thermal boundary conditions considered here in the presence of slip. Couette flow has also been studied in rarefied gas flow by, e.g., [60–64], but to the authors' knowledge, Nusselt numbers which account for arbitrary slip at the boundaries in a Couette flow do not exist in the literature.

In the context of apparent slip flows, where slip can be tailored independently on the respective boundaries, several combinations of boundary conditions are possible that are not typically considered in the study of molecular slip. These effects on convective heat transfer have not been considered and this point motivates this chapter.

In section 2, we present the governing equations for an structured surface-enhanced steady laminar plane Couette flow that is thermally developing [56, 59]. In section 3, a general infinite series solution is developed that accounts for hydrodynamic and thermal slip. Analytical expressions in terms of Airy functions for the temperature field, bulk temperature and Nusselt numbers are derived for four sets of thermal boundary conditions. Each case is analyzed with four representative sets of hydrodynamic and thermal slip lengths. In section 4, temperature profiles and Nusselt number plots are presented. Finally, the impact of hydrodynamic and thermal slip on thermally developing transport in a Couette flow is discussed. The main contribution of this work is to provide Nusselt number expressions for a Couette flow which account for arbitrary hydrodynamic and thermal slip.

2.2 Problem Formulation

2.2.1 Hydrodynamics

The relevant form of the x-momentum equation for hydrodynamically fully developed Couette flow is

$$\frac{d^2u}{dy^2} = 0, \tag{2.1}$$

where u is the streamwise velocity, and y is the spanwise coordinate originating at the stationary surface. In the presence of hydrodynamic slip, both the stationary and the moving surfaces are taken to be composite interfaces comprised of liquid-solid and liquid-vapor regions, and the respective boundary conditions are

$$u = b_s \left.\frac{du}{dy}\right|_{y=0} \tag{2.2}$$

$$u = U_o - b_m \left.\frac{du}{dy}\right|_{y=H}, \tag{2.3}$$

where H is the distance between surfaces, b_s and b_m are the hydrodynamic slip lengths at the stationary and moving surfaces, respectively, and U_o is the velocity of the liquid-solid interface at the moving surface. The liquid-vapor interface is assumed to be flat and shear free.

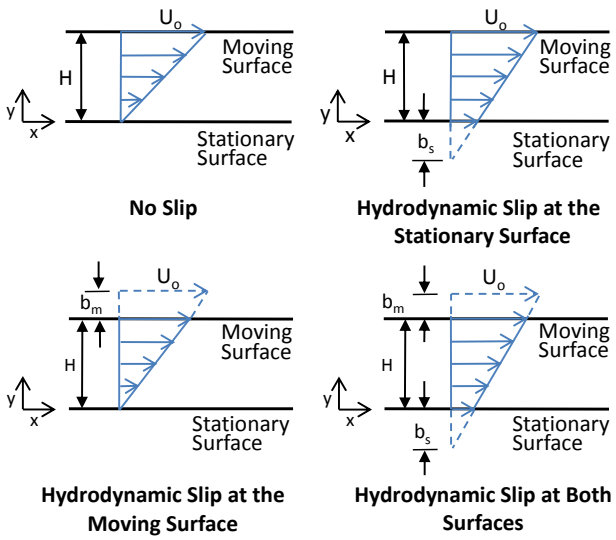

Figure 2.1: Representative fluid velocity profiles for a Couette flow with 4 possible combinations of hydrodynamic slip.

The streamwise velocity profile is

$$u = \frac{U_o}{H + b_s + b_m}(y + b_s), \tag{2.4}$$

and the mean velocity is

$$u_m = \frac{U_o}{H + b_s + b_m}\left(\frac{H}{2} + b_s\right). \tag{2.5}$$

Figure 2.1 shows the velocity profiles associated with the four possible combinations of zero and finite slip at each surface.

2.2.2 Heat Transfer

The thermal energy equation in the absence of viscous dissipation and axial conduction in the case of the thermally developing flow considered here is

$$u\frac{\partial T}{\partial x} = \alpha\frac{\partial^2 T}{\partial y^2}, \tag{2.6}$$

where α is the thermal diffusivity, T is the liquid temperature and x is the streamwise coordinate originating at the channel entrance, where uniform inlet temperature, T_{in}, is assumed.

Thermophysical properties are considered constant. The possibility of Marangoni stresses and thermal creep caused by the temperature field at the wall are neglected, as are potential evaporation and condensation effects along the liquid-vapor interface. We consider the four combinations of thermal boundary conditions at the stationary and moving surfaces studied by Šesták and Rieger [59] and depicted in Fig. 2.2 in the absence of slip. This provides a baseline for validating our analytical solutions.

In Case A, the temperatures of the liquid-solid interfaces on both surfaces are maintained at equal and constant temperature, T_p. Case B is the same as Case A with the exception that the temperature of the liquid-solid interface on the moving surface is maintained at the inlet temperature, T_{in}. For Case C, the liquid-solid interface on the stationary surface is maintained at T_{p}, and the moving surface is adiabatic. Finally, for Case D, the liquid-solid interface on the moving surface is maintained at T_p, and the stationary surface is adiabatic.

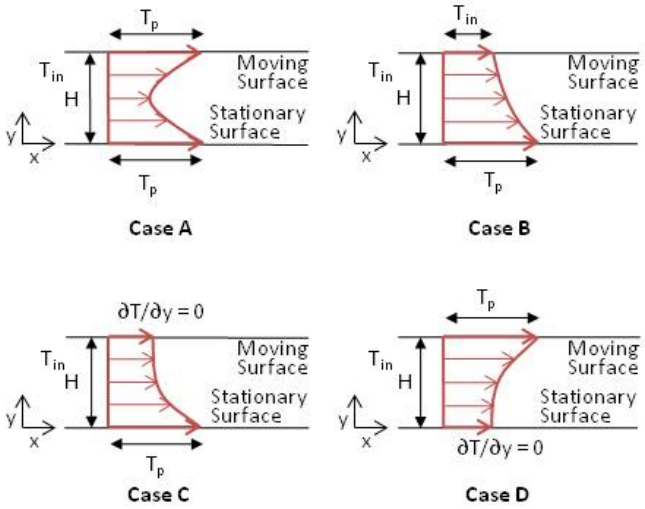

Figure 2.2: Sketch of temperature profiles for four thermal boundary conditions for Cases A - D in the absence of slip.

Schematic temperature profiles in the presence of thermal slip are shown in Fig. 2.3 for each case. When thermal slip is present, it is manifested as a temperature discontinuity between the temperature of the liquid-solid interface and that of the liquid evaluated at the composite interface. The thermal boundary conditions which account for thermal slip are

$$T_{\mathrm{s}} - T = -b_{\mathrm{t,s}} \left. \frac{\partial T}{\partial y} \right|_{y=0} \quad \text{for } x > 0 \tag{2.7}$$

$$T_{\mathrm{m}} - T = b_{\mathrm{t,m}} \left. \frac{\partial T}{\partial y} \right|_{y=H} \quad \text{for } x > 0, \tag{2.8}$$

where T_s and T_m are the temperatures of the liquid-solid interfaces at each surface, and, when evaluated at the surface, the liquid temperature, T, equals the area-averaged temperature of the composite interface. $b_{\mathrm{t,s}}$ and $b_{\mathrm{t,m}}$ are the thermal slip lengths at the stationary and moving surfaces, respectively.

Temperature profiles for each thermal case are evaluated with four combinations of slip conditions which are itemized in sub-cases. Sub-case 1 is the no slip case where the surface may be assumed to be a uniform liquid-solid interface across the entire boundary. Sub-case 2 has slip present at the stationary surface and zero slip at the moving surface. Sub-case 3 has slip present at the moving surface and zero slip at the stationary surface. Finally, in

sub-case 4, slip is present at both surfaces.

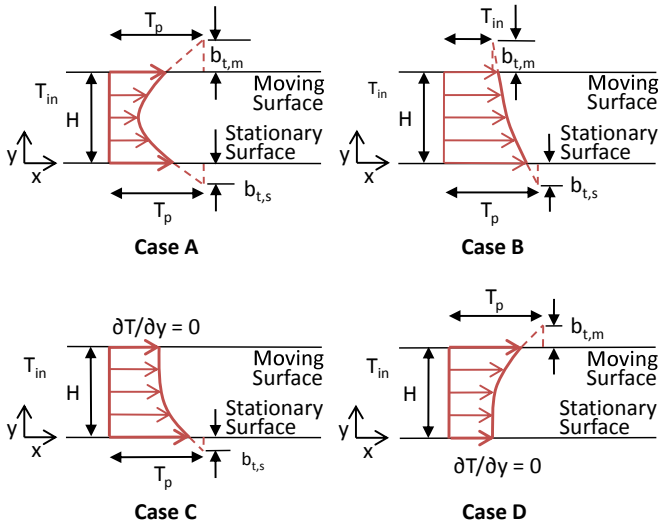

Figure 2.3: Sketch of temperature profiles for four thermal boundary conditions for Cases A - D in the presence of slip.

We have chosen to model the particular case where the thermal slip length and hydrodynamic slip length are equal, $b = b_t$, corresponding to flow over parallel ridges subject to a constant temperature boundary condition. Velocity slip and temperature jump are present concurrently; near the surface both hydrodynamic and thermal behavior are strictly diffusive with the same effective boundary condition in this case. The choice of slip length is arbitrary; however, a hydrodynamic slip length on the order of the height of the channel is requisite to influence the flow. The magnitude of the dimensionless slip length is set to half the channel dimension, $b^* = H/2$. This value is in the range which is commonly used in analytical and numerical studies [13, 65]

2.3 Analytical Solution

2.3.1 Non-dimensionalization

The preceding equations are rendered dimensionless by

$$x^* = \frac{2x/H}{Re_{D_h} Pr} \tag{2.9}$$

$$y^* = y/H \tag{2.10}$$

$$T^* = \frac{T_\mathrm{p} - T}{T_\mathrm{p} - T_\mathrm{in}} \tag{2.11}$$

$$u^* = u/U_o \tag{2.12}$$

$$u_m^* = u_m/U_o \tag{2.13}$$

$$b_s^* = b_s/H \tag{2.14}$$

$$b_m^* = b_m/H \tag{2.15}$$

$$b_{\mathrm{t},s}^* = b_{\mathrm{t},s}/H \tag{2.16}$$

$$b_{\mathrm{t},m}^* = b_{\mathrm{t},m}/H \tag{2.17}$$

$$H^* = H/(H + b_s + b_m), \tag{2.18}$$

where $\mathrm{Re}_{D_h} = 2Hu_m/\nu$.[2] The dimensionless streamwise velocity profile and the dimensionless mean velocity become

$$u^* = \frac{y^* + b_s^*}{1 + b_s^* + b_m^*} \tag{2.19}$$

$$u_m^* = \frac{1/2 + b_s^*}{1 + b_s^* + b_m^*}. \tag{2.20}$$

[2]We use u_m rather than U_o in the Reynolds number. This has the effect of normalizing the mass flow rate for various hydrodynamic slip boundary conditions and allows one to compare temperature profiles at a given dimensionless channel length to determine the relative amount of thermal energy absorbed by the fluid for different boundary conditions.

The dimensionless thermal energy equation is

$$\frac{\partial^2 T^*}{\partial y^{*2}} = \frac{2(y^* + b_s^*)}{1 + 2b_s^*} \frac{\partial T^*}{\partial x^*}. \tag{2.21}$$

Table 2.1 provides the dimensionless thermal boundary conditions for the four thermal cases considered.

2.3.2 General Solution

The dimensionless thermal energy equation is solved for the dimensionless temperature field by using the method of separation of variables. Assuming a solution of the form $T^*(x^*, y^*) = X(x^*)Y(y^*)$ and a separation constant of -λ^2, it becomes

$$\frac{dX}{dx^*} + \lambda^2 X = 0 \tag{2.22}$$

$$\frac{d^2 Y}{dy^{*2}} + \frac{2(y^* + b_s^*)}{1 + 2b_s^*} \lambda^2 Y = 0. \tag{2.23}$$

Treating the cases of $\lambda = 0$ and $\lambda \neq 0$ separately, the solution to Eq. (2.22) is

$$X(x^*) = \begin{cases} A, & \lambda = 0 \\ Be^{-\lambda^2 x^*}, & \lambda \neq 0. \end{cases} \tag{2.24}$$

For $\lambda = 0$, the solution to Eq. (2.23) is $Y(y^*) = C + Dy^*$. By defining $z(y^*) = -2^{1/3}\lambda^{2/3}(y^* + b_s^*)/(1 + 2b_s^*)^{1/3}$, Eq. (2.23) is transformed into the Airy equation,

$$\frac{d^2 Y}{dz^2} - z(y^*)Y = 0 \tag{2.25}$$

and the solution becomes:

$$Y(y^*) = \begin{cases} C + Dy^*, & \lambda = 0 \\ EAi[z(y^*)] + FBi[z(y^*)], & \lambda \neq 0. \end{cases} \tag{2.26}$$

Inlet Condition	Thermal Boundary Conditions		Thermal Slip Values		Case
	Stationary Surface	Moving Surface	Stationary Surface	Moving Surface	
$T^*_{x^*=0} = 1$	$T^*_{y^*=0} = b^*_{\mathrm{t},s} \left.\frac{\partial T^*}{\partial y^*}\right\|_{y^*=0}$	$T^*_{y^*=1} = -b^*_{\mathrm{t},m} \left.\frac{\partial T^*}{\partial y^*}\right\|_{y^*=1}$	$b^*_{t,s} = 0$	$b^*_{t,m} = 0$	A.1
			$b^*_{t,s} > 0$	$b^*_{t,m} = 0$	A.2
			$b^*_{t,s} = 0$	$b^*_{t,m} > 0$	A.3
			$b^*_{t,s} > 0$	$b^*_{t,m} > 0$	A.4
	$T^*_{y^*=0} = b^*_{\mathrm{t},s} \left.\frac{\partial T^*}{\partial y^*}\right\|_{y^*=0}$	$T^*_{y^*=1} - 1 = -b^*_{\mathrm{t},m} \left.\frac{\partial T^*}{\partial y^*}\right\|_{y^*=1}$	$b^*_{t,s} = 0$	$b^*_{t,m} = 0$	B.1
			$b^*_{t,s} > 0$	$b^*_{t,m} = 0$	B.2
			$b^*_{t,s} = 0$	$b^*_{t,m} > 0$	B.3
			$b^*_{t,s} > 0$	$b^*_{t,m} > 0$	B.4
	$T^*_{y^*=0} = b^*_{\mathrm{t},s} \left.\frac{\partial T^*}{\partial y^*}\right\|_{y^*=0}$	$\left.\frac{\partial T^*}{\partial y^*}\right\|_{y^*=1} = 0$	$b^*_{t,s} = 0$	$b^*_{t,m} \geq 0$	C.1
			$b^*_{t,s} > 0$	$b^*_{t,m} \geq 0$	C.2
	$\left.\frac{\partial T^*}{\partial y^*}\right\|_{y^*=0} = 0$	$T^*_{y^*=1} = -b^*_{\mathrm{t},m} \left.\frac{\partial T^*}{\partial y^*}\right\|_{y^*=1}$	$b^*_{t,s} \geq 0$	$b^*_{t,m} = 0$	D.1, D.2
			$b^*_{t,s} \geq 0$	$b^*_{t,m} > 0$	D.3, D.4

Table 2.1: Dimensionless Thermal Boundary and Slip Conditions by Case.

where Ai and Bi are Airy functions of the first and second kind, respectively.

Defining $G = AC$, $I = AD$, $J_n = BC$, $K_n = F/E$, and

$$z_n(y^*) = -2^{1/3}\lambda_n^{2/3}(y^* + b_s^*)/(1 + 2b_s^*)^{1/3} \tag{2.27}$$

where λ_n are an infinite number of eigenvalues found from the eigencondition given for each case. The dimensionless temperature solution is of the form

$$T^* = G + Iy^* + \sum_{n=1}^{\infty} J_n e^{-\lambda_n^2 x^*} \big\{ Ai[z_n(y^*)] + K_n Bi[z_n(y^*)] \big\}. \tag{2.28}$$

By applying specific boundary conditions and choosing hydrodynamic and thermal slip lengths, a temperature solution follows.

Bulk temperature, T_b, equals $\int_0^H uTdy / \int_0^H udy$. In dimensionless form it becomes

$$T_{\mathrm{b}}^* = \frac{2}{2b_s^* + 1} \int_0^1 (y^* + b_s^*) T^* dy^*, \tag{2.29}$$

and it may be found by integrating Eq. (2.28) term by term. A surface energy balance at each composite interface yields the succeeding equations [66]

$$h_{\mathrm{s}}(T_s - T_b) = -k \frac{\partial T}{\partial y}\Big|_{y=0}, \tag{2.30}$$

$$h_{\mathrm{m}}(T_m - T_b) = k \frac{\partial T}{\partial y}\Big|_{y=H}, \tag{2.31}$$

where h_{s} and h_{m} are the local heat transfer coefficients at the stationary and moving surfaces, respectively, and k is the fluid thermal conductivity. Substituting dimensionless variables and rearranging, the local Nusselt numbers, $\mathrm{Nu} = hH/k$, at the stationary and moving

surfaces become, respectively,

$$\mathrm{Nu_s} = \frac{\left(\partial T^* / \partial y^*\right)_{y^*=0}}{T_\mathrm{b}^* - T_s^*}, \tag{2.32}$$

$$\mathrm{Nu_m} = -\frac{\left(\partial T^* / \partial y^*\right)_{y^*=1}}{T_\mathrm{b}^* - T_m^*}. \tag{2.33}$$

The total Nusselt number is defined as

$$\mathrm{Nu}_T = \mathrm{Nu_s} + \mathrm{Nu_m}, \tag{2.34}$$

for Case A only. Nusselt numbers are unique for each case and must be determined based on the choice of thermal boundary conditions, hydrodynamic and thermal slip lengths.

2.3.3 Case A

Substituting Eq. (2.28) into the boundary condition at the stationary surface yields

$$G = b_{t,s}^* I \tag{2.35}$$

and

$$K_n = -\frac{Ai[z_n(0)] - b_{t,s}^* z_n'(y^*) Ai'[z_n(0)]}{Bi[z_n(0)] - b_{t,s}^* z_n'(y^*) Bi'[z_n(0)]}. \tag{2.36}$$

Substituting Eq. (2.28) into the boundary condition at the moving surface yields $G = I = 0$ and the eigencondition for Case A,

$$\begin{aligned} &Ai\left[z_n(1)\right] + K_n Bi\left[z_n(1)\right] \\ &+ b_{t,m}^* z_n'(y^*) \left\{Ai'\left[z_n(1)\right] + K_n Bi'\left[z_n(1)\right]\right\} = 0. \end{aligned} \tag{2.37}$$

Each eigenvalue must have one corresponding linearly independent eigenfunction. For an arbitrary set of hydrodynamic and thermal slip lengths, the left-hand side of Eq. (2.37)

is an even function of λ_n. Thus, negative eigenvalues produce a set of linearly dependent eigenfunctions and are discarded.

Applying the boundary condition at the channel entrance, Eq. (2.28) becomes

$$\sum_{n=1}^{\infty} J_n \left\{ Ai[z_n(y^*)] + K_n Bi[z_n(y^*)] \right\} = 1. \tag{2.38}$$

Equation (2.23) and the boundary conditions in the y^* direction constitute the Sturm-Liouville system [67]. The property of orthogonality is used to find J_n. Both sides of Eq. (2.38) are multiplied by the m^{th} eigenfunction and the weighting factor, $2(y^* + b_s^*)/(1 + 2b_s^*)$ from Eq. (2.23), and integrated across the domain with respect to y^*. Since the m^{th} and n^{th} terms are orthogonal with respect to the weighting function, all terms in the summation integrate to zero except when $m = n$, and J_n becomes

$$\begin{aligned} J_n = & \int_0^1 \Big\{ Ai[z_n(y^*)] + K_n Bi[z_n(y^*)] \Big\} \\ & (y^* + b_s^*) dy^* \Big/ \int_0^1 \Big\{ Ai[z_n(y^*)] + \\ & K_n Bi[z_n(y^*)] \Big\}^2 (y^* + b_s^*) dy^*. \end{aligned} \tag{2.39}$$

The symbolic form of J_n is rather cumbersome; therefore, it is not shown. Equation (2.39) is evaluated in Mathematica 8.0.1.0 which produces values for J_n corresponding to each eigenvalue. The dimensionless temperature for Case A is

$$T^* = \sum_{n=1}^{\infty} J_n e^{-\lambda_n^2 x^*} \left\{ Ai\left[z_n(y^*)\right] + K_n Bi\left[z_n(y^*)\right] \right\}. \tag{2.40}$$

The corresponding dimensionless bulk temperature is

$$\begin{aligned} T_b^* = & \frac{2^{1/3}}{(1 + 2b_s^*)^{1/3}} \sum_{n=1}^{\infty} J_n \lambda_n^{-4/3} e^{-\lambda_n^2 x^*} \Big\{ Ai'\left[z_n(1)\right] - \\ & Ai'\left[z_n(0)\right] + K_n \left(Bi'\left[z_n(1)\right] - Bi'\left[z_n(0)\right] \right) \Big\}. \end{aligned} \tag{2.41}$$

The local Nusselt number at the stationary surface becomes

$$\mathrm{Nu}_s = \frac{-\sum_{n=1}^{\infty} L_n e^{-\lambda_n^2 x^*}}{\sum_{n=1}^{\infty} M_n e^{-\lambda_n^2 x^*}}, \tag{2.42}$$

where

$$L_n = J_n {\lambda_n}^{2/3} \left\{ Ai' \left[z_n(0) \right] + K_n Bi' \left[z_n(0) \right] \right\} \tag{2.43}$$

$$\begin{aligned} M_n = J_n \lambda_n^{-4/3} \Big\{ & Ai' \left[z_n(1) \right] - Ai' \left[z_n(0) \right] \\ & + K_n \left(Bi' \left[z_n(1) \right] - Bi' \left[z_n(0) \right] \right) \Big\}. \end{aligned} \tag{2.44}$$

The local Nusselt number at the moving surface becomes

$$\mathrm{Nu}_m = \frac{\sum_{n=1}^{\infty} N_n e^{-\lambda_n^2 x^*}}{\sum_{n=1}^{\infty} M_n e^{-\lambda_n^2 x^*}}, \tag{2.45}$$

where

$$N_n = J_n {\lambda_n}^{2/3} Ai' \left[z_n(1) \right] + K_n Bi' \left[z_n(1) \right]. \tag{2.46}$$

The fully developed values of Nusselt numbers are equal to the ratio of the leading coefficients of the numerator and denominator and can be computed for selected slip lengths with one eigenvalue.

2.3.4 Case B

Case B is the same as Case A, except the moving surface is maintained at the inlet temperature, T_{in}, rather than T_p. This results in a non-homogeneous boundary condition at the moving surface which is accommodated by the use of the terms associated with $\lambda = 0$.

Applying the boundary conditions in the y^* direction, the dimensionless temperature profile for Case B becomes

$$T^* = \frac{b^*_{\mathrm{t,s}} + y^*}{1 + b^*_{\mathrm{t,s}} + b^*_{\mathrm{t,m}}} + \sum_{n=1}^{\infty} J_n e^{-\lambda_n^2 x^*} \{Ai\left[z_n(y^*)\right] + K_n Bi\left[z_n(y^*)\right]\}, \tag{2.47}$$

where K_n and the eigencondition are the same as for Case A. The Sturm-Liouville system requirement that the boundary conditions be homogeneous is satisfied by the second term in Eq. (2.47) [68]. The orthogonality relation corresponding to the Sturm-Liouville system is used to find J_n,

$$J_n = \int_0^1 \left(\frac{1 + b^*_{t,m} - y^*}{1 + b^*_{\mathrm{t,s}} + b^*_{\mathrm{t,m}}}\right) \Big\{Ai\left[z_n(y^*)\right] + K_n Bi\left[z_n(y^*)\right]\Big\}(y^* + b^*_s)dy^* \Big/ \int_0^1 \Big\{Ai\left[z_n(y^*)\right] + K_n Bi\left[z_n(y^*)\right]\Big\}^2 (y^* + b^*_s)dy^*. \tag{2.48}$$

The dimensionless bulk temperature is

$$T^*_b = \frac{2 + 3b^*_s + 3b^*_{t,s} + 6b^*_s b^*_{t,s}}{3(1 + 2b^*_s)(1 + b^*_{t,s} + b^*_{t,m})} + \frac{2^{1/3}}{(1 + 2b^*_s)^{1/3}} \sum_{n=1}^{\infty} J_n \lambda_n^{-4/3} e^{-\lambda_n^2 x^*} \Big\{Ai'\left[z_n(1)\right] - Ai'\left[z_n(0)\right] + K_n\left(Bi'\left[z_n(1)\right] - Bi'\left[z_n(0)\right]\right)\Big\}. \tag{2.49}$$

The local Nusselt number at the stationary surface becomes

$$\mathrm{Nu}_s = \frac{\dfrac{1}{1 + b^*_{t,s} + b^*_{t,m}} - \displaystyle\sum_{n=1}^{\infty} O_n e^{-\lambda_n^2 x^*}}{\dfrac{2 + 3b^*_s + 3b^*_{t,s} + 6b^*_s b^*_{t,s}}{3(1 + 2b^*_s)(1 + b^*_{t,s} + b^*_{t,m})} + \displaystyle\sum_{n=1}^{\infty} P_n e^{-\lambda_n^2 x^*}}, \tag{2.50}$$

where

$$O_n = -J_n z_n'(y^*)\left\{Ai'\left[z_n(0)\right] + K_n Bi'\left[z_n(0)\right]\right\} \tag{2.51}$$

$$P_n = J_n \frac{2^{1/3}\lambda_n^{-4/3}}{(1+2b_s^*)^{1/3}}\Big\{Ai'\left[z_n(1)\right] - Ai'\left[z_n(0)\right] + K_n\Big(Bi'\left[z_n(1)\right] - Bi'\left[z_n(0)\right]\Big)\Big\}. \tag{2.52}$$

The local Nusselt number at the moving surface becomes

$$\mathrm{Nu}_m = \frac{\dfrac{1}{1+b_{t,s}^*+b_{t,m}^*} - \displaystyle\sum_{n=1}^{\infty} Q_n e^{-\lambda_n^2 x^*}}{\dfrac{1+3b_s^*+3b_{t,m}^*+6b_s^* b_{t,m}^*}{3(1+2b_s^*)(1+b_{t,s}^*+b_{t,m}^*)} - \displaystyle\sum_{n=1}^{\infty} P_n e^{-\lambda_n^2 x^*}}, \tag{2.53}$$

where

$$Q_n = -J_n z_n'(y^*)\left\{Ai'\left[z_n(1)\right] + K_n Bi'\left[z_n(1)\right]\right\}. \tag{2.54}$$

2.3.5 Case C

In Case C, the stationary surface is maintained at T_p, and the moving surface is adiabatic. The eigencondition for Case C is

$$Ai'\left[z_n(1)\right] + K_n Bi'\left[z_n(1)\right] = 0. \tag{2.55}$$

Expressions for the dimensionless temperature and associated constants, Eqs. 2.36, 2.39 and 2.40 are the same as those of Case A. The Nusselt number at the moving surface is 0, and the Nusselt number at the stationary surface is found with Eq. (2.42). Eigenvalues are found based on selected slip lengths which result in distinct solutions for Eqs. 2.36, 2.39, 2.40 and 2.42.

2.3.6 Case D

In Case D, the stationary surface is adiabatic, and the moving surface is maintained at T_p. Application of the boundary condition on the stationary surface yields $I = 0$ and

$$K_n = -\frac{Ai'[z_n(0)]}{Bi'[z_n(0)]}. \tag{2.56}$$

Application of the boundary condition at the moving surface yields $G = 0$, and Eq. (2.37) does not change. Substituting Eq. (2.56) into Eq. (2.37) yields the eigencondition for Case D,

$$\begin{aligned} &Ai\left[z_n(1)\right] + K_n Bi\left[z_n(1)\right] \\ &+ b^*_{t,m} z'_n(y^*)\left\{Ai'\left[z_n(1)\right] + K_n Bi'\left[z_n(1)\right]\right\} = 0. \end{aligned} \tag{2.57}$$

The dimensionless temperature expression, J_n, and Nusselt number expressions are the same as for Case A. There is no heat transfer at the stationary surface; the Nusselt number at the moving surface is found from Eq. (2.45). Eigenvalues are found based on selected slip lengths which result in distinct solutions for Eqs. 2.36, 2.39, 2.40, and 2.45.

2.4 Results and Discussion

Representative results are presented in the form of a tabulation of fully developed Nusselt numbers, plots of dimensionless temperature versus dimensionless channel height at a fixed dimensionless channel length, and plots of Nusselt numbers versus dimensionless channel length. In cases where dimensionless hydrodynamic and thermal slip lengths are finite, they are set equal to 0.5.

2.4.1 Model Validation

We note that our results for Cases A.1, B.1, C.1 and D.1, where slip is not present, are in full agreement with those of Šesták and Rieger [59].[3,4] Figure 2.4 shows individual and total Nusselt numbers plotted versus the dimensionless channel length for Case A.1. The Nusselt number is highest at the entrance and, in most cases, decreases monotonically to a horizontal asymptote. However, the Nu_s curve behaves non-monotonically in the region of $x^* = 0.03$. This is documented in the literature [59].

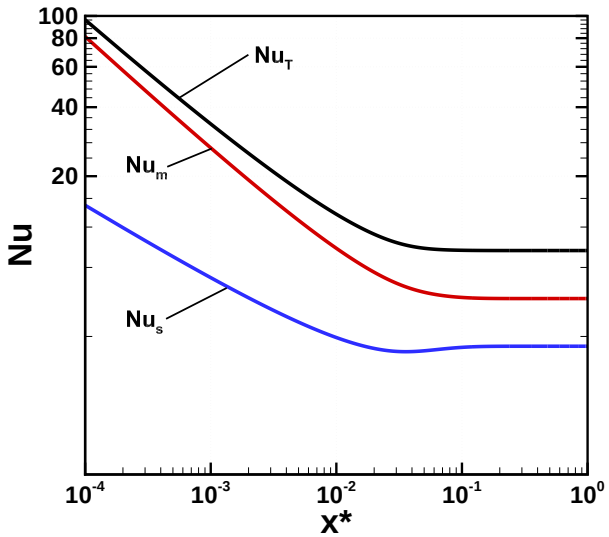

Figure 2.4: Nusselt number versus dimensionless channel length, x^*, for Case A.1, symmetric constant temperature boundary conditions with no slip.

While the fully developed Nusselt number can be calculated with only one eigenvalue, additional terms are needed to compute entrance behavior. Moreover, as x^* approaches very small values, more terms are required to achieve convergence. At $x^* = 0.0001$ the value of the seventy-first term is 0.02% of the value of Nu_T with seventy terms. We have used one

[3]We computed a value of 3.918 for the fully developed Nusselt number for Case D.1, 0.7% below that reported by Šesták and Rieger. If one solves for the eigenvalue using the eigenfunction provided by Šesták and Rieger and then uses their equation for Nusselt number, the same value of 3.918 is obtained.

[4]Several studies replicated the Šesták and Rieger results. The Case A.1 dimensionless temperature profile is replicated by Hudson et al. [55]; Bruin [56] shows the Case B.1 dimensionless temperature profile and $Nu_{m,fd}$ in agreement with Šesták and Rieger, and Davis [57] replicates $Nu_{s,fd}$ for Case B.1.

hundred terms in all our computations, which for Case A.1 adds less than 0.09% to the value computed with seventy terms at $x^* = 0.0001$.

2.4.2 Fully Developed Nusselt Numbers

The key results of this analysis are expressions for the Nusselt numbers at the stationary and moving surfaces. In the limit as $x^* \to \infty$, the Nusselt numbers converge to constant fully developed values.

The fully developed Nusselt number values for Cases A, C and D are equal to the ratio of the leading coefficients of the numerator and denominator and can be computed with only one eigenvalue. The fully developed Nusselt number values for Case B depend solely on the prescribed slip lengths as per

$$\mathrm{Nu}_{s,fd} = \frac{3(1+2b_s^*)}{2+3b_s^*+3b_{t,s}^*+6b_s^*b_{t,s}^*} \tag{2.58}$$

$$\mathrm{Nu}_{m,fd} = \frac{3(1+2b_s^*)}{1+3b_s^*+3b_{t,m}^*+6b_s^*b_{t,m}^*} \tag{2.59}$$

which, for no slip, reduce to 1.5 and 3.0, respectively, the values in the literature [56, 59] for the limiting case.

Representative values of $\mathrm{Nu}_{s,fd}$ and $\mathrm{Nu}_{m,fd}$ have been tabulated in Table 2.2. The no slip Cases A.1, B.1, C.1 and D.1, elucidate the nature of transport in Couette flow. The flow is asymmetric, and when present, the heat flux from the moving surface is much greater than that from the stationary surface. Figure 2.4 shows higher developing and fully developed Nusselt numbers at the moving surface than for the stationary surface. Consequently, when thermal slip is present at the moving surface, the reduction in Nusselt number is more pronounced than for thermal slip at the stationary surface.

The fully developed Nusselt numbers at the stationary surface are the same for Cases B.1 and B.3. Mathematically $b_{t,m}$, thermal slip on the moving surface, is not in the equation for $\mathrm{Nu}_{s,fd}$. Similarly, $\mathrm{Nu}_{s,fd}$ is the same for Cases B.2 and B.4.

Case	Slip Condition	$\mathrm{Nu}_{s,fd}$	$\mathrm{Nu}_{m,fd}$
A.1	No Slip	3.63	5.85
A.2	$b_s^* = b_{\mathrm{t,s}}^* = 0.5$	2.05	3.91
A.3	$b_{\mathrm{t,m}}^* = 0.5$	2.13	1.90
A.4	$b_s^* = b_{\mathrm{t,s}}^* = b_{\mathrm{t,m}}^* = 0.5$	1.33	1.59
B.1	No Slip	1.50	3.00
B.2	$b_s^* = b_{\mathrm{t,s}}^* = 0.5$	0.92	2.40
B.3	$b_{\mathrm{t,m}}^* = 0.5$	1.50	1.20
B.4	$b_s^* = b_{\mathrm{t,s}}^* = b_{\mathrm{t,m}}^* = 0.5$	0.92	1.09
C.1	No Slip	1.74	0
C.2	$b_s^* = b_{\mathrm{t,s}}^* = 0.5$	1.05	0
D.1	No Slip	0	3.92
D.2	$b_s^* = b_{\mathrm{t,s}}^* = 0.5$	0	3.07
D.3	$b_{\mathrm{t,m}}^* = 0.5$	0	1.40
D.4	$b_s^* = b_{\mathrm{t,s}}^* = b_{\mathrm{t,m}}^* = 0.5$	0	1.28

Table 2.2: Fully developed Nusselt numbers for selected slip lengths.

The moving surface is adiabatic for Case C and Nu_m is 0. Hydrodynamic and thermal slip on the moving surface have no effect on the flow, and Cases C.3 and C.4 would see identical flow conditions as Cases C.1 and C.2. Consequently there are only two distinct slip cases, C.1 and C.2.

Similarly for Case D, the stationary plate is adiabatic; however, unlike Case C hydrodynamic slip at the adiabatic surface does influence the flow and the flow sees four distinct slip conditions.

Case A fully developed values of Nusselt numbers at each surface have been evaluated for incremental changes to thermal and hydrodynamic slip and are plotted in Figs. 2.5 and 2.6. In both graphs, when thermal slip is zero, hydrodynamic slip at the stationary surface enhances heat transfer. Also in both graphs, $\mathrm{Nu}_{s,fd}$ increases with increasing b_s, and the

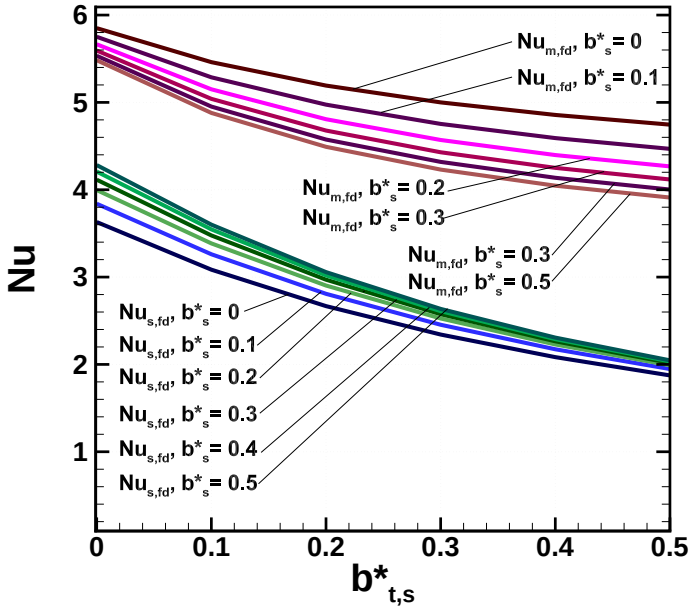

Figure 2.5: Fully developed Nusselt numbers at the stationary and moving plates, $Nu_{s,fd}$ and $Nu_{m,fd}$, versus thermal slip at the stationary plate, $b_{t,s}$, for incremental values of hydrodynamic slip at the stationary plate, b_s, for Case A, symmetric constant temperature boundary conditions.

effect of thermal slip is to decrease the Nusselt number below its no slip value. In Fig. 2.6 $\mathrm{Nu}_{m,fd}$ shows little variation with changes in b_s. Notably, $\mathrm{Nu}_{m,fd}$ shows a high sensitivity to changes in $b_{t,m}$. Since, in Couette flow, heat flux is higher at the moving surface, thermal slip at that surface plays a dominant role in heat transfer.

2.4.3 Effect of Hydrodynamic Slip

Hydrodynamic slip on the moving surface, b_m^*, is mathematically eliminated from the thermal energy equation, Eq. (2.6). Consequently, it has no effect on convective heat transfer.

When hydrodynamic slip is present at the stationary surface, the result is an increase in heat transfer at the stationary surface and a decrease at the moving surface as reflected in the Nusselt numbers per Table 3.5. For Case A, there is a net increase in the total Nusselt number. However, when the stationary surface is adiabatic, as in Case D, the

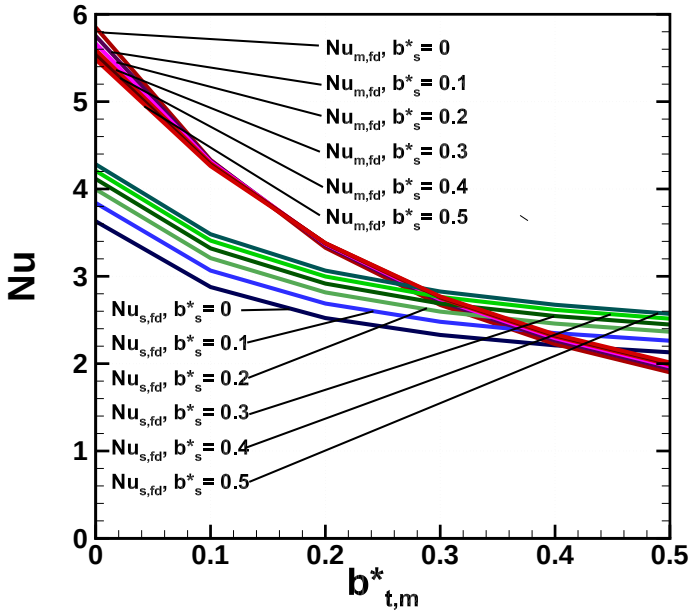

Figure 2.6: Fully developed Nusselt numbers at the stationary and moving plates, $Nu_{s,fd}$ and $Nu_{m,fd}$, versus thermal slip at the moving plate, $b_{t,m}$, for incremental values of hydrodynamic slip at the stationary plate, b_s, for Case A, symmetric constant temperature boundary conditions.

presence of hydrodynamic slip at the stationary surface decreases $\mathrm{Nu}_{m,fd}$. Notably, the effect of hydrodynamic slip in Couette flow is significantly different from findings involving heat transfer with hydrodynamic slip in Poiseuille flow [10, 29].

b_s^*	$b_{t,s}^*$	$b_{t,m}^*$	$\mathrm{Nu}_{s,fd}$	Change from No Slip Value [%]	$\mathrm{Nu}_{m,fd}$	Change from No Slip Value [%]	$\mathrm{Nu}_{\mathrm{T,fd}}$
0	0	0	3.63	0	5.85	0	9.48
0.1	0	0	3.84	5.8	5.75	-1.7	9.59
0.3	0	0	4.11	13.4	5.59	-4.4	9.71
0.5	0	0	4.28	18.0	5.48	-6.3	9.77

Table 2.3: Case A Nusselt numbers for selected values of b_s^*.

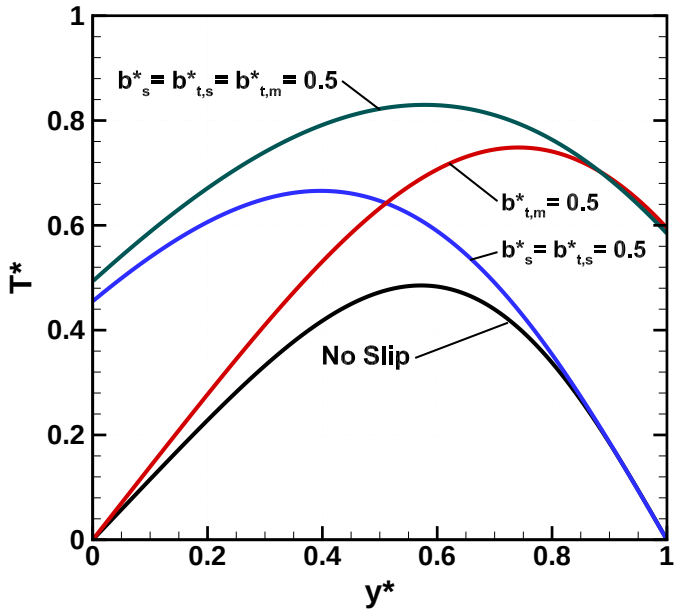

Figure 2.7: Dimensionless temperature profiles at $x^* = 0.1$, for Cases A.1-4, symmetric constant temperature boundary conditions with no slip and various values of hydrodynamic and thermal slip, b_s, $b_{t,s}$ and $b_{t,m}$.

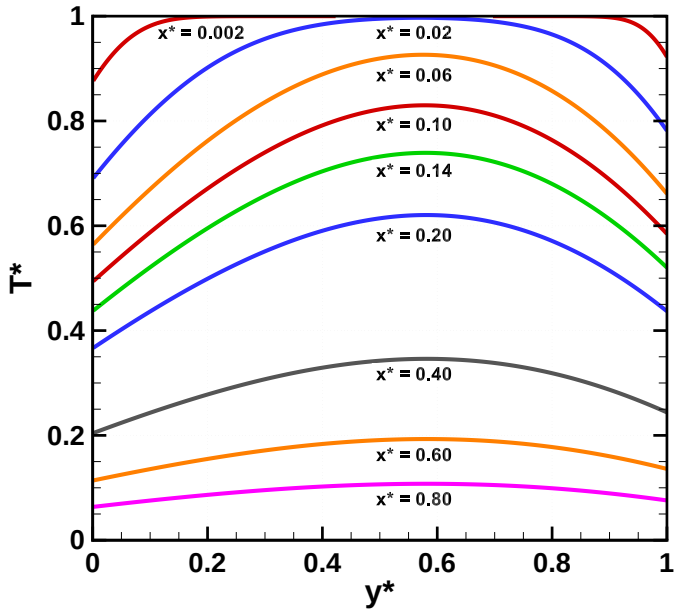

Figure 2.8: Dimensionless temperature profiles for Case A.4, symmetric constant temperature boundary conditions with hydrodynamic and thermal slip on both surfaces when $b_s^* = b_{\mathrm{t,s}}^* = b_{\mathrm{t,m}}^* = 0.5$ for various values of x^*.

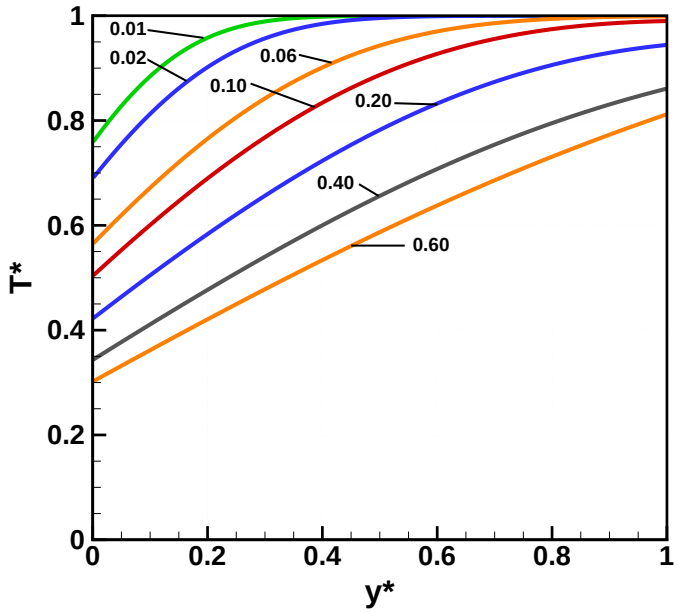

Figure 2.9: Dimensionless temperature profiles for Case B.4, asymmetric constant temperature boundary conditions with hydrodynamic and thermal slip at both surfaces when $b_s^* = b_{\mathrm{t,s}}^* = b_{\mathrm{t,m}}^* = 0$ for various values of x^*.

2.4.4 Temperature Profiles

Figure 2.7 presents dimensionless temperature profiles at $x^* = 0.1$ for Cases A.1-4. $T^* = 1$ at the entrance and asymptotically approaches 0 as $x^* \to \infty$. The no slip Case A.1 exhibits the largest change in dimensionless bulk temperature, whereas the case with slip on both surfaces, Case A.4, exhibits the smallest change. Since the heat flux at the moving surface makes a larger contribution to heat transfer, Case A.3 with thermal slip at the moving surface shows less change in dimensionless temperature than Case A.2 which has thermal slip at the stationary surface.

Figure 2.8 shows dimensionless temperature profiles for various values of x^* for Case A.4, hydrodynamic and thermal slip on both surfaces. When slip is present, not only is the gradient changing as the flow develops, but also the temperature of the fluid adjacent to the surface approaches the temperature of the liquid-solid interface.

Case B, with asymmetric constant temperature boundary conditions, demonstrates unique

behavior as $x^* \to \infty$. The dimensionless temperature profile at large x^* is defined by the first term of Eq. (2.47). For no slip, the dimensionless temperature profile asymptotically approaches $T^* = y^*$. In the presence of slip, it approaches

$$T^* = \frac{b^*_{\mathrm{t,s}} + y^*}{1 + b^*_{\mathrm{t,s}} + b^*_{\mathrm{t,m}}}, \tag{2.60}$$

as shown in Fig. 2.9.

2.4.5 Nusselt Number Plots

Total Nusselt numbers are plotted versus the dimensionless channel length in Fig. 2.10 for Cases A.1-4. For Case A.1, the total Nusselt number has the highest value both in the developing portion and the fully developed portion of the flow. The total Nusselt number for Case A.2 is greater than the total Nusselt number for Case A.3. A comparison of Case A.2 and Case A.3 highlights the different influence thermal slip has at each surface. The dimensionless bulk temperatures have comparable values in both cases; however, the heat transfer at the moving surface is much greater for Case A.2 than for Case A.3. The resulting $\mathrm{Nu_m}$ term dominates the heat transfer for Case A.2.

Nusselt numbers are plotted versus the dimensionless channel length in Fig. 2.11 for Case B.1. Note that Nu_m is negligible until $x^* > 0.06$. Since the boundary condition at the moving surface is prescribed as the inlet temperature, the temperature at the stationary surface diffuses through the flow to the moving surface and a noticeable gradient at the moving surface does not appear until $x^* = 0.06$ when Nu_m begins to increase and surpasses the value of Nu_s. Similar behavior is seen in all Case B Nu_m curves as shown in Fig. 2.12. However, for Case B.3, when thermal slip is present only at the moving surface, Nu_m remains lower than Nu_s. Notably, for Cases B.1 and B.3 and also for B.2 and B.4, the Nu_s curves overlap except in a small region near $x^* = 0.3$ where the presence of thermal slip on the moving surface influences the convection at the stationary surface slightly. Thermal entrance

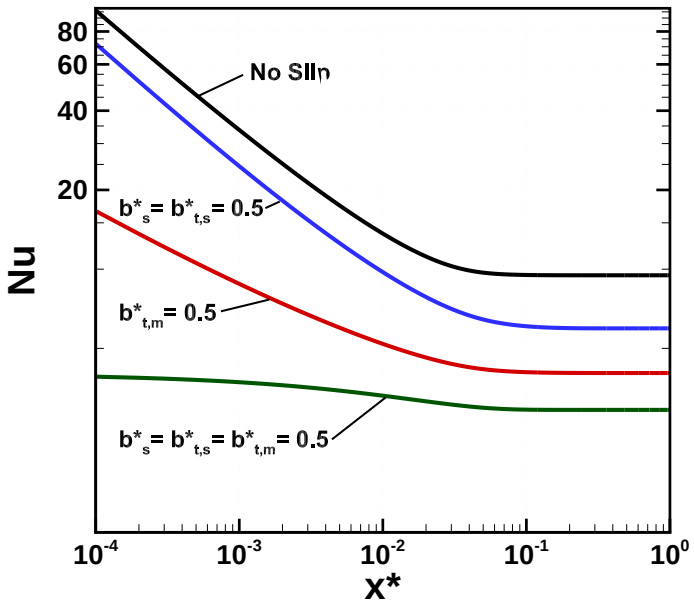

Figure 2.10: Nusselt number versus dimensionless channel length, x^*, Case A.1-4, symmetric constant temperature boundary conditions with no slip and varying values of hydrodynamic and thermal slip, b_s, $b_{t,s}$ and $b_{t,m}$.

lengths for Case B.1 are longer than those of Case A.1, and the presence of slip extends the thermal entrance lengths in Case B particularly for thermal slip on the moving surface.

The adiabatic boundary conditions in Cases C and D isolate the individual effects of hydrodynamic and thermal slip at each surface. Developing values of Nu for Cases C.1 and C.2 are similar to Nu_s of Cases B.1 and B.2. Developing values of Nu for Cases D.1-4 are similar to Nu_m of Cases A.1-4. All Case D fully developed values are lower than those of Cases A.1-4. Case D isolates the effect of hydrodynamic slip at the stationary surface which has a detrimental effect on the heat transfer and is more pronounced than in Case A.

2.5 Conclusion

Convective heat transfer in the presence of hydrodynamic and thermal slip is studied in a steady laminar plane Couette flow between parallel plates. We provide analytical expressions for temperature, bulk temperature and Nusselt number which incorporate arbitrary slip at

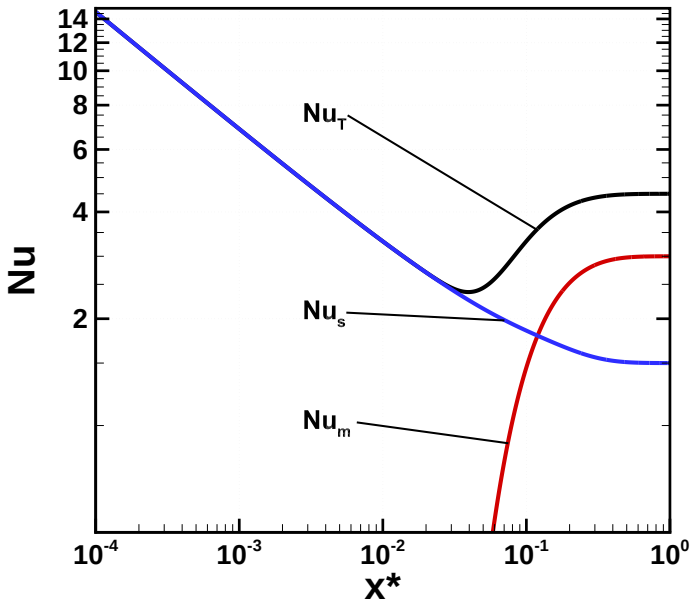

Figure 2.11: Nusselt number versus dimensionless channel length, x^*, for Case B.1, asymmetric constant temperature boundary conditions with no slip when $b_s^* = b_s^* = b_{\mathrm{t,s}}^* = b_{\mathrm{t,m}}^* = 0$.

the boundaries for a thermally developing flow. Fully developed values for Nu_s and Nu_m can be calculated with only one eigenvalue for given values of thermal and hydrodynamic slip at each surface, and for Case B the fully developed values can be calculated solely from slip values. Representative results show that the presence of hydrodynamic slip at the moving surface has no influence on convection, and the presence of hydrodynamic slip at the stationary surface enhances heat transfer at the stationary surface but decreases heat transfer at the moving surface. In all cases, the presence of thermal slip lowers the Nusselt number from the no slip value. When thermal slip is present at the moving surface in Couette flow, the reduction in heat transfer is more pronounced than for thermal slip at the stationary surface.

We also note that within the viscous sublayer of a turbulent flow, the viscous shear rate is approximated as constant as in the case of the Couette flow considered here. Since flow and heat transfer in the viscous sublayer play major roles in turbulent flows, our results may be relevant in elucidating the physics of turbulent flows over structured surfaces.

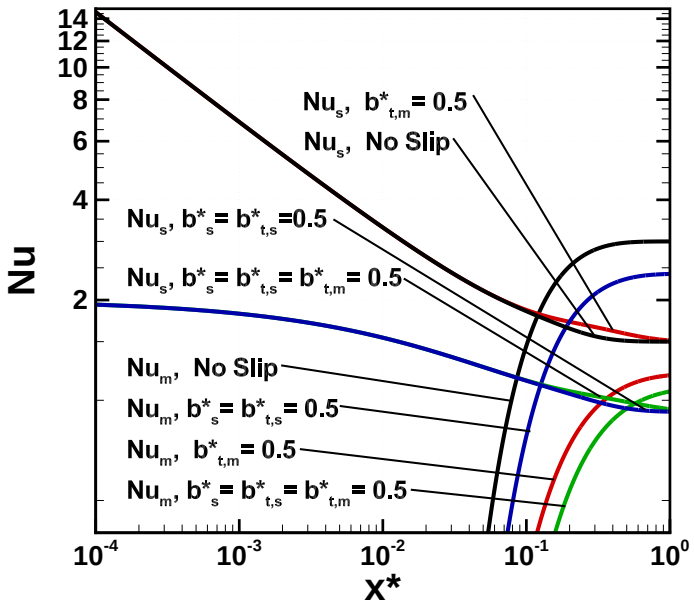

Figure 2.12: Nusselt number versus dimensionless channel length, x^*, for Case B.1-4, asymmetric constant temperature boundary conditions with no slip and varying values of hydrodynamic and thermal slip, b_s, $b_{t,s}$ and $b_{t,m}$.

While convective heat transfer has been studied here, it is important to note that other mechanisms such as caloric heating may be enhanced by the presence of hydrodynamic slip and merit further study.

Nomenclature

Ai	Airy function of the first kind
b	hydrodynamic slip length
b_t	thermal slip length
Bi	Airy function of the second kind
h	local heat transfer coefficient
H	distance between surfaces
k	fluid thermal conductivity
Kn	Knudsen number

L_c	characteristic dimension of the channel
n	direction orthogonal to the surface
Nu	Nusselt number
Pe	Peclet number
Pr	Prandtl number
Po	Poiseuille number
Re	Reynolds number
T	temperature of the fluid
T_{m}	temperature of the liquid-solid interface at the moving surface
T_{s}	temperature of the liquid-solid interface at the stationary surface
T_p	prescribed temperature of the liquid-solid interface at the surface
u	streamwise velocity
u_m	mean velocity in the streamwise direction
U_o	velocity of the liquid-solid interface at the moving surface
x	streamwise coordinate originating at the channel entrance
x_{fd}	thermal entrance length
y	spanwise coordinate originating at the stationary surface
$z(y^*)$	substitution function

Greek Symbols

α	thermal diffusivity
λ	molecular mean free path length, eigenvalue
λ^2	separation constant

λ_n	eigenvalues
ν	kinematic viscosity
ϕ_s	solid fraction

Subscripts

b	mean value
fd	fully developed
in	inlet
m	moving surface
n	index
s	stationary surface
p	prescribed value
t	thermal
T	total

Superscripts

$*$	dimensionless quantity

Chapter III

Analysis of Galinstan-Based Microgap Cooling Enhancement Using Structured Surfaces[1]

Abstract

Analyses of microchannel and microgap cooling show that galinstan, a recently developed non-toxic liquid metal that melts at -19°C, may be more effective than water for direct liquid cooling of electronics. The thermal conductivity of galinstan is nearly 28 times that of water. However, since the volumetric specific heat of galinstan is about half that of water and its viscosity is 2.5 times that of water, caloric, rather than convective, resistance is dominant. We analytically investigate the effect of using structured surfaces to reduce the overall thermal resistance of galinstan-based microgap cooling in the laminar flow regime. Significantly, the high surface tension of galinstan, i.e., 7 times that of water, implies that it can be stable in the non-wetting Cassie state at the requisite pressure differences for driving flow through microgaps. The flow over the structured surface encounters a limited liquid-solid contact area and a low viscosity gas layer interposed between the channel walls and galinstan. Consequent reductions in friction factor result in decreased caloric resistance, but accompanying reductions in Nusselt number increase convective resistance. These are

[1]This work is under review in Analysis of Galinstan-Based Microgap Cooling Enhancement Using Structured Surfaces, L. Steigerwalt Lam, M. Hodes, and R. Enright, *Journal Heat Transfer, Special Issue on Micro/Nanoscale Heat Mass Transfer*, 2014.

accounted for by expressions in the literature for apparent hydrodynamic and thermal slip. We develop a dimensionless expression to evaluate the tradeoff between the pressure stability of the liquid-solid-gas system and hydrodynamic slip. We also consider secondary effects including entrance effects and temperature dependence of thermophysical properties. Results show that the addition of structured surfaces enhances heat transfer.

3.1 Introduction

Single-phase direct liquid cooling of electronics in a microchannel configuration was first investigated by Tuckerman and Pease [49] in 1981 and, subsequently, has received remarkable attention [50, 53]. Recently, Hodes et al. [69] have shown that galinstan is a more effective coolant than water under the pressure drop and form factor constraints imposed by Tuckerman and Pease [49]. This is because the thermal conductivity of galinstan is approximately 28 times that of water and despite its lower volumetric heat capacity (ρc_p), approximately 0.45 times that of water [69], and its higher viscosity, 2.5 times that of water [70]. Overall, the increase in heat transfer coefficient more than offsets the increased caloric resistance of the system when galinstan rather than water is the coolant. Caloric thermal resistance, sometimes referred to as bulk thermal resistance, is the thermal resistance associated the bulk temperature rise of the fluid and is a function of volumetric heat capacity of the fluid, and mass flow rate [50]. It is relevant that the caloric rather than convective resistance to heat transfer is the dominant component of total thermal resistance in the case of galinstan, an observation that motivates the present study.

When a channel is textured with surfaces structured to resist wetting, a composite interface is introduced at the boundary of the flow which is comprised of liquid-solid regions where the classic boundary conditions apply and liquid-gas regions that are approximated as shear free and adiabatic. When heat is transferred to the liquid flowing over such a surface, the limited liquid-solid contact area and the lubricating gas layer between the liquid and channel wall increase convection resistance, but decrease caloric resistance relative to a

smooth channel due to *apparent* hydrodynamic and thermal slip referred to henceforth as slip. We show this to be of net benefit in the case of microgap cooling using galinstan when the available pressure difference to drive the flow is dictated by structure topography.

Galinstan is a eutectic alloy of gallium, indium and tin developed by Geratherm Medical AG (Geschwenda, Germany) [70]. It is 66.0% Ga, 20.5% In and 13.5% Sn by mass [71, 72]. Liu et al. [73] have measured the contact angle of galinstan with various materials. For the galinstan-silicon dioxide-nitrogen system, the advancing contact angle under non-oxidizing conditions has been experimentally determined to be $\theta_A = 146.8°$. This makes it possible to characterize the wetting interactions of galinstan with a structured surface, SS. Expressions for hydrodynamic and thermal slip length which are available in the literature [17, 29] allow us to characterize the slip at the composite interface. Additionally, Poiseuille number (fRe_{D_h}) and Nusselt number as function of arbitrary hydrodynamic and thermal slip lengths in a parallel plate channel have recently been developed [29, 34]. Consequently, it is possible to evaluate the enhancement to heat transfer in a flow with slip in a microgap geometry.

3.2 Previous Work

3.2.1 Structured Surfaces

The flow enhancing properties of SSs are well known. Quere [74] discusses the wetting interactions at these surfaces and the various wetting proprieties that can be induced such as superhydrophobicity or superoleophobicity. Hydrodynamic slip length expressions are used to model the velocity slip boundary condition at the surface and are available in the literature [16, 17, 23, 29, 75]. Rothstein [14] provides a review of the experimental and theoretical hydrodynamic work as of 2010.

Thermal transport over SSs has been addressed by e.g. [31, 33, 76]. In the context of rarefied gases, in 1964, Inman [34] analytically studied slip regime flow in a parallel plate channel with uniform heat flux and provided expressions for Nusselt number as function of

slip velocity and temperature jump. Enright et al. [29] studied Poiseuille flow in a parallel plate channel and developed the aforementioned Poiseuille number (fRe_{D_h}) and Nusselt number expressions; the expression for Nu reduces to those of Inman [34] and Maynes and Crockett [33] for the symmetric case.

While the main body of this paper assumes fully developed flow, the presence of an entrance region is also considered. The slip boundary conditions for SSs take the same mathematical form as the boundary conditions for rarefied gas flow in the slip regime. Several studies [77–80] have addressed entrance effects in rarefied gas flow between parallel plates. Following the work of Sparrow et al. [77], Duan and Muzychka [80] studied slip flow in the entrance region of circular and noncircular microchannels. They provide expressions for entrance length and apparent friction factor for a slip regime in a parallel plate channel which we adapt to flow over SSs in order to assess the effect of entrance length on the enhancement to heat transfer.

3.2.2 Non-constant Thermophysical Properties

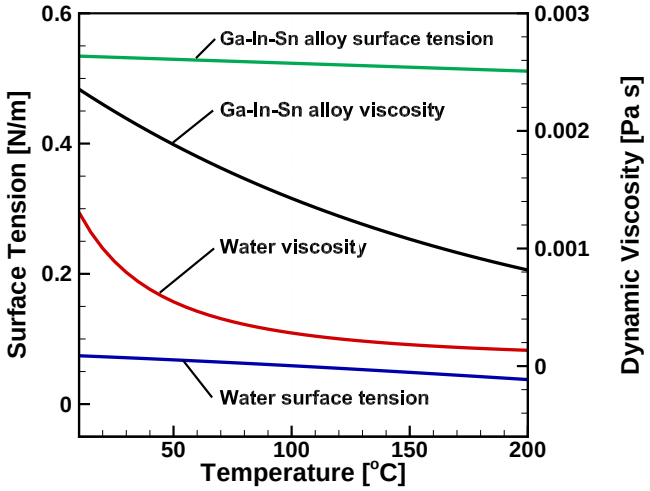

Figure 3.1: Surface tension and viscosity for water and Ga-In-Sn ternary alloy. Saturated water properties from [81]. Ga-In-Sn alloy properties from [82].

To the authors' knowledge, the effect of temperature on the thermophysical properties

of galinstan has not been studied; however, Prokhorenko et al. [82] have studied a ternary alloy of gallium, indium and tin with a similar composition, i.e., a eutectic alloy that is 67% gallium, 20.5% indium and 12% tin by mass with a melting point of 263.5 K [82]. They report expressions for the temperature dependence of viscosity, density and surface tension. Viscosity and surface tension versus temperature are shown for the Ga-In-Sn alloy and water in Fig. 3.1. The change in viscosity over this temperature range is large enough to affect caloric resistance. Prokhorenko et al. found no temperature dependence of contact angle at temperatures below 800K for contact angles of this alloy on stainless steel.

3.3 Problem Formulation

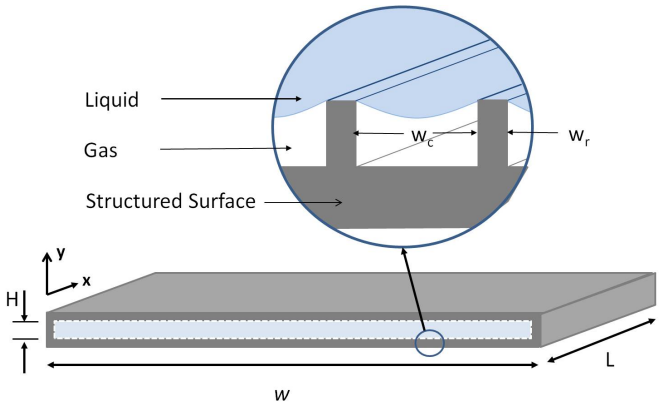

Figure 3.2: Schematic of SS microgap with height H, width w and length L. The walls of the channel are structured with ridges of width w_r and spacing $w_c + w_r$ arranged parallel to the flow in the x-direction.

The geometry under consideration here is a microgap as per Fig. 3.2. We assume the aspect ratio is high enough to model it as a parallel plate channel. Its spanwise cross-sectional area is w x H, where w is the channel width and H is the channel height. Its length in the streamwise direction is L. Channel dimensions of $L = 1$ cm and $w = 1$ cm are chosen to represent that of a silicon die, typical of thermal management applications. The top and bottom of the channel are assumed to be SSs comprised of ridges oriented parallel to the flow. The widths of the cavities and ridges of the SSs are w_c and w_r, respectively.

The coolants considered are galinstan and water. In the case of galinstan, the substrate of the channel is assumed to be silicon coated with a thin layer of silicon dioxide. To prevent the formation of a solid oxide film on the galinstan, an inert gas such as argon or nitrogen is assumed to fill the cavities below the liquid-gas interface. In the case of water, the silicon would be coated with a fluoropolymer and air would fill the cavities between the ridges. The advancing contact angle for water, fluoropolymer and air is taken to be 110°. A pressure difference across the channel, Δp_{ch}, is applied to drive the flow. A constant heat flux boundary condition is imposed along the tips of the ridges on the top and bottom surfaces of the channel. We assume hydrodynamically and thermally fully developed flow. The channel heights, which reflect realistic values for thermal management applications, have been set to maintain laminar flow as expressions are unavailable for friction factor and Nusselt number as a function of slip lengths in a turbulent regime. The SS channel heights are reduced to account for the addition of ridges with different ridge heights for galinstan and water as discussed later in this section.

Thermophysical properties of both galinstan and water are considered constant. We neglect the spanwise thermocapillary stress generated along the liquid-gas interface that would pull the liquid away from the solid-liquid interface towards the middle of the cavities and the streamwise thermocapillary stress that would pull the liquid upstream. We also assume that the evaporation and condensation along the liquid-gas interface are negligible due to the extremely low vapor pressure of galinstan ($p_v < 10^{-6}$ Pa at 500°C) [70]. In the case of water, evaporation and condensation may have a more significant effect on slip lengths. We further assume that for the purposes of calculating hydrodynamic and thermal slip lengths the liquid-gas interface is flat.

We also note that the solubility of inert gases in galinstan should be considered in the design of a galinstan SS channel which would be a closed system. Data on the gas solubility of inert gases in galinstan are unavailable. An inert gas such as nitrogen or argon would likely be absorbed by the galinstan at low temperatures and released at higher temperatures.

Allowance for this effect would need to be made in the system design, perhaps in the form of a gas reservoir adjacent to the cooled area of the galinstan loop that would be connected to the gas cavities allowing the galinstan and gas to equilibrate.

3.3.1 Structured Surface Design

The presence of SSs introduces a composite interface composed of a liquid-solid interface on the top surface of each ridge and a liquid-gas interface between them. The *apparent* discontinuity in velocity at the composite interface is modeled using Navier's slip boundary condition

$$\bar{u}_c = b \left. \frac{du}{dn} \right|_c , \tag{3.1}$$

where $\bar{u}_c$ is the apparent velocity at the composite interface, b is the apparent hydrodynamic slip length and n is the direction normal to the composite interface pointing into the liquid flow.

Analogous to the hydrodynamic conditions at the composite interface, temperature continuity is maintained at the liquid-solid interface while the liquid-gas interface is considered adiabatic. The resulting temperature at the composite interface is an area-averaged temperature which is modeled with a thermal slip boundary condition

$$\bar{T}_{ls} - \bar{T}_c = -b_t \left. \frac{\partial T}{\partial n} \right|_c , \tag{3.2}$$

where $\bar{T}_{ls}$ is the mean temperature of the liquid-solid interface, $\bar{T}_c$ is the apparent temperature of the composite interface, and b_t is the apparent thermal slip length.

3.3.1.1 Selection of Structure Geometry

A precondition for generating an apparent slip over an SS is maintaining the liquid in the Cassie state. An important failure mode is the onset of wetting due to an applied pres-

sure difference across the liquid-gas interface exceeding that corresponding to the maximum contact angle, Δp_{lg}^{max}, causing the contact line to depin. A low Δp_{lg}^{max} implies a restricted operating regime. In practice, we wish Δp_{lg}^{max} to be large to mitigate against wetting due to applied pressure differences, i.e., under pressure-driven flow conditions, and/or environmental fluctuations, such as mechanical and acoustic vibration. However, we also wish to maximize the magnitude of the hydrodynamic slip length, this being the primary goal. To understand this trade-off, we recognize that both slip and pressure stability are functionally dependent on geometry. We neglect the influence of partial wetting and interface curvature on slip. By necessity, however, we account for curvature in computing Δp_{lg}^{max}. As such this analysis offers a first order estimate for comparing the performance of different SS geometries. By balancing the pressure difference across the liquid-gas interface with the upward force of

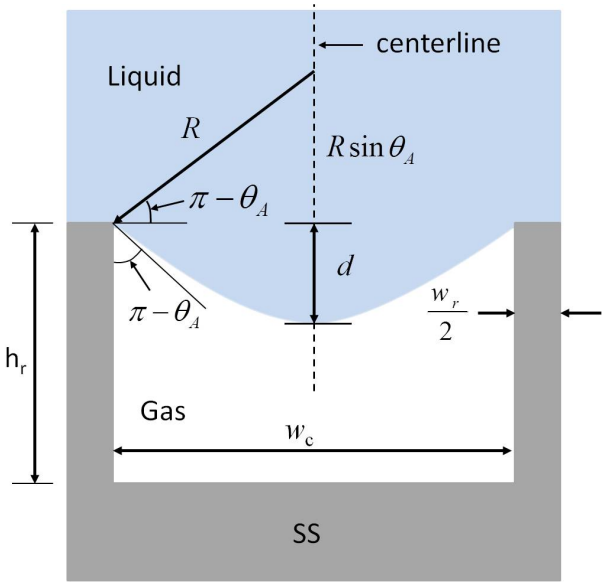

Figure 3.3: Schematic of a single unit cell of a parallel ridge structured surface in a channel. The ridges have a thickness, w_r, spacing, w_c, and height, h. The maximum deflection of the interface, d, and the advancing contact angle on the wall of the ridge are also shown.

the surface tension along the triple contact line, an expression for the maximum pressure stability for any generic geometry can be derived [83–85]. The ratio of the perimeter of the triple contact line, S, to the liquid-gas interfacial area, A, as a function of the maximum pressure and the wetting properties of a given three phase system, i.e., the surface tension

Geometry	NL	Applicable Range
Pillars [29]	$\frac{6}{\sqrt{\pi\phi_s}(1-\phi)} \sum_{n=1}^{\infty} \frac{J_1(\delta_n) \sin\left(\delta_n \sqrt{\phi_s}\right)}{\delta_n^3 J_0^2(\delta_n)}$	$\phi_s \leq 0.25$
Parallel Ridges [17]	$\frac{2 \ln\left[\sec\left(\frac{\pi}{2}(1-\phi_s)\right)\right]}{\pi(1-\phi_s)}$	$0 < \phi_s < 1$
Transverse Ridges [17]	$\frac{\ln\left[\sec\left(\frac{\pi}{2}(1-\phi_s)\right)\right]}{\pi(1-\phi_s)}$	$0 < \phi_s < 1$
Square Holes [75]	$\frac{4\left[-0.014 - 0.115 \ln(\phi_s)\right]}{\sqrt{1-\phi_s}}$	$\phi_s < 0.75$

Table 3.1: Navier-Laplace parameter as a function of surface solid fraction,ϕ_s, for various geometries (δ_n are the positive, real roots of $J_1(\delta_n) = 0$).

and contact angle,

$$\frac{S}{A} = \frac{\Delta p_{lg}^{max}}{\sigma_{lg}(\cos\pi - \theta_A)}. \tag{3.3}$$

where σ_{lg} is the liquid-gas surface tension as shown in Fig. 5.1 for a ridge geometry. Note that this expression captures the correct scaling for pillar structures, but is only exact in the limit as $\phi_s \to 0$ where ϕ_s is the solid fraction, i.e., the ratio of the liquid-solid interface area to the total projected interface area. We define a dimensionless parameter describing the relationship between the slip behavior and wetting state stability, which we call the Navier-Laplace parameter, NL. This number is solely dependent on the surface solid fraction ϕ_s and is

$$NL = b\frac{S}{A} = \frac{b\Delta p_{lg}^{max}}{\sigma_{lg}\cos(\pi - \theta_A)}, \tag{3.4}$$

where b is the hydrodynamic slip length. Equation (3.4) indicates that, for a given three phase system and structure geometry, there is an inversely proportional relationship between slip and pressure stability. Table 3.1 provides expressions for NL for pillar, parallel ridge, transverse ridge and square hole geometries. These expressions employ the nominal Stokes-flow geometric slip relations found in the literature [17, 23, 29, 75].

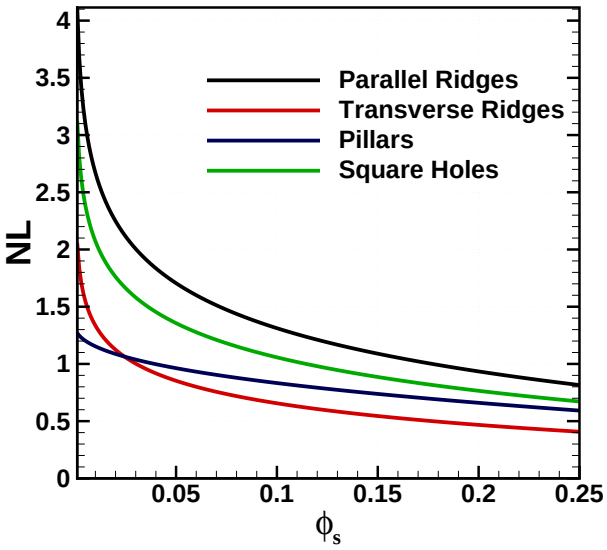

Figure 3.4: Navier-Laplace parameter as a function of surface solid fraction, ϕ_s.

In Fig. 3.4, the expressions given in Table 3.1 are plotted as a function of the surface solid fraction for $\phi_s \leq 0.25$. We observe that parallel ridges always demonstrate a larger nominal slip length for the same Δp_{lg}^{max}. This is consistent with the experimental observations of Lee et al. [22] who demonstrated larger slip lengths for parallel ridges versus pillars, while maintaining a stable Cassie wetting state at a fixed Laplace pressure of $\Delta p \approx 250$ Pa. For square holes we find that they, too, perform better than pillars, though only marginally so at larger solid fractions. Transverse ridges outperform pillars once $\phi_s \leq 0.03$. For the case of circular holes (not plotted), we expect a trend similar to that of pillars due to the fact that they become disconnected for $\phi_s \leq 0.21$ and demonstrate slip characteristics similar to pillars as $\phi_s \to 0$ [75]. Furthermore, if we explore the limit as $\phi_s \to 0$, we see that pillars are outperformed by all of the other geometry types considered here. This is not surprising considering that as the solid fraction goes to zero, the contact line perimeter for pillars also approaches zero. However, for the other geometries, which are connected, a finite length of contact line remains as $\phi_s \to 0$.

Both the hydrodynamic and thermal slip associated with a given surface geometry will

impact heat transfer. The NL parameter gives us the optimum geometry from a hydrodynamic perspective. Additionally, thermal slip should be minimized. Taking into account the thermal slip that arises due to various geometries, the ratio of hydrodynamic slip length to thermal slip length is also of interest. Enright et al. [29] show that b/b_t for pillars, transverse ridges and parallel ridges, is 3/4, 1/2 and 1, respectively. Thus, for the same reduction in heat transfer coefficient, flow across parallel ridges will see a larger drag reduction. Consequently, the aforementioned hydrodynamic and thermal considerations indicate a parallel ridge geometry will provide optimum heat transfer. Henceforth, the analysis focuses exclusively on parallel ridges.

The hydrodynamic slip length for parallel ridges is provided for low Reynolds number flows by Lauga and Stone [17] as

$$\frac{b}{l} = \frac{1}{\pi} \ln \left[\sec \left((1 - \phi_s) \left(\pi/2 \right) \right) \right], \tag{3.5}$$

where $\phi_s = w_r/(w_r + w_c)$, and $l = w_c + w_r$ is the pitch of the ridges. The thermal slip length for parallel ridges with a constant heat flux boundary condition is provided by Enright et al. [29] as

$$\frac{b_t}{l} = \frac{1}{\pi^3 \phi_s^2} \sum_{n=1}^{\infty} \frac{\sin^2 \left(n\pi\phi_s \right)}{n^3}. \tag{3.6}$$

The choice of surface parameters, ϕ_s and l, determines the amount of hydrodynamic and thermal slip that the flow exhibits with corresponding reductions in frictional drag and heat transfer coefficient, respectively.

3.3.1.2 Determination of Ridge Height

Several factors must be considered when determining the ridge height. First, there is the minimum ridge height required for the liquid to be in a thermodynamically stable Cassie state, i.e., the free energy of the system must be lower than that corresponding to the Wenzel

(wetted) state for the given geometry and liquid properties [1]. This is satisfied when [86]:

$$\frac{\cos\theta_c^*}{\cos\theta_w^*} < 1, \tag{3.7}$$

where θ_c^* is the apparent contact angle given by Cassie's relation [87], i.e.,

$$\cos\theta_c^* = -1 + \phi_s\left(\cos\theta_A + 1\right), \tag{3.8}$$

and θ_w^* is that given by Wenzel's relation [88], i.e.,

$$\cos\theta_w^* = r\cos\theta_A. \tag{3.9}$$

The roughness factor, r [88], is the ratio of the actual area of liquid-solid contact in the Wenzel state to the projected area in the horizontal plane. For parallel ridges, $r = 1 + 2h_r/l$, where h_r is the ridge height. It follows that the minimum ridge height required for stability of the Cassie state is,

$$h_r > \frac{l\phi_s\cos\theta_A + l(\phi_s - 1)}{2\cos\theta_A} - \frac{l}{2}. \tag{3.10}$$

The second consideration for determining the minimum ridge height is the maximum depth which the liquid-gas interface will protrude below the top surface of the ridges. In the case of galinstan, which has a larger contact angle than water, this becomes the critical requirement. The presence of a pressure gradient in the channel produces a meniscus with an essentially constant radius of curvature in the x-y plane and a streamwise gradient. Assuming a constant pressure in the gas phase equal to the liquid outlet pressure, p_o, the maximum meniscus curvature and therefore maximum meniscus depth will occur at the point of maximum channel pressure, i.e., the liquid inlet pressure, p_i. The triple contact line is pinned at the corner of the ridge, and the contact angle is made between the meniscus and

the vertical projection of the side of the ridge into the liquid. The depth of the meniscus can be found from geometric considerations as shown in Fig. 2,

$$d = \frac{w_c}{2\cos\theta_A}\left(\sin\theta_A - 1\right). \tag{3.11}$$

The magnitude of the advancing contact angle of the liquid determines whether Eq. (3.10) or Eq. (3.11) is of greater magnitude thus becoming the criterion for the minimum height for the ridges. For the selected geometry of $l = 10\,\mu$m and $\phi_s = 0.025$ with galinstan, the depth of the meniscus, $d_g = 2.64\,\mu$m is larger than the height required for Cassie stability, $h_{r,g} = 1.10\,\mu$m. Notably for water, due to its smaller contact angle, the opposite is true, $h_{r,w} = 9.74\,\mu\text{m} > d_w = 0.86\,\mu$m.

Finally, to assess the shear free nature of the liquid-gas interface, the shear stress in the liquid at the interface, $\tau_l = \mu_l du_l/dy$, is compared to the shear stress in the gas, $\tau_g = \mu_g du_g/dy$, where $du_l/dy \approx \bar{u}_c/b$ and $du_g/dy \approx \bar{u}_c/d$. The viscosities at 20°C for nitrogen and galinstan are 0.000018 kg/(m s) and 0.0024 kg/(m s), respectively. The ratio of shear stresses, $\tau_g/\tau_l = 0.018$ such that τ_g is small compared to τ_l.

Additionally, the Knudsen number of the gas cavity system, Kn, should be considered to determine if the gas is in the slip regime. $\text{Kn} = \lambda/L_c$, where λ is the molecular mean free path length and L_c is the characteristic length scale of the gas cavity, in this case the hydraulic diameter. For $\text{Kn} > 0.001$, the slip regime applies, and the gas will exhibit velocity slip which would contribute to shear free behavior at the interface. For nitrogen at 0°C and 1 atm, the mean free path length is 58.8 nm, so for a solid fraction of 0.025 and pitch of $10\,\mu$m, $\text{Kn} = 0.01$.

3.3.2 Thermal Resistance

Caloric and convective thermal resistances are determined based on expressions for Po and Nu provided by Enright et al. [29] and Inman [34] which are functions of hydrodynamic

and thermal slip lengths. The thermal conductivity of the surfaces at the base of the ridges is assumed to be infinite in the spanwise direction and zero in the streamwise direction. Hence, the maximum temperature of the channel occurs along the trailing edge of the parallel plate surfaces. The total thermal resistance of the microgap for a prescribed heat flux supplied to both its surfaces based upon the difference in temperature between the trailing edge of the surface at the tip of the ridge and the inlet liquid is

$$R_{Total} = R_{Cal} + R_{Conv}, \tag{3.12}$$

where the caloric thermal resistance, $R_{Cal} = 1/(\dot{m}c_p)$, the convective thermal resistance, $R_{Conv} = 1/(2wLh)$, $\dot{m}$ is mass flow rate, c_p is heat capacity and h is heat transfer coefficient at the trailing edge.

Computing caloric resistance requires an expression for the mass flow rate. In a classic channel, the mass flow rate is a function of the pressure gradient along the channel, friction factor, channel dimensions and liquid properties. In an SS channel, wetting interactions of the liquid with the surface must also be considered. Using Eq. (3.3), Δp_{lg}^{max} for ridges is

$$\Delta p_{lg}^{max} = \frac{2\sigma \cos(\pi - \theta_A)}{l(1-\phi_s)}. \tag{3.13}$$

Enright et al. [29], e.g., have provided an expression for the Poiseuille number in a parallel plate channel with symmetric surfaces as a function the dimensionless hydrodynamic slip length, $\tilde{b}$,

$$\mathrm{Po} = f\mathrm{Re}_{D_h} = \frac{96}{1+6\tilde{b}} \tag{3.14}$$

where $Re_{D_h} = \rho u_m D_h/\mu$, $\tilde{b} = b/H$, ρ is the density of the liquid, u_m is the mean velocity of the flow, $D_h = 2H$ is the hydraulic diameter of the channel and μ is the dynamic viscosity of the liquid. The inlet pressure to the channel is limited by the maximum pressure that can be supported by the meniscus such that $\Delta p_{ch} \leq \Delta p_{lg}^{max}$, where Δp_{ch}, the pressure drop in the

channel, is the difference between the inlet pressure and the outlet pressure. An expression for the mass flow rate, $\dot{m} = \rho H w u_m$, is found by substituting Eq. (3.13) into the definition of the Darcy friction factor, $f = \Delta p_{ch} 2 D_h / (L \rho u_m^2)$ to find the maximum mean velocity. The mass flow rate follows,

$$\dot{m} = \frac{(6b + H) H^2 w \rho \sigma \cos(\pi - \theta_o)}{6 L \mu l (1 - \phi_s)}. \tag{3.15}$$

The caloric resistance as a function of hydrodynamic slip length follows as

$$R_{Cal} = \frac{6 L \mu l (1 - \phi_s)}{c_p w \rho \sigma H^2 (6b + H) \cos(\pi - \theta_A)}. \tag{3.16}$$

The convective thermal resistance is found by determining an expression for the heat transfer coefficient h from $h = \mathrm{Nu} k / D_h$, where Nu is the Nusselt number, k is the thermal conductivity of the liquid. Nu is the expression from Inman [34] for symmetric hydrodynamic and thermal slip and constant heat flux at both surfaces.

$$\begin{aligned} \mathrm{Nu} =& 140 H (6b + H)^2 / \\ & (17 H^3 + 168 b H^2 + +420 b^2 H \\ & + 70 b_t H^2 + 840 b b_t H + 2520 b^2 b_t). \end{aligned} \tag{3.17}$$

The convective resistance follows as

$$\begin{aligned} R_{Conv} =& \big[168 b H (5 b_t + H) + 420 b^2 (6 b_t + H) \\ & + H^2 (70 b_t + 17 H)\big] \big/ \big[140 w L k (6b + H)^2\big]. \end{aligned} \tag{3.18}$$

Since the channel pressure difference used to calculate R_{Cal} is based on Δp_{lg}, we develop an expression for the thermal resistance in the classic channel using the same one for comparison. The total thermal resistance for a classic channel, with the SS pressure definition

and the classic values for Po and Nu is

$$R_{TotalClassic} = \frac{6L\mu l(1-\phi_s)}{c_p w\rho\sigma H^3\cos(\pi-\theta_A)} + \frac{17H}{140Lwk}. \tag{3.19}$$

3.3.2.1 Extension to an Asymmetric Channel

In order for there to be enhancement to heat transfer from the use of SSs, the thermal resistance of the SS channel must be less than that of the classic channel per the following

$$\frac{R_{ss}}{R_{cl}} < 1. \tag{3.20}$$

For a parallel plate channel with height, H, and for arbitrary heat flux supplied to its surfaces [89], the total thermal resistance is based upon the difference in temperature between the trailing edge of the surface at the tip of the ridge and the inlet liquid. Using the analysis of Nield [89] to account for asymmetric heat flux, the total thermal resistance can be expressed in the same form as Eq. (3.12) where $R_{Conv} = 2H/Nu$. For the classic channel the Nusselt number which accounts for arbitrary prescribed heat flux is available from [89].

In the presence of slip Eq. (3.20) is expressed in terms of Nusselt number and Poiseuille numbers for the SS channel,

$$\frac{35\Delta p_{cl}H^3(kL^2\mathrm{Nu}_{ss}\mathrm{Po}_{ss}\nu + 8c_p\Delta p_{ss}(2d+H)^4)}{2\Delta p_{ss}(2d+H)^3\mathrm{Nu}_{ss}(1680kL^2\nu + 17c_p\Delta p_{cl}H^4)} < 1, \tag{3.21}$$

where Δp_{ss} and Δp_{cl} are the pressure differences across the SS and classic channels, respectively.

Expressions for Po_{ss} and Nu_{ss} as functions of arbitrary hydrodynamic and thermal slip are available from Enright et al. [29].

3.4 Results and Discussion

In order to exercise our model, we have chosen a geometry which allows us to examine the fluid flow in a laminar regime with the intent of attaining a high mass flow rate in order to minimize the thermal resistance. Heat transfer in an SS channel is compared to that in a classic channel and results for galinstan and water are listed in Table 3.2.

	Galinstan SS Channel	Galinstan Classic Channel	Water Classic Channel	Water SS Channel
$H\,(\mu\text{m})$	88	96	96	76
$\tilde{b}$	0.117	N/A	N/A	0.135
$\tilde{b}_t$	0.121	N/A	N/A	0.140
Nu	6.06	8.24	8.24	5.77
Po	56.4	96	96	52.9
$\Delta p_{ch}\,(\text{kPa})$	92	92	92	5.1
$h_r\,(\mu\text{m})$	4	N/A	N/A	10
Re_{D_h}	1984	1512	1348	68
$\dot{m}\,(\text{kg/sec})$	0.0238	0.0181	0.0067	0.00034
$R_{Conv}\,(^\circ\text{C/W})$	0.009	0.007	0.194	0.219
$R_{Cal}\,(^\circ\text{C/W})$	0.142	0.186	0.035	0.705
$R_{Total}\,(^\circ\text{C/W})$	0.148	0.177	0.229	0.924

Table 3.2: Thermal resistances for galinstan and water in an SS channel and a classic channel for $l = 10\,\mu m$ and $\phi_s = 0.025$. The pressure gradient for water and galinstan in the classic channel is set equal to that of galinstan in the SS channel which is limited by the Cassie stability requirement for the galinstan-nitrogen-silicon oxide system. The pressure gradient in the water SS channel is set to that which maintains Cassie stability for the water-fluoropolymer-air system at this pitch and solid fraction.

The thermophysical properties for galinstan and water used in this study are given in Table 3.3. The channel and surface dimensions are listed in Table 3.4. The SS channel height is narrower to allow the requisite space for the structures. Twice the ridge height has been

added to the dimension of the classic channel height, H_{cl}, such that $H_{cl} = 2h_r + H_{ss}$ where h_r is the ridge height and H_{ss} is the SS channel height. The water channel ridge height is larger to maintain Cassie stability.

Property	Galinstan	Water
$T_m\,(°\text{C}\ )$	-19	0
$T_b\,(°\text{C})$	>1300	100
$\rho\,(kg/m^3)$	6440	998
$\mu\,(kg/ms)$	0.0024	0.001
θ_A	146.8° [73]	110°
$\sigma\,(N/m)$	0.5346 at 28(°C) [73]	0.073
$c_p\,(J/kgK)$	296 [69]	4184
$k\,(W/mK)$	16.5	0.60

Table 3.3: Properties of galinstan and water. Properties of galinstan evaluated at 20°C or temperature indicated and atmospheric pressure from [70] and saturated properties for water from [81].

Dimension	Value
Galinstan SS channel height, $H_{ss,g}\,(\mu m)$	88
Water SS channel height, $H_{ss,w}\,(\mu m)$	76
Classic channel height, $H_{cl}\,(\mu m)$	96
Channel length, $L\,(m)$	0.01
Channel width, $w\,(m)$	0.01
Galinstan SS ridge height, $h_{r,g}\,(\mu m)$	4
Water SS ridge height, $h_{r,w}\,(\mu m)$	10
Solid fraction, ϕ_s	0.025
Pitch, $l\,(\mu m)$	10

Table 3.4: Dimensions for channels and surfaces.

The total thermal resistance of galinstan in a parallel plate SS channel was calculated

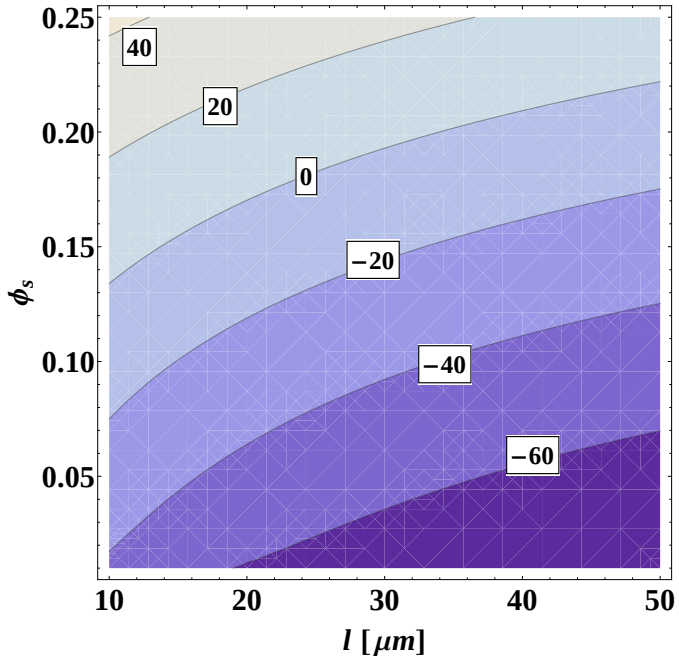

Figure 3.5: Percent change in thermal resistance of a galinstan SS channel from that of a galinstan classic channel as a function of ridge pitch and solid fraction.

and compared to that in a classic channel with the same pressure drop. Figure 3.5 shows the percent reduction in thermal resistance corresponding to the geometry of the channel surfaces in terms of pitch and solid fraction. This suggests that significant enhancement to heat transfer can be achieved by using an SS channel over a classic channel when galinstan is the heat transfer fluid.

The pressure drop in the channel is chosen to be the maximum which can be supported across the liquid-gas interface for a given pitch as per Eq. (3.13). This varies inversely with the cavity width such that it decreases as pitch increases. Fig. 3.6 shows the pressure drop corresponding to pitch in the galinstan SS channel for a fixed value of $\phi_s = 0.025$ which applies to Figs. 3.7 and 3.8.

Even though the calculations for mass flow rate take the slip into account, for all cases the mass flow rates decrease with pitch.

Figure 3.7 shows the caloric, convective and total thermal resistances versus pitch for the galinstan-based SS and classic channels with a solid fraction of $\phi_s = 0.025$. As the

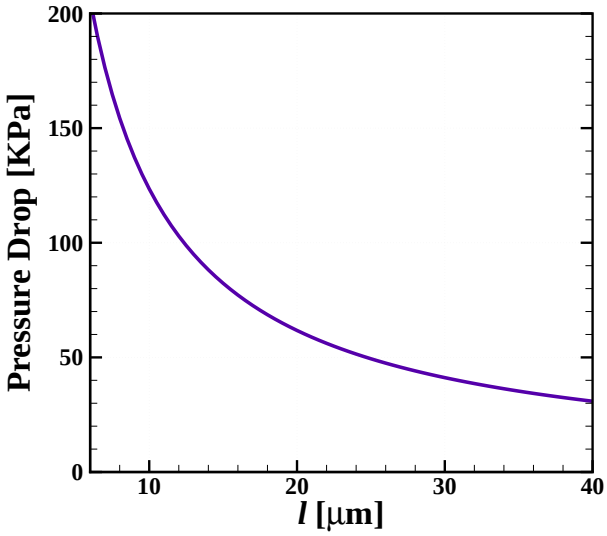

Figure 3.6: Pressure drop versus pitch in the galinstan SS channel, $\phi_s = 0.025$ also used for galinstan and water in the classic channel for comparison.

mass flow rate commensurate with the pressure drop decreases, caloric resistance rises. For lower pressure drops, the relative advantages gained by using an SS channel increase over the classic channel. However, the lowest thermal resistances of the galinstan-based system are achieved at high mass flow rates. As pitch is sufficiently decreased, hydrodynamic and thermal slip lengths approach zero and the classic and structured channels yield the same performance.

The total thermal resistances versus pitch for galinstan-based SS and classic channels and water-based SS and classic channels is shown in Fig. 3.8 for a solid fraction of $\phi_s = 0.025$. The water-based classic channel uses the same pressure drop as the galinstan-based channels. The water-based SS channel pressure drop is equal to Δp_{lg}^{max} and is the limited by the lower surface tension and lower contact angle of water; the resulting flow rate is too small to effect comparable heat transfer with the other channel scenarios. For low values of pitch, both galinstan-based channels show a lower thermal resistance than that of the water-based classic channel. At higher values of pitch, the galinstan mass flow rate drops and the resistance of the galinstan classic channel exceeds that of the water-based classic channel reflecting the

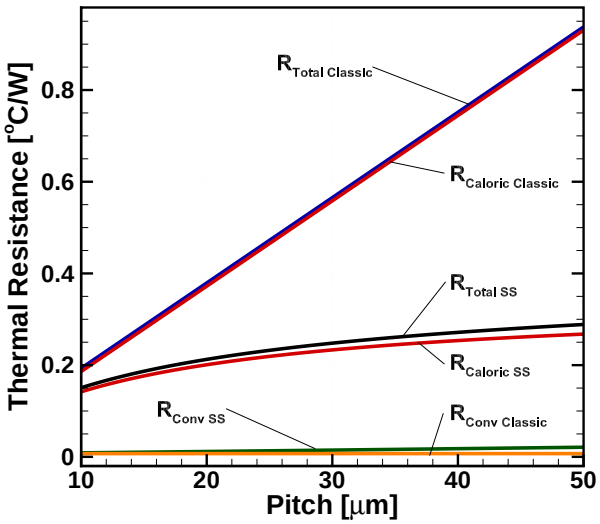

Figure 3.7: Thermal resistance versus pitch for galinstan in SS channel, $\phi_s = 0.025$ and in classic channel.

dominance of the caloric component of galinstan thermal resistance. In the galinstan-based SS channel the flow rate drops less with increased pitch and also sees less friction such that the thermal resistance remains lower.

3.4.1 Volumetric Flow Rate Advantage

The addition of ridges decreases the available channel cross-sectional area through which the liquid flows, potentially offsetting the gains from hydrodynamic slip. In order to determine the range of values of b that result in a net increase to the flow rate, the mass flow rate in the SS channel is set to be greater than the mass flow rate in the classic channel $\dot{m}_{ss} > \dot{m}_{cl}$,

$$\frac{D_{h,ss}^3}{\mathrm{Po}_{ss}\mu L} > \frac{D_{h,cl}^3}{\mathrm{Po}_{cl}\mu L}. \tag{3.22}$$

Po_{ss} is taken from Eq. (3.14) and the hydraulic diameter of the classic channel is $D_{h_{cl}} = 2(H + 2d)$. It follows that

$$H^3(H + 6b) > (H + 2d)^3. \tag{3.23}$$

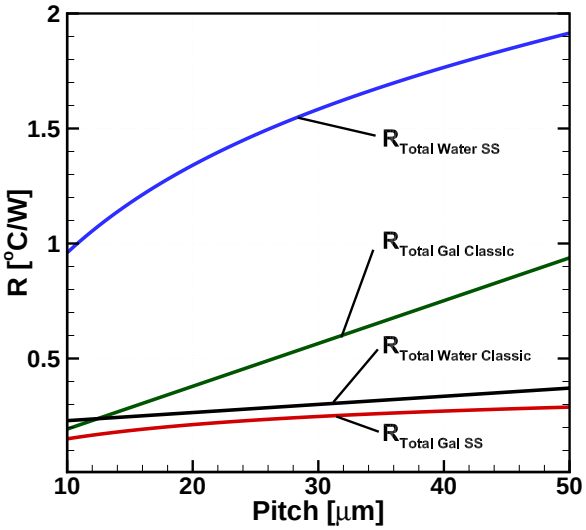

Figure 3.8: Thermal resistance versus pitch for galinstan and water in SS channel, $\phi_s = 0.025$ and in classic channel. Pressure drop corresponds to Fig. 3.6 except for that of water in the SS channel.

Eliminating the third order term on the right hand side this reduces to

$$b > \frac{2d^2 + dH}{H}. \tag{3.24}$$

For galinstan, d must be greater than the depth of the meniscus, from Eq. (3.11) and θ_A is approximated as 150°. It follows that

$$b > \frac{1}{3}\left(w_c + \frac{2w_c^2}{3H}\right), \tag{3.25}$$

which for the chosen geometry implies that $b > 3.49\,\mu$m or $\tilde{b} > 0.04$ is the range of slip length values for which the flow will see an advantage from slip. Notably when $w_c \ll H$, $b \approx w_c/3$ for galinstan. The slip length used here exceeds the minimum by a factor of 2. For water, on the other hand, the minimum ridge height required for Cassie stability would be used in Eq. (3.24) which results in a value of $b/H \geq 0.161$, a value larger than that obtained from Eq. (3.5). Consequently, there would be no volumetric advantage for water with the geometry considered here per Table 3.4.

3.4.2 Thermal Resistance through Ridges

The addition of ridges to the channel surfaces adds thermal resistance to the heat transfer path between the base of the channel and the liquid.

The total thermal resistance through the ridges is

$$R_{Ridge} = R_{cons} + R_{cond} + R_{coat} \tag{3.26}$$

where R_{cons} is the constriction resistance that results from the sudden area change that the heat flow undergoes, R_{cond} is thermal conduction resistance through the the height of ridge and R_{coat} is the thermal resistance of the thin coating on top of the ridge.

Smythe [90] developed a closed form expression for current flow through a long strip with an abrupt change in width. This was adapted by Yovanovich and Marotta [91] for a thermal spreading resistance for steady conduction in a two-dimensional channel whose width decreases from $2b$ to $2a$.

$$\begin{aligned} R_{cons} =& \frac{1}{2\pi kL}\left[\left(\epsilon + \frac{1}{\epsilon}\right)\ln\left(\frac{1+\epsilon}{1-\epsilon}\right)\right. \\ &\left. + 2\ln\left(\frac{1-\epsilon^2}{4\epsilon}\right)\right] \end{aligned} \tag{3.27}$$

where $\epsilon = a/b = \phi_s$. The above expression assumes that a and b are very small compared to the length of their respective sections which is the case here. For the selected galinstan SS geometry per Table 3.4 and assuming the thermal conductivity of silicon, the constriction resistance through the ridges for both surfaces, $R_{cons} = 0.00028\,^{\circ}\mathrm{C/W}$.

The 1D conduction resistance due to the ridge height is $R_{cond} = h_r/(2k_r\phi_s wL)$ where k_r is the thermal conductivity of the ridge, and the conduction resistance through the coating is $R_{coat} = h_c/(2k_c\phi_s wL)$ where h_c is the thickness of the coating and k_c is the thermal conductivity of the coating. The thermal resistance through the coating can be a significant component of the total depending on the material choice as many coatings commonly

used on SSs have low thermal conductivities. The silicon dioxide coating used here has $k_c = 1.2\,W/mK$. For the galinstan SS channel selected geometry in Table 3.4 the thermal resistance through the silicon ridges is 0.0049 °C/W and the thermal resistance through the 20 nm silicon dioxide coating is 0.0031 °C/W. For a water channel, using a 20 nm fluoropolymer coating with a thermal conductivity of $k_c = 0.25\,W/mK$, $R_{coat} = 0.0148$ °C/W.

The total thermal resistance through the ridges for the galinstan SS channel is $R_{Ridge} = 0.0083$ °C/W.

3.4.3 Entrance Length Effects

The analysis thus far has made the assumption of fully developed flow in the SS and classic channels. The presence of hydrodynamic slip on the channel surfaces increases the entrance length and reduces the magnitude of the pressure gradient in the entrance region. If the entrance length of the channel is a significant portion of the channel length, this region must be taken into account.

The apparent Fanning friction factor, f_{app}, is used to represent the total friction in the channel including the entrance region and is based on the total flow resistance from $x^+ = 0$ to x^+. It is used in the dimensionless quantity, apparent friction factor-Reynolds number product, $f_{app}\mathrm{Re}_{D_h}$. The additional pressure drop in the entrance region has two components: the pressure drop due to the change in momentum of the flow and the pressure drop due to the incrementally higher friction in the developing flow. In comparison to the fully developed assumption, when entrance effects are considered, the velocity of the flow will decrease and the caloric resistance will increase for a prescribed pressure drop. Additionally, the presence of a hydrodynamically developing boundary layer in the entrance region will cause an increase in the local Nusselt number in that region. However, this is not considered in the convective resistance in the current analysis which uses the heat transfer coefficient calculated at the trailing edge of the channel surface.

Expressions for entrance length, L_{hy}, and apparent friction factor, $f_{app}\mathrm{Re}_{D_h}$, are available

in the literature for classic channels [92]. Shah and London [93] provide an expression for $f_{app}\mathrm{Re}_{D_h}$ as a function of dimensionless channel length, x^+ which accounts for the momentum change and skin friction in the entrance region for a parallel plate channel.

Duan and Muzychka [80] provide an expression for entrance length which accounts for hydrodynamic slip,

$$\frac{L_{hy}}{D_h} = \frac{0.315}{0.0175\mathrm{Re}+1} + 0.0112\mathrm{Re}(1+6.7\mathrm{Kn}'-37(\mathrm{Kn}')^2), \tag{3.28}$$

where $\mathrm{Kn}' = \mathrm{Kn}(2-\sigma)/\sigma$ is the dimensionless slip length. They also provide an expression for the apparent friction factor Reynolds number product, $f_{app}\mathrm{Re}$, for parallel plate channel in a slip flow regime.

$$f_{app}\mathrm{Re}_{D_h} = \frac{24}{1+12\mathrm{Kn}'} + \frac{1}{5x^+(1+12\mathrm{Kn}')^2} - \sum_{i=1}^{\infty} \frac{(3-e^{(-16\alpha_i^2 x^+)})e^{(-16\alpha_i^2 x^+)}}{\alpha_i^2 x^+(1+(12\mathrm{Kn}')+16(\alpha_i^2\mathrm{Kn}')^2)} \tag{3.29}$$

where $x^+ = (x/D_h)\,/\,(u_m D_h/\upsilon)$ is the dimensionless channel length and α_i are eigenvalues found from the eigencondition,

$$\tan(\alpha_i) = \frac{\alpha_i}{1+4\alpha_i^2\mathrm{Kn}'}. \tag{3.30}$$

Because the analytical models for rarefied gas flow in the slip regime use slip boundary conditions and continuum flow equations analogous to those of SSs, these expressions can be used with an equivalent slip length to estimate the entrance length and $f_{app}\mathrm{Re}$ for galinstan in a channel lined with SSs. It is noted that these expressions only apply to parallel plate channels with symmetric slip.

The expression for equivalent slip length can be extracted from the slip boundary condi-

	SS channel	Classic channel
Entrance length [m]	0.0042	0.0032
fRe for fully developed flow assumption	56.4	96
$4f_{app}$Re [80]	64.7	113
$R_{caloric}$ based on fully developed flow fRe [°C/W]	0.142	0.186
$R_{caloric}$ based on f_{app}Re [°C/W]	0.163	0.218
Change from fully developed assumption [%]	14.8	17.2

Table 3.5: Entrance length and $f_{app}\mathrm{Re}_{D_h}$ values from Eq. (3.29) for galinstan-based SS and classic channel with dimensions from Table 3.4.

tion of Duan and Muzychka [80], which is used to derive their expressions,

$$U(1, x^+) = -\frac{2-\sigma}{\sigma} 4Kn \left.\frac{\partial U}{\partial \eta}\right|_{\eta=1}. \tag{3.31}$$

Eq. (3.31) is equivalent to the slip boundary condition in the SS channel as defined by Eq. (3.1) rewritten here in terms of $u(x, y)$,

$$u(x, H) = -\tilde{b} \left.\frac{\partial u}{\partial y}\right|_{y=H}. \tag{3.32}$$

By converting from the dimensionless coordinates, $\eta = y/h$, $U(\eta, x^+) = u(\eta, x^+)/\bar{u}$, and $H = 2h$, Kn' can be expressed in terms of the apparent dimensionless hydrodynamic slip length, $\tilde{b}$ as:

$$\mathrm{Kn}' = \frac{\tilde{b}}{2}. \tag{3.33}$$

Substituting Eq. (3.33) into Eq. (3.29), a value for the apparent friction factor can be found by iterating. Taking into account that the Fanning friction factor is 1/4 of the Darcy

friction factor, the mean velocity then is found from

$$u_m = \frac{\Delta p_{lg} {D_h}^2}{2 f_{app} \mathrm{Re}_{D_h} \mu L} \tag{3.34}$$

and the caloric resistance in terms of the apparent friction factor becomes,

$$R_{caloric} = \frac{f_{app} \mathrm{Re}_{D_h} L \mu l (1 - \phi_s)}{4 c_p H^3 w \sigma \rho \cos(\pi - \theta_A)}. \tag{3.35}$$

Equation (3.35) can be used to calculate the caloric resistance in a classic channel using Eq. (3.29) where $\mathrm{Kn}' = 0$. Values for the caloric resistance with a fully developed flow assumption and with an apparent friction factor assumption are listed in Table 3.5 for flow in an SS channel and classic channel. Channel and surface dimensions are taken from Table 3.4.

In the present geometry, the length of the entrance region is significant in the both channels, and the presence of slip extends the length of the entrance regions. Since the flow is calorically dominated, the effect on caloric resistance is an important one. Since the contribution to total resistance from convective resistance is small, the analysis here can be considered a conservative estimate of the impact on total thermal resistance.

3.4.4 Temperature Dependence of Thermophysical Properties

To approximate the changes to thermal resistance that would occur as a result of temperature change, the thermophysical properties of the Ga-In-Sn alloy studied by Prokhorenko et al. [82] were used to calculate the thermal resistance at 20°C and 40 °C. To maintain laminar flow, the pitch of the structures was altered. Table 3.6 shows the changes to caloric and total resistance for a water-based classic channel and the Ga-In-Sn alloy-based SS channel that result from changes in viscosity, surface tension and density due to temperature. The changes in viscosity both in water and the liquid metal alloy significantly impact the flow rate and thus caloric resistance. The magnitude of the change is higher for water. However,

	Water Classic Channel			Ga-In-Sn Alloy SS Channel		
Temperature (°C)	20	40	% Change	20	40	% Change
$\mu\,(kg/ms)$	0.001	0.0006	-40.00	0.0022	0.002	-9.09
$\rho\,(kg/m^3)$	998	992	-0.60	6363	6354	-0.14
$\sigma\,(N/m)$	0.073	0.0695	-4.79	0.5331	0.5306	-0.47
Po	96	96		55.3	55.3	
Nu	8.24	8.24		5.97	5.97	
Δp_{ch}	50.8	50.6	-0.39	50.8	50.6	0.39
Re_{D_h}	748	2056	175	1719	2067	20.27
R_{Conv} (°C/W)	0.194	0.194	0	0.011	0.011	0
R_{Cal} (°C/W)	0.064	0.039	-39.35	0.179	0.163	-8.53
R_{Total} (°C/W)	0.258	0.233	-9.74	0.190	0.174	-8.03

Table 3.6: Thermal resistance change with temperature change for Ga-In-Sn Alloy-based SS channel and water classic channel for $l = 18\mu$m considering temperature dependence of viscosity, density and surface tension. Properties of Ga-In-Sn Alloy from [82] and saturated properties for water from [81].

since caloric resistance is a lower percentage of the total thermal resistance for water, the changes in the resistance for both channels are on the same order.

3.5 Conclusion

We provide a methodology for assessing heat transfer enhancement resulting from apparent slip. Galinstan cooling in a microgap geometry lined with SSs has been studied and compared to galinstan in a classic channel and water in both classic and SS channels. Substantial reductions in thermal resistance can be achieved by incorporating SSs into the microgap surface, and the extent of the reduction depends on channel and surface geometry. Results show that the convective thermal resistance in galinstan is a small percentage of the total thermal resistance and that galinstan-based cooling is calorically dominated.

Convective resistance is 6.34% and 3.95% of total thermal resistance for the galinstan-based SS channel and the classic channel, respectively. Notably, the enhancement to heat transfer gained from drag reduction in the galinstan-based system outweighs the reduction in convective heat transfer resulting in a net improvement.

Galinstan-based micro/minigap coolers are a promising alternative to water-based single phase cooling. We have demonstrated for fully developed laminar flows with constant slip coefficients, that significant reductions in thermal resistance are possible particularly for systems that are pumping pressure limited. The presence of an entrance length is also considered, and while caloric resistance is increased by comparison to a fully developed flow, SSs still show significant enhancement to heat transfer. The caloric resistance is 25% lower in the SS channel than in the classic channel when the entrance length is taken into account. The temperature dependence of thermophysical properties of a comparable liquid metal alloy are used to estimate the effect of temperature on heat transfer in galinstan flow demonstrating a positive correlation. The percent change in both coolants with a 20°C increase is comparable; notably, the caloric resistance in galinstan is 22% lower than water at the higher temperature.

We discuss several methods to assess the effect on transport due to the addition of SSs. The NL parameter allows the comparison of surface geometries to optimize the trade off between pressure stability and hydrodynamic slip. The additional height of structures reduces the available channel cross-sectional area and adds an additional resistance to the heat transfer path. This is taken onto account in an analysis of impact to the volumetric flow which estimates a minimum value of 0.04 for $\tilde{b}$ for velocity enhancement in the galinstan system. Analysis of the thermal resistance through the surface structures shows $R_{Ridge} = 0.0083\,^{\circ}\mathrm{C/W}$ which is small compared to the total and on the same order as the convective resistance for the galinstan system.

Future work will examine the effect of evaporation and condensation on thermal slip length and the effect of meniscus curvature on thermal slip length. While laminar flow has

been studied here, it is important to note that thermal resistance of galinstan flow could potentially be further reduced in a turbulent regime, and merits further study.

Nomenclature

b	apparent hydrodynamic slip length [m]
b_t	apparent thermal slip length [m]
$\tilde{b}$	dimensionless apparent hydrodynamic slip length
$\tilde{b}_t$	dimensionless apparent thermal slip length
c_p	specific heat at constant pressure [J/(kgK)]
D_h	hydraulic diameter [m]
f	Darcy friction factor
h	heat transfer coefficient [W/(m^{2}K)]
h	structure height [m]
H	channel height [m]
k	thermal conductivity [W/(mK)]
Kn	Knudsen number
l	ridge pitch [μm]
L	channel length [m]
L_c	characteristic length [μm]
$\dot{m}$	mass flow rate [kg/s]
n	direction normal to channel surface, index
Nu	Nusselt number
p	pressure [Pa]
p_v	vapor pressure [Pa]
Po	Poiseuille number (fRe_{D_h})
r	roughness factor
R	radius of curvature [m]

R	thermal resistance [°C/W]
Re_{D_h}	Reynolds number
T	temperature [°C]
u	velocity [m/s]
w	interior channel width [m]

Greek Symbols

λ	molecular mean free path length [μm]
μ	viscosity [kg/(ms)]
ϕ_s	solid fraction
ρ	density [kg/m^3]
θ_A	advancing contact angle [radians]
θ_c^*	apparent Cassie contact angle [radians]
θ_w^*	apparent Wenzel contact angle [radians]

Subscripts

c	composite interface, coating, cavity
i	inlet
lg	liquid-gas
ls	liquid-solid
m	mean value
o	outlet
r	ridge

Chapter IV

Effect of Evaporation and Condensation at Menisci on Apparent Thermal Slip [1]

Abstract

We semi-analytically capture the effects of evaporation and condensation at menisci on apparent thermal slip lengths for liquids suspended in the Cassie state on ridge-type structured surfaces using a conformal map and convolution theory. An isoflux boundary condition is prescribed at solid-liquid interfaces and a constant heat transfer coefficient or isothermal one at menisci. We assume that the gaps between ridges, where the vapor phase resides, are closed systems; therefore, the net rates of heat and mass transfer across menisci are zero. The reduction in apparent thermal slip length due to evaporation and condensation relative to the limiting case of an adiabatic meniscus as a function of solid fraction and interfacial heat transfer coefficient is quantified in a single plot that is validated by numerical simulations. Results suggest that interfacial evaporation and condensation need to be considered in the design of microchannels lined with structured surfaces for direct liquid cooling of electronics applications, and a quantitative means to do so is elucidated. The result is a decrease in thermal resistance relative to the predictions of existing analyses which neglect them.

[1] This work is under review in "Effect of Evaporation and Condensation at Menisci on Apparent Thermal Slip," M. Hodes, L. Steigerwalt Lam, S. MacLachlan, and R. Enright, *Journal Heat Transfer*, 2014.

4.1 Introduction

A sessile droplet on a structured surface characterized by periodic length scales that are small compared to the capillary length may be stable in the Cassie state, where solid-liquid contact is confined to the tips of the structures [1]. A liquid flowing over a structured surface may also be in this state, which we assume here and depict in Fig. 4.1 for ridge-type structures. The necessary criteria are provided elsewhere [3]. The solid-liquid interface is subjected to the no-slip boundary condition, but lubrication is achievable because low shear stress may be maintained at the meniscus (liquid-vapor interface). Heat is supplied to the liquid primarily through the solid-liquid interface.

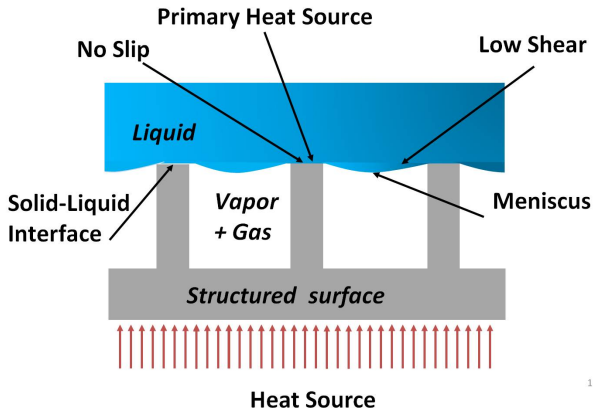

Figure 4.1: Liquid in Cassie state on ridge-type structures.

Trapping a flowing liquid in the Cassie state is envisioned for enhanced microchannel cooling of electronics [3, 94]. This reduces the caloric resistance, $1/(\dot{m}c_p)$, to heat transfer, but, simultaneously, degrades the effective heat transfer coefficient. To evaluate the efficacy of the enhancement it is necessary to capture the beneficial effects of condensation and evaporation along menisci on apparent thermal slip length when a volatile coolant such as water is utilized.

We consider a periodic array of ridges of width $2a$, of pitch $2d$ and centered about the origin and assume that menisci are flat as per the semi-infinite domain shown in Fig. 4.2. The composite interface corresponds to the $y = 0$ boundary of the domain and includes

the solid-liquid interface and the meniscus. Solid fraction (ϕ) equals the area fraction of the solid-liquid portion of the composite interface, a/d. The temperature field is symmetric about $x = 0$ and $x = d$. We assume that the gaps between ridges, where the vapor phase resides, are closed systems[2]. This is true, when, e.g., ridges reside in a trench on a substrate over which liquid flows. We consider steady-state conditions; therefore, the net rates of heat and mass transfer into the meniscus are zero. Thermophysical properties are assumed to be constant.

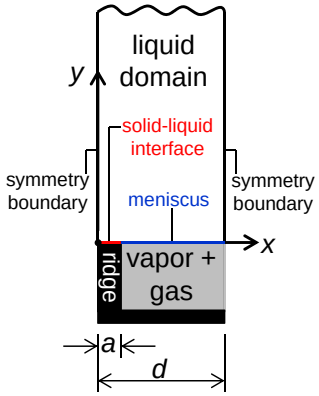

Figure 4.2: Liquid domain and ridge and vapor region beneath it.

The Reynolds number characterizing flow near a composite interface in the limit as solid fraction approaches zero is $\mathrm{Re_c} = \rho \bar{w}_c a/\mu$, where w is streamwise velocity, the overbar denotes a mean quantity, the subscript c denotes the composite interface, and ρ and μ are liquid density and viscosity, respectively. More generally, $\mathrm{Re_c}$ can't exceed $\rho \bar{w}_c d/\mu$. The corresponding Pclet number is $\mathrm{Pe_c} = \mathrm{Re_c Pr}$, where Pr is the Prandtl number of the liquid. At pitches characterizing structured surfaces, $\mathrm{Re_c}$ and $\mathrm{Pe_c}$ approach zero in most applications. Thus, as we assume here, transport is diffusive, neglecting viscous dissipation, and the temperature field is governed by Laplace's equation for the "inner problem."

There is a distinction between the true temperature profiles, $T(x, y, z)$ and $T(x, y)$ for ridges oriented parallel and transverse to the streamwise direction, respectively, and those averaged over the width of the domain, d, $\bar{T}(x, z)$ and $\bar{T}(x)$ for parallel and transverse

[2]The "vapor" phase normally has vapor and noncondensable gas components.

ridges, respectively. However, the (maximum) length scale for the distance normal to the composite interface to which it applies is d. We assume that length scales characterizing the "outer problem," e.g., boundary layer thickness in an external flow, are large compared to d. Then, heat flux is constant as $y \to \infty$ in the inner problem, as it is within the linear region of the temperature profile of the outer one. We further assume that $\partial^2 T/\partial x^2 \sim \partial^2 T/\partial y^2 \gg \partial^2 T/\partial z^2$ in the inner problem such that it is governed by the two-dimensional form of the Laplace equation. This is precisely true for a fully-developed internal flow over parallel ridges subjected to a constant heat flux at the solid-liquid interface (q''_{sl}) and for transverse ridges. However, our analysis assumes symmetry boundary conditions in x; therefore, it only applies to flow over transverse ridges when the linear component of the streamwise temperature change may be ignored. The preceding discussion is restricted to laminar flows due to the minute length scales associated with viscous sublayers in turbulent flows.

Apparent slip results from the interaction of liquid flow with regions of solid-liquid contact and menisci. The no-slip boundary condition applies at solid-liquid interfaces, but not along menisci; therefore, lubrication may be realized in microfluidic conduits. The apparent hydrodynamic slip length (b), subsequently referred to as the slip length, relates the streamwise velocity averaged over the width of the domain to its gradient at the composite interface as per [7]

$$\bar{w}_c = b \left. \frac{\partial \bar{w}}{\partial y} \right|_c . \tag{4.1}$$

Analogously, the apparent thermal slip length (b_t), also referred to as the temperature jump length and subsequently referred to as the thermal slip length, relates the difference between the mean temperatures of the solid-liquid and composite interfaces to the gradient of $\bar{T}(y)$ at the composite interface as per

$$\bar{T}_{sl} - \bar{T}_c = -b_t \left. \frac{\partial \bar{T}}{\partial y} \right|_c , \tag{4.2}$$

where the subscript sl denotes the solid-liquid interface, where a constant heat flux is pre-

scribed. (Thermal slip length may also be based upon the maximum temperature of the solid-liquid interface.) We note that as per the Leibniz Rule $\partial\bar{T}/\partial y\big|_c$ equals the mean heat flux at the composite interface which, in turn, as per an energy balance on the domain equals $dT/dy|_{y\to\infty}$.

Slip lengths and thermal slip lengths follow from the solution to the inner problems and capture perturbations to the velocity and temperature fields due to structured surfaces. Assuming a flat and shear-free meniscus, expressions for slip length were developed by Lauga and Stone [17] for parallel and transverse ridges and by Davis and Lauga [95] and Enright et al. [29] for pillars[3]. More generally, Ybert et al. [23] developed scaling laws that consider meniscus curvature and viscous dissipation in the gas phase.

Analytical results for thermal slip length for isoflux and isothermal solid-liquid interfaces and adiabatic menisci were developed by Enright et al. [29] for ridge- and pillar-type structures based upon expressions for thermal spreading resistances [35]. Ng and Wang [36] semi-analytically computed thermal slip lengths for isothermal, ridge-type structures as a function of vapor-phase to liquid-phase thermal conductivity and ridge depth when isothermal surfaces bounded the vapor phase. When the cavity depth is shallow compared to structure spacing, conduction through the vapor phase can reduce the thermal slip length relative to the case of an adiabatic meniscus. For cavity depths on the order of the spacing of the structures and larger, conduction through the gas has negligible impact on slip length. No effort is made to account for this effect here. Ng and Wang [36] also semi-analytically computed slip lengths for an isothermal surface with adiabatic circular or square holes. The preceding results are based on pure diffusion in the aforementioned inner problem. Maynes and Crockett [33] analytically studied Poiseuille flow in a parallel plate channel lined with parallel ridges subjected to a constant heat flux by solving the thermal energy equation rather than the Laplace equation, thereby accounting for advection. They developed a closed form

[3]For pillar-geometry structures, the velocity and temperature fields in the inner problems are three-dimensional; therefore, velocities and temperatures are averaged over areas rather than line segments to compute slip lengths.

solution for the local Nusselt number in agreement with [29] and provide an expression for thermal slip length based on it. Finally, Cowley et al.[96] account for the effects of axial conduction in a numerical study of Poiseuille flow in a parallel plate channel lined with transverse ridges. Their results elucidate when axial conduction is important and when diffusion-based analyses apply as a function of the relevant dimensionless parameters.

We capture the effects of evaporation and condensation along the meniscus on thermal slip length when the tips of ridge-type structures are isoflux. Significantly, when heat is transferred from the solid-liquid interface into the liquid, evaporation occurs along the relatively hot portion of the meniscus adjacent to the triple contact line and condensation elsewhere. Therefore, a fraction of the heat entering the domain conducts through the liquid to the relatively hot portion of the meniscus, drives evaporation, convects through the vapor-phase and is transported back into the liquid by condensation. This decreases thermal slip length relative to the limiting case of an adiabatic meniscus, except in the case of a non-volatile liquid, e.g., galinstan. This has ramifications to the efficacy of using structured surfaces to reduce the thermal resistance of microchannel cooling of microelectronics [3].

In the general case, we prescribe solid fraction and the dimensionless interfacial heat transfer coefficient at the meniscus, $\tilde{h}$. Then, the limiting case of an isothermal meniscus ($\tilde{h} \to \infty$) is addressed. We note that thermal slip lengths are geometric parameters only in the limits of an adiabatic or isothermal meniscus.

Macroscopic parameters, e.g., Poiseuille and Nusselt numbers, follow by imposing the boundary conditions given by Eqs. 4.1 and 4.2 on the convective transfer equations governing the outer problem. These govern the velocity and temperature fields averaged over the appropriate length (e.g., ridge pitch) or area (e.g., that bounded by symmetry lines surrounding a pillar); see, e.g., Lam et al. [3]. By implication, the Nusselt number is a function of the thermal slip length, and its value computed from the analysis herein rather than that for an adiabatic meniscus should be utilized. Subsequently, a microchannel heat sink exploiting the favorable effects of liquid flowing over textured surfaces may be optimized

as per the analysis of Lam et. al [3].

We note that when the Knudsen number characterizing an internal gas flow is between about 0.001 and 0.01 the continuum forms of the convective transfer equations apply, but the wall boundary conditions which account for molecular slip are of the same form as Eqs. 4.1 and 4.2 [11]. Therefore, expressions in the rarefied gas and microflow literature for Poiseuille number (see, e.g., Duan and Muzychka [80]) and Nusselt number (see, e.g., Colin [12]) apply to liquid flows exhibiting apparent slip. In both classes of problems the effects of slip vanish as the ratio of the slip length to the length scale for the outer problem approaches zero. Hence, since apparent slip lengths scale with structure pitch [23], itself on the order of microns, apparent slip is relevant in laminar microchannel flows and turbulent flows [14].

4.2 Analysis

We organize this section according to the type of boundary condition imposed at the meniscus. First, we consider it adiabatic. Then, we prescribe a finite heat transfer coefficient. Finally, we consider it isothermal. The solid-liquid interface is isoflux.

4.2.1 Adiabatic Meniscus

As per the result of Enright et al. [29], for an adiabatic meniscus, dimensionless thermal slip length, $\tilde{b}_t = b_t/(2d)$, is

$$\tilde{b}_t = \frac{1}{\pi^3 \phi^2} \sum_{n=1}^{\infty} \frac{\sin^2(n\pi\phi)}{n^3}. \tag{4.3}$$

4.2.2 Finite Heat Transfer Coefficient at Meniscus

The two-dimensional temperature field is governed by Laplace's equation,

$$\nabla^2 T = 0, \tag{4.4}$$

subjected to

$$\frac{\partial T}{\partial y} = -\frac{q''_{sl}}{k} \text{ for } 0 < x < a,\ y = 0 \tag{4.5}$$

$$\frac{dT}{dy} = -\frac{a}{d}\frac{q''_{sl}}{k} \text{ for } 0 < x < d,\ y \to \infty \tag{4.6}$$

$$\frac{\partial T}{\partial y} = \frac{h}{k}\left(T - \bar{T}_{lv}\right) \text{ for } a < x < d,\ y = 0 \tag{4.7}$$

$$\frac{\partial T}{\partial x} = 0 \text{ for } x = 0,\ y > 0 \tag{4.8}$$

$$\frac{\partial T}{\partial x} = 0 \text{ for } x = d,\ y > 0. \tag{4.9}$$

where $\bar{T}_{lv}$ is the mean temperature of the meniscus and k is the thermal conductivity of the liquid. Implicit in the assignment of Eq. 4.7 to the meniscus is the assumption of a uniform pressure on the vapor side of it that corresponds to the saturation pressure associated with $\bar{T}_{lv}$. While local evaporation and condensation occur, the net heat and mass flows across the meniscus are zero. Hence, all of the heat entering the domain at the solid-liquid interface is removed by the sensible temperature rise of the liquid, and the rate of heat leaving the domain as $\tilde{y} \to \infty$ equals that through the solid-liquid interface as per Eq. 4.6.

Equation 4.6 implies that the rate of heat entering the domain at the solid-liquid interface equals that leaving it by conduction as $y \to \infty$. We develop the dimensionless parameter that must be small compared to unity to justify ignoring the heat advected out of the domain. Accordingly, we consider the domain shown in Fig. 4.2, with the exception that it is finite rather than semi-infinite. Its height is d, the maximum length scale required for the temperature field to become uniform in x in the inner problem, and it is of depth dz. For fully-developed flow, the rate of heat advected out of the domain is

$$q_{adv} = \dot{m}_{inner} c_p \frac{dT_m}{dz} dz, \tag{4.10}$$

where $\dot{m}_{inner}$ is the mass flow rate of liquid through the aforementioned (finite) inner domain, c_p is the specific heat of the liquid at constant pressure and T_m is the bulk temperature of

the liquid. The characteristic velocity in the inner problem is that at $y = 0$, which equals $\bar{w}_c$ as per Eq. 4.1 and is readily computed from available expressions for b. Hence, $\dot{m}_{inner}$ is of order $\rho \bar{w}_c d^2$. Moreover, because the boundary condition at y = 0 is one of constant heat input, a macroscopic energy balance on a domain that extends across a parallel plate channel. This yields $dT_m/dz = 2q''_{sl}a/(\dot{m}c_p)$, where the factor of 2 implies the channel is symmetrically heated and $\dot{m}$ is the total mass flow rate of liquid through the channel, which may be computed based upon available friction factors which account for hydrodynamic slip. It follows that

$$q_{adv} = \frac{2\rho \bar{w}_c d^2 q''_{sl} a}{\dot{m}} dz. \tag{4.11}$$

The rate of heat conducted into the domain is $q''_{sl} a dz$ such that the criterion for negligible advection out of the domain becomes

$$\frac{2\rho \bar{w}_c d^2}{\dot{m}} \lesssim 0.1 \tag{4.12}$$

Physically, this implies that the mass flow rate of liquid through the inner portion(s) of the domain is small compared to the total mass flow rate.

In dimensionless form, Laplace's equation becomes,

$$\frac{\partial^2 \theta}{\partial \tilde{x}^2} + \frac{\partial^2 \theta}{\partial \tilde{y}^2} = 0, \tag{4.13}$$

where $\theta = \left(T - \bar{T}_{lv}\right) k / \left(q''_{sl} d\right)$. Throughout this paper variables with units of length are non-dimensionalized by half of the pitch of the ridges (d) when a tilde symbol is placed over them. The exception is b_t, which is non-dimensionalized by structure pitch to be consistent

with most of the previous literature. The boundary conditions become

$$\frac{\partial\theta}{\partial\tilde{x}} = 0 \text{ for } \tilde{x} = 0,\ \tilde{y} > 0 \tag{4.14}$$

$$\frac{\partial\theta}{\partial\tilde{x}} = 0 \text{ for } \tilde{x} = 1,\ \tilde{y} > 0 \tag{4.15}$$

$$\frac{\partial\theta}{\partial\tilde{y}} = -1 \text{ for } 0 < \tilde{x} < \phi,\ \tilde{y} = 0 \tag{4.16}$$

$$\frac{\partial\theta}{\partial\tilde{y}} = \tilde{h}\theta \text{ for } \phi < \tilde{x} < 1,\ \tilde{y} = 0 \tag{4.17}$$

$$\frac{d\theta}{d\tilde{y}} = -\phi \text{ for } 0 < \tilde{x} < 1,\ \tilde{y} \to \infty, \tag{4.18}$$

where $\tilde{h} = hd/k$. The symmetry boundary conditions in Eqs. 4.14 and 4.15 always apply, but are only explicitly stated here.

We homogenize the boundary condition given by Eq. 4.16 by defining $\tilde{u}\left(\tilde{x},\tilde{y}\right) = \tilde{\theta}\left(\tilde{x},\tilde{y}\right) + \tilde{y}$. Then, we conformally map the problem to the complex plane according to [15]

$$\tilde{v} = \frac{2}{\pi}\cos^{-1}\left[\frac{\cos\left(\pi\tilde{z}/2\right)}{\cos\left(\pi\phi/2\right)}\right], \tag{4.19}$$

where $\tilde{v} = \tilde{r}\left(\tilde{x},\tilde{y}\right) + i\tilde{s}\left(\tilde{x},\tilde{y}\right)$ and $\tilde{z} = \tilde{x} + i\tilde{y}$. Equation 4.13 is preserved, but the independent variables become $\tilde{r}$ and $\tilde{s}$. The map sends the points (0,∞), (0,0), (ϕ,0), (1,0) and (1,∞) in the real ($\tilde{x}$,$\tilde{y}$) plane to (0,∞), (0,$\tilde{D}$), (0,0), (1,0) and (1,∞), respectively, in the complex ($\tilde{r}$,$\tilde{s}$) plane, where

$$\tilde{D} = \frac{2}{\pi}\ln\left[\frac{\cos\left(\pi\phi/2\right)}{1-\sin\left(\pi\phi/2\right)}\right]. \tag{4.20}$$

Because $\tilde{D}$ is a finite, positive constant, the problem in the complex plane has a homogeneous Neumann boundary condition along $\tilde{r} = 0$ for $\tilde{s} > 0$. Also, the homogeneous Neumann boundary condition along $\tilde{x} = 1$ for $\tilde{y} > 0$ becomes one of the same type along $\tilde{r} = 1$ for $\tilde{s} > 0$. The nonhomogeneous Robin boundary condition along $\tilde{y} = 0$ for $\tilde{a} < \tilde{x} < 1$ is stretched to one of the same type along $\tilde{s} = 0$ for $0 < \tilde{r} < 1$. Finally, the nonhomogeneous Neumann boundary condition as $\tilde{y} \to \infty$ for $0 < \tilde{x} < 1$ corresponds to one of the same type

as $\tilde{s} \to \infty$ for $0 < \tilde{r} < 1$. When $\tilde{u}$ is expressed in terms of ($\tilde{r}$,$\tilde{s}$) rather than ($\tilde{x}$,$\tilde{y}$), we denote it by $U(\tilde{r}, \tilde{s})$.

The effect of the conformal map on the derivatives within the nonhomogeneous boundary conditions may be evaluated from $\partial\tilde{u}/\partial\tilde{y} = \partial\tilde{U}/\partial\tilde{r} \times \partial\tilde{r}/\partial\tilde{y} + \partial\tilde{U}/\partial\tilde{s} \times \partial\tilde{s}/\partial\tilde{y}$. After manipulation it follows that, along $\tilde{s} = 0$ for $0 < \tilde{r} < 1$, $\partial\tilde{U}/\partial\tilde{s} = \partial\tilde{u}/\partial\tilde{y} \times f(\tilde{r})$, where

$$f(\tilde{r}) = \frac{\cos\left(\frac{\pi\phi}{2}\right)\sin\left(\frac{\pi\tilde{r}}{2}\right)}{\left[1 - \cos^2\left(\frac{\pi\phi}{2}\right)\cos^2\left(\frac{\pi\tilde{r}}{2}\right)\right]^{1/2}} \text{ for } 0 < \tilde{r} < 1, \tag{4.21}$$

and, as $\tilde{s} \to \infty$, $\partial\tilde{U}/\partial\tilde{s} = \partial\tilde{u}/\partial\tilde{y}$. Eliminating a mixed boundary condition from the problem is of net benefit, but causes $f(\tilde{r})$ to appear in the Robin boundary condition. Finally, defining $\tilde{w}(\tilde{r}, \tilde{s}) = \tilde{U}(\tilde{r}, \tilde{s}) + (\phi - 1)\tilde{s}$, renders the Neumann boundary condition as $\tilde{s} \to \infty$ homogeneous such that $\nabla^2\tilde{w} = 0$ is subjected to

$$\frac{\partial\tilde{w}}{\partial\tilde{r}} = 0 \text{ for } \tilde{r} = 0,\ \tilde{s} > 0 \tag{4.22}$$

$$\frac{\partial\tilde{w}}{\partial\tilde{r}} = 0 \text{ for } \tilde{r} = 1,\ \tilde{s} > 0. \tag{4.23}$$

$$\frac{\partial\tilde{w}}{\partial\tilde{s}} + 1 - \phi = \tilde{h}\left(\tilde{w} + \frac{1}{\tilde{h}}\right) f(\tilde{r}) \quad \text{for } 0 < \tilde{r} < 1,\ \tilde{s} = 0 \tag{4.24}$$

$$\frac{\partial\tilde{w}}{\partial\tilde{s}} = 0 \text{ for } 0 < \tilde{r} < 1,\ \tilde{s} \to \infty \tag{4.25}$$

Solving Eq. 4.13 by the method of separation of variables and applying the three homogeneous boundary conditions yields

$$\tilde{w} = \sum_{j=0}^{\infty} d_j \cos(j\pi\tilde{r})\, e^{-j\pi\tilde{s}} \tag{4.26}$$

Inserting this result into the nonhomogeneous boundary condition, Eq. 4.24, multiplying by the j$^{\text{th}}$ eigenfunction and integrating across the homogeneous direction, does not yield an expression for d_j. However, by expressing the left- and right-hand sides of Eq. 4.24 by

Fourier series, we can utilize orthogonality to numerically compute d_j.

The function $f(\tilde{r})$ is odd and has a dimensionless period of 4. However, since only its value for $0 < \tilde{r} < 1$ is relevant, we choose to express it in a Fourier cosine series as

$$f(\tilde{r}) = \sum_{k=0}^{\infty} e_k \cos(k\pi\tilde{r}), \tag{4.27}$$

where standard orthogonality relations yield,

$$e_0 = \int_0^1 \frac{\cos\left(\frac{\pi\phi}{2}\right)\sin\left(\frac{\pi\tilde{r}}{2}\right)}{\left[1-\cos^2\left(\frac{\pi\phi}{2}\right)\cos^2\left(\frac{\pi\tilde{r}}{2}\right)\right]^{1/2}} d\tilde{r} \tag{4.28}$$

$$e_k = 2\int_0^1 \frac{\cos\left(\frac{\pi\phi}{2}\right)\sin\left(\frac{\pi\tilde{r}}{2}\right)}{\left[1-\cos^2\left(\frac{\pi\phi}{2}\right)\cos^2\left(\frac{\pi\tilde{r}}{2}\right)\right]^{1/2}} \cos(k\pi\tilde{r})\, d\tilde{r} \tag{4.29}$$

for $k > 0$.

Analytical results for the preceding integrals are cumbersome. Hence, we compute them numerically.

Utilizing the expression for $\tilde{w}$ (Eq. 4.26), the left-hand side of the nonhomogeneous boundary condition (Eq. 4.24) may be expressed as

$$\left.\frac{\partial\tilde{w}}{\partial\tilde{s}}\right|_{\tilde{s}=0} + 1 - \phi = \sum_{l=0}^{\infty} f_l \cos(l\pi\tilde{r}), \tag{4.30}$$

where

$$f_0 = 1 - \phi \tag{4.31}$$

$$f_l = -l\pi d_l \text{ for } l > 0. \tag{4.32}$$

Moreover, excluding the scaling factor, the right-hand side of this boundary condition may be expressed as

$$\tilde{h}\left[\tilde{w}(\tilde{r},0) + \frac{1}{\tilde{h}}\right] = \sum_{m=0}^{\infty} g_m \cos(m\pi\tilde{r}), \tag{4.33}$$

where

$$g_0 = \tilde{h}\left(d_0 + \frac{1}{\tilde{h}}\right) \tag{4.34}$$

$$g_m = d_m \tilde{h} \text{ for } m > 0. \tag{4.35}$$

The product of this Fourier series and that representing the scaling factor (Eq. 4.21) equals the Fourier-series representation of the left-hand side of the nonhomogeneous boundary condition as per

$$\sum_{l=0}^{\infty} f_l \cos\left(l\pi\tilde{r}\right) = \sum_{m=0}^{\infty} g_m \cos\left(m\pi\tilde{r}\right) \sum_{k=0}^{\infty} e_k \cos\left(k\pi\tilde{r}\right). \tag{4.36}$$

Multiplying this expression by $\cos\left(p\pi\tilde{r}\right)$, where p is an integer between 0 and ∞, and integrating across the homogeneous direction yields

$$\sum_{l=0}^{\infty} f_l \int_0^1 \cos\left(l\pi\tilde{r}\right)\cos\left(p\pi\tilde{r}\right) d\tilde{r} = \sum_{m=0}^{\infty}\sum_{k=0}^{\infty} g_m e_k \cdot \int_0^1 \cos\left(m\pi\tilde{r}\right)\cos\left(k\pi\tilde{r}\right)\cos\left(p\pi\tilde{r}\right) d\tilde{r}. \tag{4.37}$$

Performing the integration yields a linear system of equations valid between $p = 0$ and $p = \infty$ as per

$$\sum_{l=0}^{\infty} f_l t\left(l,p\right) = \sum_{m=0}^{\infty}\sum_{k=0}^{\infty} g_m e_k \left[a\left(m,k,p\right) + b\left(m,k,p\right) + c\left(m,k,p\right) + d\left(m,k,p\right)\right], \tag{4.38}$$

where

$$t\left(l,p\right) = \begin{cases} 1 & \text{if } l = p = 0 \\ 1/2 & \text{if } l = p > 0 \\ 0 & \text{otherwise} \end{cases} \tag{4.39}$$

$$a\left(m,k,p\right)=\begin{cases}1/4 & \text{if } m=k=p=0\\ 0 & \text{otherwise}\end{cases} \tag{4.40}$$

$$b\left(m,k,p\right)=\begin{cases}1/4 & \text{if } k-m=p\\ 0 & \text{otherwise}\end{cases} \tag{4.41}$$

$$c\left(m,k,p\right)=\begin{cases}1/4 & \text{if } m+k=p\\ 0 & \text{otherwise}\end{cases} \tag{4.42}$$

$$d\left(m,k,p\right)=\begin{cases}1/4 & \text{if } m-k=p\\ 0 & \text{otherwise.}\end{cases} \tag{4.43}$$

Upon removal of the terms equal to zero in the sum and double sum in Eq. 4.38, it becomes

$$f_0=e_0g_0+\frac{1}{2}\sum_{m=1}^{\infty}e_mg_m\ \ (p=0) \tag{4.44}$$

$$2f_p=\sum_{m=0}^{p}e_{p-m}g_m+\sum_{m=0}^{\infty}e_mg_{m+p}+e_{m+p}g_m\ \ (p\geq 1)\,. \tag{4.45}$$

The unknown column vector in the linear system, d_j, appears in f_l (for $l\geq 1$) and g_m (for all m). We impose $P+1$ unknowns (d_0 through d_P) on a truncated form of the linear system with $P+1$ equations (those for $p=0$ through $p=P$) by truncating the sums therein

according to

$$f_0 = g_0 e_0 + \frac{1}{2}\sum_{m=1}^{P} e_m g_m \;\; (p=0) \tag{4.46}$$

$$2f_p = \sum_{m=0}^{p} e_{p-m} g_m + \sum_{m=0}^{P-p} e_m g_{m+p} + \sum_{m=0}^{P} e_{m+p} g_m \quad (p \geq 1)\,. \tag{4.47}$$

The linear systems were solved using the built-in LU factorization from MATLAB to find the coefficents, d_j, although we note that an indirect method, using a few steps of Gauss-Seidel iteration gave effectively the same results. Evaluation of the thermal slip length requires an expression for $\theta(\tilde{x}, 0)$ along $\tilde{y} = 0$. Upon transforming from $\tilde{w}$ back to θ, it follows that

$$\theta(\tilde{x}, 0) = \sum_{j=0}^{P} d_j \cos\left[j\pi \tilde{r}(\tilde{x}, 0)\right] e^{-j\pi \tilde{s}(\tilde{x},0)} + (1-\phi)\,\tilde{s}(\tilde{x}, 0)\,, \tag{4.48}$$

where it follows from Eq. 4.19 and the requirement that $\tilde{s}(\tilde{x}, 0) \geq 0$ that for $0 \leq \tilde{x} \leq 1$

$$\tilde{r}(\tilde{x}, 0) = \frac{2}{\pi}\cos^{-1}\left[\frac{\cos\left(\frac{\pi}{2}\tilde{x}\right)}{\cos\left(\frac{\pi}{2}\phi\right)}\right] H(\tilde{x} - \phi) \tag{4.49}$$

$$\tilde{s}(\tilde{x}, 0) = -\frac{2}{\pi}\ln\left[\frac{\cos\left(\frac{\pi}{2}\tilde{x}\right)}{\cos\left(\frac{\pi}{2}\phi\right)} - \left|\sqrt{\frac{\cos^2\left(\frac{\pi}{2}\tilde{x}\right)}{\cos^2\left(\frac{\pi}{2}\phi\right)} - 1}\right|\right] H(\phi - \tilde{x})\,, \tag{4.50}$$

where H is the Heaviside step function, which equals 0 and 1 when its argument is < 0 and ≥ 0, respectively. Noting that

$$\phi = -\left.\frac{\partial \bar{\theta}}{\partial \tilde{y}}\right|_c, \tag{4.51}$$

the definition of thermal slip length implies that

$$\tilde{b}_t = \frac{1-\phi}{2\phi^2}\int_0^{\phi} \theta(\tilde{x}, 0)\, d\tilde{x} - \frac{1}{2\phi}\int_{\phi}^{1} \theta(\tilde{x}, 0)\, d\tilde{x}. \tag{4.52}$$

We compute $\tilde{b}_t$ for prescribed values of ϕ and $\tilde{h}$ by setting $P = 200$ and increasing it by 200 until no change is observed in the result to six digits.

4.2.3 Isothermal Meniscus

The boundary conditions for an isoflux solid-liquid interface and isothermal meniscus are those given by Eqs. 4.14-4.18, except that Eq. 4.7 is replaced by $\theta = 0$ for $\phi < \tilde{x} < 1$ and $\tilde{y} = 0$. The solution is the superposition of those to a one-dimensional background problem and a two-dimensional perturbation problem. The former is governed by $d^2\theta_{1D}/d\tilde{y}^2 = 0$ subjected to $\theta_{1D} = 0$ at $\tilde{y} = 0$ and $d\theta_{1D}/d\tilde{y} = -\phi$ as $\tilde{y} \to \infty$ such that $\theta_{1D} = -\phi\tilde{y}$. The latter is governed by $\nabla^2\theta_p = 0$ subjected to the symmetry boundary conditions and

$$\frac{\partial\theta_p}{\partial\tilde{y}} = \phi - 1 \text{ for } 0 < \tilde{x} < \tilde{a},\ \tilde{y} = 0 \tag{4.53}$$

$$\theta_p = 0 \text{ for } \tilde{a} < \tilde{x} < 1,\ \tilde{y} = 0 \tag{4.54}$$

$$\frac{d\theta_p}{d\tilde{y}} = 0,\ \text{for } 0 < \tilde{x} < 1,\ \tilde{y} \to \infty. \tag{4.55}$$

We note that $\bar{\theta}_{sl} - \theta_{\tilde{y}\to\infty} = (\theta_{1D,\tilde{y}=0} - \theta_{1D,\tilde{y}\to\infty}) + \left(\bar{\theta}_{p,sl} - \theta_{p,\tilde{y}\to\infty}\right)$ and that $\theta_{1D,\tilde{y}=0} - \theta_{1D,\tilde{y}\to\infty} = \bar{\theta}_c - \theta_{\tilde{y}\to\infty}$. Then, it follows from Eq. 4.2 that the thermal slip length is

$$\tilde{b}_t = \frac{\bar{\theta}_{p,sl} - \theta_{p,\tilde{y}\to\infty}}{2\left(\partial\theta/\partial\tilde{y}\right)\big|_c}. \tag{4.56}$$

Philip [15] solved a mathematically equivalent perturbation problem in the context of shear flow over a plate with a regular array of shear-free slots parallel to the flow direction. Utilizing his results in Eq. 4.56, the thermal slip length becomes

$$\tilde{b}_t = \frac{(1-\phi)}{\pi\phi}\left\{\frac{1}{\phi}\int_0^{\phi}\cosh^{-1}\left[\sec\left(\frac{\pi\phi}{2}\right)\cos\left(\frac{\pi\tilde{x}}{2}\right)\right]d\tilde{x} - \ln\left[\sec\left(\frac{\pi\phi}{2}\right)\right]\right\}. \tag{4.57}$$

4.3 Model Validation

To validate the analytical results, STAR-CCM+Ⓡ version 7.04 (double precision) was used to solve the problem for an adiabatic meniscus, an isothermal meniscus, and three finite non-dimensional heat transfer coefficient values at the meniscus $\tilde{h} = 1, 100$, and 1000, all at solid fractions of 0.01 and 0.1. The height of the computational domain was set to 25 times the structure pitch to well approximate a semi-infinite domain. A finite volume approach with an algebraic multigrid iterative solver was employed. The meshes utilized featured increasing levels of refinement near the solid-liquid interface where steep temperature gradients were present. Meshes were generated for both solid fractions and were subsequently refined until the thermal slip length for the isothermal meniscus case was within 1% of the analytical value given by Eq. 4.57. To further verify the validity of the meshes, the meniscus was also subjected to the adiabatic condition and the resulting thermal slip lengths agreed with the analytical predictions to within 0.04%. The meshes used for $\phi = 0.1$ and 0.01 contained nominally 200k and 370k cells, respectively. Further refinement to the smaller solid fraction mesh for the adiabatic meniscus case yielded a change in thermal slip length of less than 0.02%. The solutions were deemed converged when the discretized Laplace equation residuals asymptoted to nominally 10^{-13} and, within numerical precision, the thermal slip length ceased to change.

4.4 Results

The semi-analytically computed thermal slip length is plotted versus solid fraction for an adiabatic meniscus, selected finite values of dimensionless heat transfer coefficient and an isothermal meniscus in Fig. 4.3. The corresponding numerical results for the aforementioned discrete values of ϕ and $\tilde{h}$ are shown by the solid triangles. The mean of the absolute value of the discrepancy between the analytical and numerical results is 1.61% .

As discussed by Carey [37], Schrage [38] derived an expression for the interfacial heat

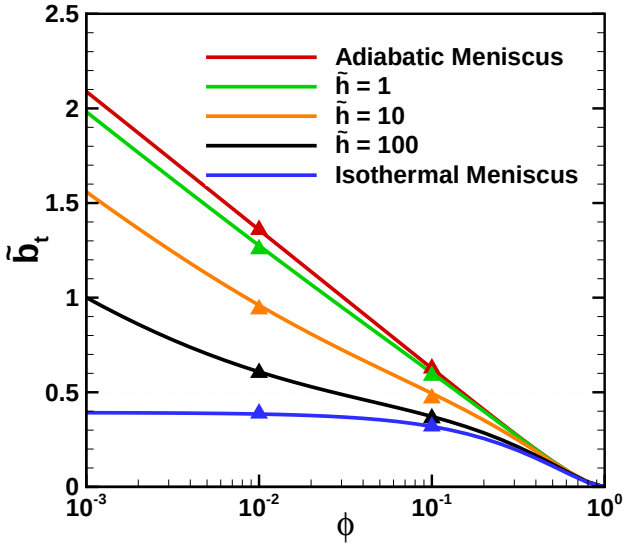

Figure 4.3: Dimensionless thermal slip length versus solid fraction for adiabatic meniscus, finite dimensionless heat transfer coefficient at meniscus and isothermal meniscus when the boundary condition at the solid-liquid interface is constant heat flux. Triangles correspond to numerical validation of semi-analytical results.

transfer coefficient as per

$$h = \frac{2\hat{\sigma}}{2-\hat{\sigma}} \frac{h_{lv}^2}{\bar{T}_{lv} v_{lv}} \left(\frac{M}{2\pi R \bar{T}_{lv}} \right)^{1/2} \left(1 - \frac{p_v v_{lv}}{2h_{lv}} \right), \tag{4.58}$$

where properties are evaluated at $\bar{T}_{lv}$ and $\hat{\sigma}$ is the accommodation coefficient, h_{lv} is the latent heat of evaporation, v_{lv} is the difference between saturated vapor and saturated liquid specific volumes, M is the molecular weight of the liquid, R is the universal gas constant and p_v is saturation pressure. Eq. 4.58 is valid when

$$\frac{q''_{lv}}{\rho_v h_{lv}} \left(\frac{2R\bar{T}_{lv}}{M} \right)^{1/2} \leq 0.01, \tag{4.59}$$

where ρ_v is the vapor density. When the right-hand side of this equation equals 0.01, the corresponding interfacial heat flux is denoted by $q''_{lv,max}$. Eq. 4.58 imposes a linear relationship between the (local) heat flow and the (local) temperature difference between the phases. This implies that conditions are sufficiently close to equilibrium such that the Boltzmann

distribution describes the velocity distribution of vapor molecules leaving and approaching the meniscus. In the case of water, assuming an accommodation coefficient of unity, the extremely-high interfacial heat transfer coefficient and corresponding $q''_{lv,max}$ are plotted versus temperature in Fig. 4.4 based upon the properties of water in Reference [81]. When Eq. 4.59 is invalid, Schrage [38] provides a more cumbersome relation to compute the interfacial heat transfer coefficient.

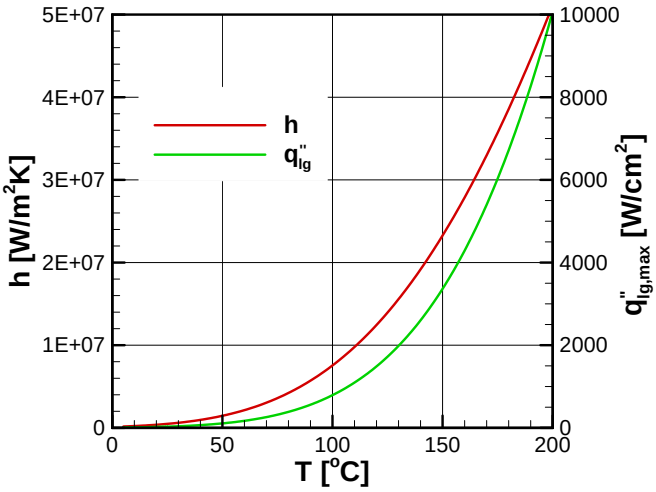

Figure 4.4: Interfacial heat transfer coefficient and maximum interfacial heat flux to which it applies as a function of temperature for water.

Thermal slip length is computed by prescribing ϕ and $\bar{T}_{lv}$, using Fig. 4.4 to determine the corresponding value of $\tilde{h}$ and finding $\tilde{b}_t$ from Fig. 4.3. For example, for $\phi = 0.01$ and $\bar{T}_{lv} = 100^o$C, in the case of water, $h = 7.55\times10^6$ W/(m^2·K) and $q''_{lv,max} = 792$ W/cm^2. Assuming a ridge pitch of 2 μm ($d = 1$ μm), $\tilde{h} = 11.12$, and $\tilde{b}_t = 0.94$, which is a 30% reduction relative to the case of an adiabatic meniscus and 2.44 times the limiting value for an isothermal meniscus. Macroscopically, the Nusselt number is a function of the thermal slip length [29] and its value computed from the analysis herein rather than that for an adiabatic meniscus should be utilized.

4.5 Conclusions

We developed expressions for the dimensionless (apparent) thermal slip length for liquid flow in the Cassie state over ridge-type structured surfaces in the presence of local evaporation and condensation along the meniscus subject to the constraint that the net rate of phase change is zero. An isoflux boundary condition was imposed at the solid-liquid interface. In the limiting case of an isothermal meniscus, analytical results provide thermal slip length as a function of solid fraction. In the case of a finite heat transfer coefficient along the meniscus, semi-analytical results provide thermal slip length as a function of solid fraction and dimensionless interfacial heat transfer coefficient. Evaporation and condensation substantially reduce thermal slip lengths at conditions relevant to water-based thermal management of electronics. The reduction in thermal resistance of a microchannel heat sink may be quantified by using apparent thermal slip lengths computed from the present analysis in relevant Nusselt number expressions. Future work should consider the effect of evaporation and condensation on the hydrodynamic slip length as they induce a non-zero velocity normal to the meniscus. More rigorous expressions for both slip lengths in diabatic flows must simultaneously account for the effects of curvature, thermocapillary stress and evaporation and condensation along the meniscus and, as per the study by Ng and Wang [36], relax the assumption that heat is supplied to the fluids exclusively at the solid-liquid interface.

4.6 Acknowledgements

The authors gratefully acknowledge Durwood Marshall and Shawn Doughty of Tufts Technology Services for their assistance and access to Tufts UIT Research Computing facilities. We acknowledge Bruce Bogosian for a useful discussion on the solution of Laplace?s equation subjected to mixed boundary conditions. Bell Labs Ireland thanks the Industrial Development Agency (IDA) Ireland for their financial support. Funding for this research was provided in part by the NSF CBET award no. 1402783.

Chapter V

Effect of Meniscus Curvature on Apparent Thermal Slip

Abstract

We analytically consider the effect of meniscus curvature on heat transfer to laminar flow across structured surfaces. The surfaces considered are composed of ridges oriented parallel to the flow. The curved meniscus separating liquid in the Cassie state and gas trapped in cavities between the ridges, results from the pressure difference between the liquid and the gas. Perturbation theory is used to develop expressions that account for the change in the temperature field that occurs in the limit of small deflections to the meniscus. The meniscus is considered adiabatic. A constant heat flux boundary condition is prescribed at the tips of the ridges. We provide approximate expressions for the apparent thermal slip length as function of solid-fraction over a range of small meniscus protrusion angles. Numerical results show good agreement with perturbation results for protrusion angles less than +/- 20 degrees.

5.1 Introduction

Micro and nano-structured surfaces, SSs, are engineered to reduce drag by using a combination of roughness and hydrophobic coatings. They are being considered for microchannel

flows where surface friction forces dominate in such applications as electronics cooling and lab-on-a-chip technologies. Liquid in the Cassie (unwetted) state on a micro- or nano-structured surface forms a meniscus along the liquid-gas interface as shown in Fig. 5.1. Meniscus curvature is often considered a secondary effect and neglected in analysis of flow and heat transfer along these surfaces. Recent work has shown that the effect of curvature on hydrodynamic slip length is not necessarily small and depends on the geometry of the structures, the solid-fraction and magnitude of protrusion angle. We use a perturbation approach to assess the change to apparent thermal slip across parallel ridges due to the presence of meniscus curvature.

In the presence of a pressure gradient along the channel, the radius of curvature of the meniscus increases in the streamwise direction. The angle made by the meniscus at any point follows from the Young-Laplace equation. The maximum protrusion downward into the gas phase is limited by the maximum advancing contact angle of the solid-liquid-gas system. Above this angle the liquid will begin to advance down the sides of the structures compromising the Cassie state. Conversely, if the pressure in the gas phase is greater than that of the liquid, the meniscus will extend upward into the liquid. This is limited by the receding contact angle of the solid-liquid-gas system, above which the meniscus will depin from the structures.

When the liquid is thermodynamically stable in the so-called Cassie state, it encounters a mixed-boundary condition at the surface. The classic no-slip boundary condition exits at the liquid-solid interface where the primary heat transfer occurs. At the liquid-vapor interface, i.e., the meniscus, the flow boundary condition is low to no shear, and the thermal boundary condition is low heat transfer to adiabatic.

When considering channel flow, the hydrodynamic and thermal boundary conditions on these surfaces are treated similarly to the boundary conditions in the slip regime of rarefied gas flows using Navier's [7] and Poison's[1] slip conditions, respectively. For velocity, the

[1]According to Kennard [8]

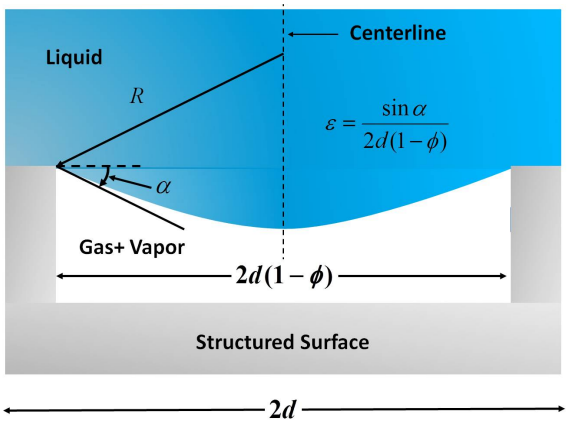

Figure 5.1: Schematic of a curved meniscus between the ridges. The protrusion angle, α is made between the line tangent to the meniscus at the corner of the ridge and the horizontal. The pitch of the strucures is $2d$.

boundary condition is

$$\bar{u}|_c = b \left. \frac{du}{dn} \right|_c \tag{5.1}$$

where $\bar{u}|_c$ is the *apparent* velocity at the composite interface, b is the the *apparent* hydrodynamic slip length, henceforth referred to as slip length, and n is the direction normal to the composite interface pointing into the liquid flow. The thermal boundary condition is

$$\bar{T}_{sl} - \bar{T}_c = -b_t \left. \frac{\partial \bar{T}}{\partial n} \right|_c \tag{5.2}$$

where b_t is the *apparent* thermal slip length, henceforth referred to as thermal slip length. Slip and thermal slip length expressions are available from [17, 29, 97]

In the presence of meniscus curvature, finding an average for apparent velocity and temperature across the interface becomes problematic. Instead, the slip velocity that is added to the flow is equivalent to $\bar{u}|_c$ and the slip length can be found from it subsequent to solving the channel level flow [16, 17, 98].

For the thermal case, the left hand side of Eq. 5.2 is the temperature jump which results from the added thermal resistance at the composite boundary. The inner problem is solved to find the change to the thermal resistance between the solid-liquid interface and the outer

flow that results from the presence of a curved meniscus. Near the tips of the structures, the flow and heat transfer are governed by Re_c and Pe_c, where c is the length scale of the structures. The flow is considered Stokes flow and heat transfer is considered purely diffusive. When the channel height is large compared with the length scale of the structures, the temperature field becomes uniform at a vertical distance that is on the order of the pitch of the structures. This is compared to that of the one dimensional case, T_{1D}, where there is no meniscus in a domain with the same width and the same heat rate. The thermal resistance can then be found from the difference between the two cases, i.e. the change in thermal resistance due to the meniscus. This approach was used by, e.g., Mikic and Rohsenow [99] and Smythe [90] in the context of thermal contact resistance and electrical resistance, respectively. Taking T_p as the change to the temperature field which results from the presence of the meniscus, i.e., $T_{1D}+T_p = T$ and requiring that the heat rate in the T and T_{1D} domains be the same. The temperature jump can be expressed as $\bar{T}_{p,sl} - T_{p,\infty}$. Noting that $\bar{T}_{sl} - T_\infty = \left(\bar{T}_{p,sl} - T_{p,\infty}\right) + (T_{1D,sl} - T_{1D,\infty})$. The thermal boundary condition for the outer problem can be rewritten

$$\bar{T}_{p,sl} - \bar{T}_{p,\infty} = -b_t \left.\frac{\partial \bar{T}}{\partial y}\right|_{y=0}. \tag{5.3}$$

The slip length captures not only the spreading resistance but also the change to the one dimensional resistance that results from the presence of the irregular boundary.

5.2 Previous work

The effect of hydrodynamic slip on drag reduction across structured surfaces is well documented in the literature [13, 25, 26, 65]. Heat transfer to such flows has only recently received attention [29, 33, 100, 101].

A number of studies have shown that the shape of the meniscus and the degree of protrusion significantly affect drag. Ybert et al. [23] developed scaling laws for hydrodynamic

slip. They derive expressions for secondary effects such as a finite shear force at the meniscus and pressure-induced curvature of the meniscus. They assumed a meniscus with a positive protrusion angle, i.e., positive pressure in the gas. In the limit of large solid fraction, the correction to slip length is negatively proportional to the cavity fraction and the height of the meniscus. In the limit of small solid fraction, the correction to slip length varies inversely with curvature such that for high curvature the slip length is negatively impacted. Bocquet and Barrat [42] discuss the analogy between thermal slip and hydrodynamic slip. We note that these scaling laws are also applicable to thermal slip in the presence of curvature.

Sbragaglia and Prosperetti [43] used perturbation theory to study the effect of small deflections in the meniscus as a function of shear free fraction for parallel ridges. They identify two significant effects that result. The first is the effect on the change in the cross-sectional area of the flow due to the deformation at the liquid-gas interface, and the second is the change in the velocity field. They provide hydrodynamic slip length expressions for parallel ridges for a pressure driven flow with a finite channel height and for shear flow with an infinite channel height. They use a small parameter ε in their expressions but they do not account for the fact the ε changes with shear-free fraction.

Steinberger et al. [28] studied menisci formed on a surface composed of a square lattice of cylindrical holes. They used a dynamic surface force apparatus to measure viscous damping forces which they correlated to slip lengths. They experimentally studied two cases, liquid in the Cassie and Wenzel states. When the liquid was in the Cassie state, gas bubbles were trapped in the holes with menisci protruding upward in the shape of spherical caps. In the Wenzel state, the surface and cavities were fully wetted. They found a lower effective slip length in the presence of microbubbles than in the wetted state. Notably, roughness caused by the presence of these bubbles increased friction at the surface. They also performed numerical simulations of a Couette flow over menisci with the same geometry at various contact angles. They found that the shape and protrusion angle of the meniscus significantly affected slip length. For negative protrusion angles slip length increased with protrusion

angle. The maximum value of slip length was reached at angle of zero. For positive protrusion angles, slip length was degraded as protrusion angle increased and became negative above a critical value.

Hyvaluoma and Harting [44] used a mesoscopic lattice Boltzmann simulation to study Couette flow over structured surfaces with attached gas bubbles. They accounted for deformation of the bubbles due to viscous forces. They found slip length had a shear rate dependence. Increasing the shear rate decreased the height of the bubbles. They report slip length as a function of protrusion angle of the bubbles and found the same qualitative relationship between protrusion angle and slip length in agreement with Steinberger et al. [28].

Two analytical studies have addressed the effect of meniscus curvature in the limit of low shear-free fraction. Crowdy [45] used a series of conformal maps to model a meniscus between parallel ridges. He derived an expression for slip length as a function of solid fraction and protrusion angle which is applicable for a periodic distribution of ridges in the limit of large solid fractions. Davis and Lauga [46] used a two-dimensional model of shear flow past an array of bubbles trapped between transverse ridges and provide an expression to calculate the critical protrusion angle. Their results also show the asymmetry between the effects of negative and positive protrusion angles.

Teo and Khoo performed numerical studies of the effect of meniscus curvature on drag for menisci formed between parallel ridges for both Poiseuille and Couette flows [27] and in Poiseuille flow between transverse ridges [47]. For transverse ridges, they report a critical protrusion angle $\theta_c \approx 62 - 65^\circ$ at which the slip length becomes zero that is independent of shear-free fraction, geometry and flow type but which decreases as channel height is reduced for a given shear-free fraction. Above θ_c friction was enhanced. For parallel ridges, slip length displayed asymmetry with respect to positive and negative protrusion angles; however, there was no critical angle at which drag reduction became zero. Instead the slip length exhibited a monotonic increase with protrusion angle even for large angle values

up to 90°. They also found that the ratio of parallel ridge slip length to transverse ridge slip length did not remain constant as protrusion angle was varied. Notably, their results showed a more positive benefit in drag reduction for menisci between parallel ridges than for transverse ridges holding shear-free fraction, protrusion angle and normalized rib spacing constant. Teo and Khoo [47] correlated their results with those of Davis and Lauga [46], Crowdy [45] and Ng and Wang [48] showing good agreement between the numerical results and the analytical models. To the authors' knowledge the effect of meniscus curvature on thermal slip has not been studied. This motivates the present work.

5.3 Problem Formulation

The geometry under consideration is that of a concave or convex meniscus formed between two ridges of a structured surface with solid-fraction, ϕ. The center-to-center spacing of the ridges is $2d$, the width of the ridge is $2a$, the width of the cavity is $2c$, and $(d-c)/d = \phi$. The flow in the outer problem is assumed hydrodynamically and thermally fully developed and thermophysical properties are assumed constant. We address the inner problem where the Reynolds and Peclet numbers, Re_a and Pe_a, based on the ridge width, a, are very small. The hydrodynamic condition is considered to be Stokes flow, and heat transfer is considered to be purely diffusive. Secondary effects such as evaporation and condensation across the meniscus [97] and thermocapillary stress are not considered here.

We consider a unit cell of width, d and infinite height. Symmetry boundary conditions exist at the midpoint of the meniscus and the midpoint of the ridge such that

$$\frac{\partial T}{\partial x} = 0 \quad \text{for} \quad x = 0, d \quad \text{and} \quad y > 0. \tag{5.4}$$

We consider a constant heat flux boundary condition at the solid-liquid interface

$$\frac{\partial T}{\partial y} = -\frac{q''_{sl}}{k} \quad \text{for} \quad c < x < d, \quad y = 0. \tag{5.5}$$

Constant heat flux leaves the domain as $y \to \infty$.

$$\frac{\partial T}{\partial y} = -\frac{q''_\infty}{k} \quad \text{for} \quad 0 < x < d, \quad y \to \infty. \tag{5.6}$$

The adiabatic condition along the meniscus is

$$\hat{n} \cdot \nabla T = 0 \tag{5.7}$$

where $\hat{n}$ is the vector normal to the meniscus. The problem is rendered dimensionless by using $\tilde{T} = Tk/(q''_{sl}d), \tilde{x} = x/d$ and $\tilde{y} = y/d$. The analytical domain is shown in Fig. 5.2.

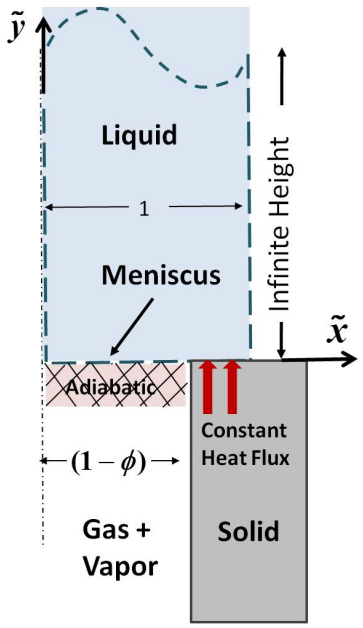

Figure 5.2: Schematic of a single unit cell of a parallel ridge structured surface with meniscus between the ridges. Dimensions are normalized with respect to half the pitch of the structures.

5.3.1 Perturbation Approach

In the limit of a small protrusion angle, as would potentially be the case with water, the deflection of the meniscus is taken to be small and we follow the approach of Sbragaglia and

Prosperetti [43] defining the meniscus shape as

$$\tilde{y} + \tilde{\varepsilon}\tilde{\eta}(\tilde{x}) = 0 \tag{5.8}$$

where $\tilde{\eta}$ and $\tilde{\varepsilon}$ are dimensionless quantities and $\varepsilon \ll 1$. Expressing the temperature field as a Taylor series in $\tilde{\varepsilon}$ it takes the form

$$\tilde{T}(\tilde{x}, \tilde{y}) = \tilde{T}_0 + \tilde{\varepsilon}\tilde{T}_1 + o(\tilde{\varepsilon}) \tag{5.9}$$

where $\tilde{T}_0$ is the temperature profile assuming a flat adiabatic meniscus between the structures, and $\tilde{T}_1$ is the addition to temperature that would result from the deflection of the meniscus.

5.3.1.1 Boundary Condition at Meniscus

Taking the normal vector as $\hat{n} = \tilde{\varepsilon} d\tilde{\eta}/d\tilde{x}\hat{i} + \hat{j}$, the adiabatic condition along the meniscus is

$$\tilde{\varepsilon}\frac{d\tilde{\eta}}{d\tilde{x}}\frac{\partial \tilde{T}}{\partial \tilde{x}} + \frac{\partial \tilde{T}}{\partial \tilde{y}} = 0 \quad \text{for} \quad 0 < |\tilde{x}| < 1 - \phi. \tag{5.10}$$

Substituting Eq. 5.9 into the above

$$\tilde{\varepsilon}\frac{d\tilde{\eta}}{d\tilde{x}}\left(\frac{\partial \tilde{T}_0}{\partial \tilde{x}} + \tilde{\varepsilon}\frac{\partial \tilde{T}_1}{\partial \tilde{x}}\right) + \frac{\partial \tilde{T}_0}{\partial \tilde{y}} + \tilde{\varepsilon}\frac{\partial \tilde{T}_1}{\partial \tilde{y}} = 0 \quad \text{for} \quad 0 < |\tilde{x}| < 1 - \phi \tag{5.11}$$

Matching terms the boundary condition along the meniscus for $\tilde{T}_0$ becomes,

$$\left.\frac{\partial \tilde{T}_0}{\partial \tilde{y}}\right|_{\tilde{y}=0} = 0, \tag{5.12}$$

and for $\tilde{T}_1$

$$\left.\frac{\partial \tilde{T}_1}{\partial \tilde{y}}\right|_{\tilde{y}=0} = -\left.\frac{d\tilde{\eta}}{d\tilde{x}}\frac{\partial \tilde{T}_0}{\partial \tilde{x}}\right|_{\tilde{y}=0}. \tag{5.13}$$

We approximate the shape of the meniscus by considering an arc of radius, R, which

results from a pressure difference across the meniscus, Δp_{lg} between the pressure in the liquid above the composite interface and the pressure of the gas in the cavities. It is governed by the Laplace-Young equation

$$\Delta p_{\mathrm{lg}} = \frac{\sigma_{\mathrm{lg}}}{R} \tag{5.14}$$

where σ_{lg} is the liquid-gas surface tension. This arc would extend upward if the pressure in the gas exceeded the pressure in the liquid. We note that, for a pressure-driven flow, there would be a pressure gradient in the channel causing R to change in the streamwise direction. A circular arc pinned at the corners of the ridges and extending downward is of the form

$$x^2 + \left(y - \left|\sqrt{R^2 - c^2}\right|\right)^2 = R^2 \tag{5.15}$$

or

$$y = \left(\left|\sqrt{R^2 - c^2}\right| - \left|\sqrt{R^2 - x^2}\right|\right). \tag{5.16}$$

Rewriting and using binomial series approximations

$$y \simeq R\left[1 - \frac{1}{2}\left(\frac{c}{R}\right)^2\right] - R\left[1 - \frac{1}{2}\left(\frac{x}{R}\right)^2\right], \tag{5.17}$$

results in

$$y \simeq \frac{1}{2R}\left(c^2 - x^2\right). \tag{5.18}$$

Expressing Eq. 5.14 in terms of ε

$$\varepsilon \simeq \frac{1}{2R} \simeq \frac{\Delta p_{\mathrm{lg}}}{2\sigma_{\mathrm{lg}}} \tag{5.19}$$

where $\varepsilon = \tilde{\varepsilon}/d$. Using the relation in Eq. 5.8 in dimensionless terms

$$\tilde{y} = -\tilde{\varepsilon}\tilde{\eta}\left(x\right) \simeq -\tilde{\varepsilon}\left(\left(1 - \phi\right)^2 - \left(\tilde{x}\right)^2\right). \tag{5.20}$$

It follows that

$$\tilde{\varepsilon} \simeq \frac{\Delta p_{\mathrm{lg}} d}{2\sigma_{\mathrm{lg}}}, \tag{5.21}$$

and the shape of the meniscus is

$$\tilde{\eta}\left(\tilde{x}\right) \simeq \left[(1-\phi)^2 - \left(\tilde{x}\right)^2\right]. \tag{5.22}$$

From geometry, Eq. 5.21 can be stated in terms of solid-fraction and meniscus protrusion angle, α.

$$\tilde{\varepsilon} \simeq -\frac{\sin\alpha}{2(1-\phi)} \tag{5.23}$$

The protrusion angle is measured from the horizontal to the line tangent to the meniscus at the triple contact line at the corner of the ridge. A positive protrusion angle corresponds to the meniscus projecting upward into the liquid, and a negative protrusion angle corresponds to the meniscus extending downward into the cavity.

For water in the Cassie state with maximum contact angle of $\theta_A = 110^\circ$ on a surface with solid fraction, $\phi = .01$, $\tilde{\varepsilon} = -0.17$.

5.3.2 Isoflux Ridge, Flat Meniscus

In this section we solve the temperature profile in the presence of a flat meniscus, $\tilde{T}_0$. Assuming constant heat flux q''_{sl} at the ridge and symmetry boundary conditions at $x = 0$ and $x = d$, the temperature profile takes the following form.

$$\tilde{T}_0[\tilde{x}, \tilde{y}] = -\phi\tilde{y} + \tilde{u}[\tilde{x}, \tilde{y}]. \tag{5.24}$$

The first term on the RHS is the temperature profile in the absence of a meniscus and $\tilde{u}$ is the change to the temperature field that results from the presence of an adiabatic, flat

meniscus. The two-dimensional temperature field is governed by Laplaces equation,

$$\nabla^2 \tilde{T}_0 = 0 \tag{5.25}$$

subjected to

$$\frac{\partial \tilde{T}_0}{\partial \tilde{y}} = 0 \qquad 0 < \tilde{x} < 1 - \phi, \quad \tilde{y} = 0 \tag{5.26}$$

$$\frac{\partial \tilde{T}_0}{\partial \tilde{y}} = -1 \qquad 1 - \phi < \tilde{x} < 1, \quad \tilde{y} = 0 \tag{5.27}$$

$$\frac{\partial \tilde{T}_0}{\partial \tilde{y}} = -\phi \qquad 0 < \tilde{x} < 1, \qquad \tilde{y} \to \infty \tag{5.28}$$

$$\frac{\partial \tilde{T}_0}{\partial x} = 0 \qquad \tilde{x} = 0, \qquad \tilde{y} > 0 \tag{5.29}$$

$$\frac{\partial \tilde{T}_0}{\partial x} = 0 \qquad \tilde{x} = 1, \qquad \tilde{y} > 0 \tag{5.30}$$

Taking $\tilde{u}(\tilde{x}, \tilde{y}) = \tilde{T}_0 + \phi \tilde{y}$ the system becomes

$$\nabla^2 \tilde{u} = 0 \tag{5.31}$$

subjected to

$$\frac{\partial \tilde{u}}{\partial \tilde{y}} = \phi \qquad 0 < \tilde{x} < 1 - \phi, \quad \tilde{y} = 0 \tag{5.32}$$

$$\frac{\partial \tilde{u}}{\partial \tilde{y}} = \phi - 1 \qquad 1 - \phi < \tilde{x} < 1, \quad \tilde{y} = 0 \tag{5.33}$$

$$\frac{\partial \tilde{u}}{\partial \tilde{y}} = 0 \qquad 0 < \tilde{x} < 1, \qquad y \to \infty \tag{5.34}$$

$$\frac{\partial \tilde{u}}{\partial \tilde{x}} = 0 \qquad \tilde{x} = 0, \qquad \tilde{y} > 0 \tag{5.35}$$

$$\frac{\partial \tilde{u}}{\partial \tilde{x}} = 0 \qquad \tilde{x} = 1, \qquad \tilde{y} > 0 \tag{5.36}$$

Applying the last three boundary conditions the solution takes the form

$$\tilde{u} = \sum_{n=0}^{\infty} a_n e^{-n\pi\tilde{y}} \cos\left(n\pi\tilde{x}\right). \tag{5.37}$$

Applying the boundary conditions at the composite interface, results in

$$\sum_{n=1}^{\infty} - n\pi a_n \cos\left(n\pi\tilde{x}\right) = \phi \qquad 0 < \tilde{x}, 1-\phi \tag{5.38}$$

$$\sum_{n=1}^{\infty} - n\pi a_n \cos\left(n\pi\tilde{x}\right) = \phi - 1 \qquad 1-\phi < \tilde{x} < 1. \tag{5.39}$$

Applying orthogonality and adding the equations together results in

$$\int_0^1 -n\pi a_n \cos^2\left(n\pi\tilde{x}\right) d\tilde{x} = \phi \int_0^1 \cos\left(n\pi\tilde{x}\right) d\tilde{x} - \int_{1-\phi}^1 \cos\left(n\pi\tilde{x}\right) d\tilde{x} \tag{5.40}$$

which is solved to find the coefficients

$$a_n = -2\frac{\sin\left(n\pi(1-\phi)\right)}{n^2\pi^2} \tag{5.41}$$

The temperature profile is

$$\tilde{T}_0 = -\phi\tilde{y} - \frac{2}{\pi^2}\sum_{n=1}^{\infty}\frac{1}{n^2} e^{-n\pi\tilde{y}} \sin\left(n\pi(1-\phi)\right)\cos\left(n\pi\tilde{x}\right). \tag{5.42}$$

Enright et al. [29] provide an expression for apparent thermal slip length which is adapted from Mikic and Rohsenow [99] who solved the system of Eq. 5.25 in the context of a thermal spreading resistance. The apparent thermal slip length associated with T_0 is found from

$$\tilde{b}_{t,0} = \frac{(\bar{T}_{0,sl} - \bar{T}_{0,\infty})}{2\,\partial\tilde{T}/\partial\tilde{y}\Big|_{y=0}}. \tag{5.43}$$

It follows that

$$\tilde{b}_{t,0} = \sum_{n=1}^{\infty} \frac{\sin^2(n\pi(\phi-1))}{\phi^2 n^3 \pi^3}. \tag{5.44}$$

5.3.3 Isoflux Ridge "Curved" Meniscus

The correction to the temperature field in the presence of deflection of the meniscus is $\tilde{T}_1$. Noting from Eq. 5.9 earlier that $\tilde{T} = \tilde{T}_0 + \tilde{\varepsilon}\tilde{T}_1$. It is the solution of the following system

$$\nabla^2 \tilde{T}_1 = 0 \tag{5.45}$$

subjected to Eq. 5.13 and the following

$$\frac{\partial \tilde{T}_1}{\partial \tilde{y}} = 0 \quad 1-\phi < \tilde{x} < 1, \tilde{y} = 0 \tag{5.46}$$

$$\frac{\partial \tilde{T}_1}{\partial \tilde{y}} = 0 \quad 0 < \tilde{x} < 1, \qquad \tilde{y} \to \infty \tag{5.47}$$

$$\frac{\partial \tilde{T}_1}{\partial \tilde{x}} = 0 \quad \tilde{x} = 0, \qquad \tilde{y} > 0 \tag{5.48}$$

$$\frac{\partial \tilde{T}_1}{\partial \tilde{x}} = 0 \quad \tilde{x} = 1, \qquad \tilde{y} > 0. \tag{5.49}$$

Applying the last three boundary conditions leads to

$$\tilde{T}_1 = \sum_{n=0}^{\infty} g_n e^{-n\pi\tilde{y}} \cos(n\pi\tilde{x}.) \tag{5.50}$$

Applying Eqs. 5.13 and 5.46 results in the dual series

$$\sum_{n=1}^{\infty} -n\pi g_n \cos(n\pi\tilde{x}) = f(\tilde{x}) \quad 0 < \tilde{x} < 1-\phi \tag{5.51}$$

$$\sum_{n=1}^{\infty} n\pi g_n \cos(n\pi\tilde{x}) = 0 \quad 1-\phi < \tilde{x} < 1 \tag{5.52}$$

where

$$f(\tilde{x}) = \sum_{n=1}^{\infty} \left\{ \frac{4}{n\pi} \tilde{x} \sin[n\pi\tilde{x}] \sin[n\pi(1-\phi)] \right\}. \tag{5.53}$$

Using orthogonality and combining Eqs. 5.51 and 5.52 results in

$$\begin{aligned} &\int_0^1 -m\pi g_m \cos^2(m\pi\tilde{x}) d\tilde{x} = \\ &+ \sum_{n=1}^{\infty} \frac{4}{n\pi} \sin(n\pi(1-\phi)) \int_0^{1-\phi} \tilde{x} \sin(n\pi\tilde{x}) \cos(m\pi\tilde{x}) \, d\tilde{x} \end{aligned} \tag{5.54}$$

The coefficients, g_m, are found from the above. For $m \neq n$

$$\begin{aligned} g_m = \sum_{n=1}^{\infty} -\frac{4}{mn\pi^4} \sin[n\pi(1-\phi)] \Bigg\{ & \frac{\pi(\phi-1)\cos[(m+n)\pi(\phi-1)]}{(m+n)} \\ &+ \frac{\sin[(m+n)\pi(1-\phi)]}{(m+n)^2} \\ &+ \frac{\pi(1-\phi)\cos[(m-n)\pi(\phi-1)]}{(m-n)} \\ &+ \frac{\sin[(m-n)\pi(\phi-1)]}{(m-n)^2} \Bigg\}. \end{aligned} \tag{5.55}$$

When $m = n$ the following term is used in the above sum

$$\begin{aligned} g_m = \frac{4}{mn(m+n)^2\pi^4} \sin[n\pi(1-\phi)] \Bigg\{ & \\ &+ (m+n)\pi(1-\phi)\cos[(m+n)\pi(\phi-1)] \\ &+ \sin[(m+n)\pi(\phi-1)] \Bigg\}. \end{aligned} \tag{5.56}$$

The contribution to thermal slip length associated with the deflection of the meniscus is found from

$$\tilde{\varepsilon}\tilde{b}_{t,1} = \frac{\tilde{\varepsilon}(\bar{T}_{1,sl} - \bar{T}_{1,\infty})}{2\partial\tilde{T}/\partial\tilde{y}\Big|_{y=0}}. \tag{5.57}$$

It follows that

$$\tilde{b}_{t,1} = \sum_{m=1}^{\infty} \frac{g_m \sin(m\pi(-1+\phi))}{2m\pi\phi^2}. \tag{5.58}$$

The total apparent thermal slip associated with a small deflection of the meniscus in an infinite domain with a constant heat flux boundary condition is

$$\tilde{b}_t = \tilde{b}_{t,0} + \tilde{\varepsilon}\tilde{b}_{t,1} \tag{5.59}$$

which yields

$$\tilde{b}_t = \sum_{m=1}^{\infty} \frac{\sin^2(m\pi(\phi-1))}{\phi^2 m^3 \pi^3} + \frac{g_m \tilde{\varepsilon} \sin(m\pi(-1+\phi))}{2m\pi\phi^2}. \tag{5.60}$$

5.4 Results

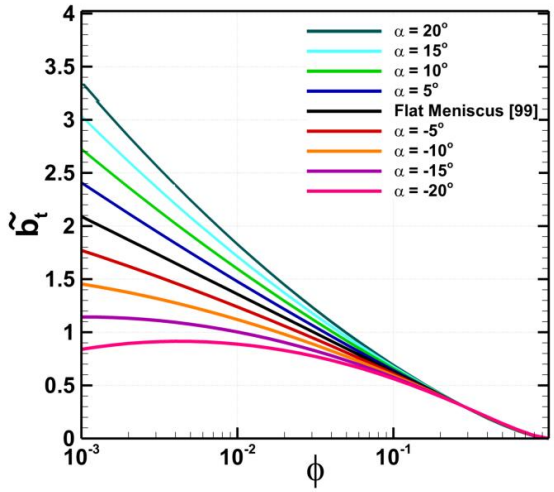

Figure 5.3: Dimensionless thermal slip length versus solid fraction, ϕ, for selected protrusion angles, α.

Thermal slip length versus solid fraction is plotted in Fig. 5.3 for a flat meniscus and for a range of positive and negative protrusion angles. Negative angles reduce the thermal slip length resulting in enhancement to heat transfer. Positive protrusion angles increase the thermal slip length resulting in reductions to heat transfer. Figure 5.4 shows thermal slip

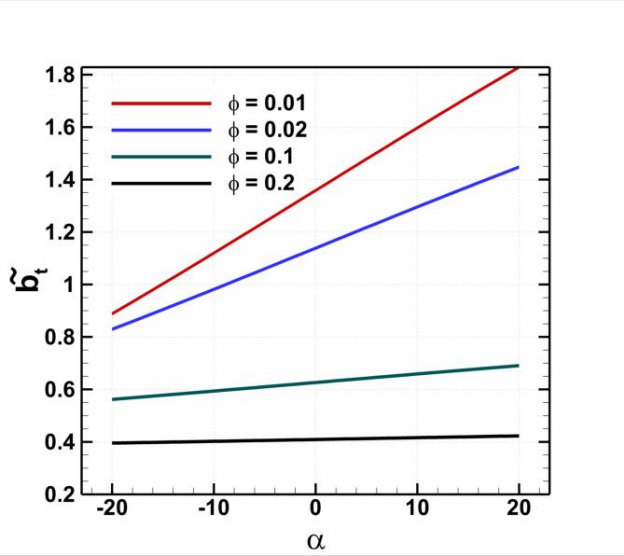

Figure 5.4: Dimensionless thermal slip length versus protrusion angle, α, for selected solid fractions, ϕ.

length as a function of protrusion angle for selected solid fractions. Notably, the slip length is more sensitive to protrusion angle for low solid fractions. This highlights the importance of accounting for the effect of curvature on heat transfer in at low solid fractions which are typical of many applications.

Model Validation

The Partial Differential Equation (PDE) Toolbox in MATLAB was used to validate the results. The Laplace equation with relevant boundary conditions was solved with a finite element solver. The flow domain was discretized on average with 440,000 elements. Slip length results from this model were first compared to the analytical slip length for the flat meniscus and to comparable FLUENT simulations. The slip length from the PDE Toolbox was found to match the known flat meniscus slip length to 5 decimal places; therefore, it was used to evaluate the analytical values in order to determine the range of angles and solid fractions over which the analytical results are valid. The mesh at each case was adapted and refined multiple times for both the MATLAB and the FLUENT simulations to ensure mesh independence.

Solid Fraction	Protrusion Angle [°]	Perturbation Thermal Slip length	Numerical Thermal Slip length	Percent Error
0.1	-20	0.567806	0.575841	-1.395
0.1	-10	0.593614	0.598399	-0.800
0.1	-5	0.609875	0.611573	-0.278
0.1	0	0.626259	0.626254	0.001
0.1	5	0.642645	0.642654	-0.001
0.1	10	0.658906	0.661039	-0.323
0.1	20	0.684714	0.705070	-2.887

Table 5.1: Comparison of perturbation method values with numerical values.

Table 5.1 compares slip length values obtained from the perturbation method with those obtained from the PDE Toolbox. The perturbation results for negative angles have lower error than those with corresponding positive angles. This highlights the asymmetry of the thermal slip length between positive and negative angles which is not captured in the perturbation method. For angles between $\pm 20°$, and solid fractions below 0.1, values that are typical for water-based cooling, the error is less than 3%. Figure 5.5 shows the validated data points on the slip length curves. As $|\alpha|$ increases, $\tilde{\varepsilon}$ increases and $\tilde{\varepsilon}$ is an indication of the magnitude of error to be expected. As ϕ decreases, $\tilde{\varepsilon}$ decreases; therefore the error associated with lower values of ϕ will be lower.

5.5 Conclusions

A thermal slip length expression has been developed for flow across parallel ridges which accounts for the change in thermal resistance associated with the presence of a curved meniscus. It is applicable for a range of small protrusion angles and solid fractions which are typical of water-based cooling in a microchannel. When liquid pressure is higher than that of the

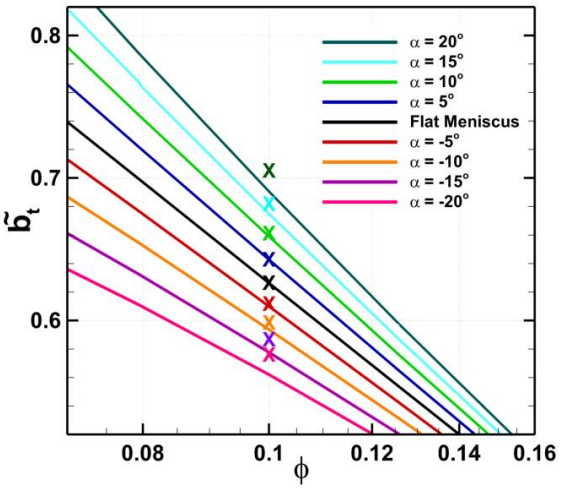

Figure 5.5: Dimensionsless slip length versus solid fraction. Solid lines correspond to perturbation method results, X's correspond to numerical validation results from MATLAB.

gas, a negative protrusion angle exists and heat transfer is enhanced. Conversely, the presence of bubble mattresses formed because the pressure in the gas is higher than that of the liquid will reduce heat transfer to the liquid at low protrusion angles.

Future work will develop thermal slip lengths for constant temperature boundary conditions and over a wider range of protrusion angles and solid fractions.

5.6 Acknowledgements

Funding for this research was provided in part by the NSF CBET award no. 1402783. The authors gratefully acknowledge Durwood Marshall and Shawn Doughty of Tufts Technology Services for their assistance and access to Tufts UIT Research Computing facilities.

Chapter VI

Conclusions and Future Work

6.1 Conclusions

In this work we have developed expressions and methods to assess heat transfer across structured surfaces. In Chapters 2 and 3, we present results for shear-driven and pressure-driven channel flows. In Chapters 4 and 5, we develop slip length expressions which account for secondary effects. We find that the secondary effects studied here significantly impact the temperature field. Thus, they change the thermal resistance between the structured surface and the outer flow and should be accounted for in the calculation of heat transfer to the flow.

6.1.1 Apparent slip in Couette flow

In Chapter 2, we provide expressions for temperature, bulk temperature and Nusselt number as a function of arbitrary *apparent* slip at the boundaries for a thermally developing steady laminar plane Couette flow with four sets of thermal boundary conditions. Fully developed Nusselt numbers can be calculated with only one eigenvalue for given values of *apparent* thermal and hydrodynamic slip and in one case, only the *apparent* slip values are needed.

For a Couette flow, we find that the presence of *apparent* hydrodynamic slip at the moving surface has no influence on Nusselt number, and the presence of *apparent* hydrodynamic slip

at the stationary surface enhances heat transfer at the stationary surface but decreases heat transfer at the moving surface. In all cases, the presence of *apparent* thermal slip lowers the Nusselt number relative to the no slip case. When *apparent* thermal slip is present at the moving surface in Couette flow, the reduction in heat transfer is more pronounced than for *apparent* thermal slip at the stationary surface.

6.1.2 Liquid cooling in a microgap

In Chapter 3, we show that galinstan-based micro/minigap coolers are a promising alternative to water-based single phase cooling. We have demonstrated that, for fully developed laminar flows with constant slip coefficients, significant reductions in thermal resistance are possible, particularly for systems that are pressure limited.

We provide a methodology for assessing heat transfer enhancement resulting from *apparent* slip. We show that by considering both the caloric and convection contributions to heat transfer, substantial reductions in thermal resistance can be achieved by incorporating structured surfaces into a microgap surface, and the extent of the reduction depends on channel and surface geometry.

We also find that when the working fluid is galinstan, the convective thermal resistance is a small percentage of the total thermal resistance and that galinstan-based cooling is calorically dominated both in a classic channel and a channel lined with structured surfaces. Notably, the enhancement to heat transfer gained from drag reduction in the galinstan-based system outweighs the reduction in convective heat transfer resulting in a net improvement.

We also consider the presence of an entrance length, and while caloric resistance is increased by comparison to a fully developed flow, structured surfaces still show significant enhancement to heat transfer. The caloric resistance is 25% lower in the structured surface channel than in the classic channel when the entrance length is taken into account. Additionally, we consider the effect of non-constant thermophysical properties. Since the effect of temperature on the thermophysical properties of galinstan has not been studied, we use

the properties of a terniary alloy whose composition is comparable to galinstan to assess the the effect of the temperature dependence of thermophysical properties on heat transfer. The percent change in both the alloy and water for a 20°C increase is comparable; notably, the caloric resistance in galinstan is 22% lower than water at the higher temperature.

We discuss several methods to assess the effect on transport due to the addition of structured surfaces. First, we develop a dimensionless expression called the Navier-Laplace parameter which allows the comparison of surface geometries to optimize the trade-off between pressure stability and hydrodynamic slip. Using this we show that parallel ridges have the best performance with regard to drag reduction. Second, the additional height of structures reduces the available channel cross-sectional area and adds an additional resistance to the heat transfer path. This is taken into account, first, in an analysis of the impact to the volumetric flow. A minimum value of $\tilde{b} \geq 0.04$ is required for velocity enhancement in the galinstan system constraining both the classic and structured-surface channels to fit into the same available height. Subsequently, an analysis of the thermal resistance through the surface structures shows $R_{Ridge} = 0.0083\,^{\circ}\mathrm{C/W}$ which is small compared to the total and on the same order as the convective resistance for the galinstan system.

6.1.3 Effect of Evaporation and Condensation at Menisci on Apparent Thermal Slip

In Chapter 4, we develop expressions for the dimensionless *apparent* thermal slip length for liquid flow in the Cassie state over ridge-type structured surfaces in the presence of local evaporation and condensation. The net rate of phase change along the meniscus is constrained to be zero. An isoflux boundary condition is imposed at the solid-liquid interface. In the limiting case of an isothermal meniscus, analytical results provide thermal slip length as a function of solid fraction. In the case of a finite heat transfer coefficient along the meniscus, semi-analytical results provide thermal slip length as a function of solid fraction and dimensionless interfacial heat transfer coefficient. Evaporation and condensation substan-

tially reduce thermal slip lengths at conditions relevant to water-based thermal management of electronics. The reduction in thermal resistance of a microchannel heat sink may be quantified by using *apparent* thermal slip lengths computed from the present analysis in relevant Nusselt number expressions.

6.1.4 Effect of Meniscus Curvature on Apparent Thermal Slip

In Chapter 5, we develop a thermal slip length expression for flow across parallel ridges which accounts for the change in thermal resistance associated with the presence of a curved meniscus. Although an approximate method (perturbation) is used, the results are quite accurate for a range of protrusion angles, $-20^\circ \leq \alpha \leq 20^\circ$ and solid fractions, $\phi_s \leq 0.1$, which are typical of water-based cooling in a microchannel. When liquid pressure is higher than that of the gas, a negative protrusion angle exists and heat transfer is enhanced. Conversely, the presence of bubble mattresses formed because the pressure in the gas is higher than that of the liquid will reduce heat transfer to the liquid at low protrusion angles.

6.2 Future Work

Building on the results presented here, there are open questions and many opportunities for further analytical, numerical and experimental studies.

6.2.1 Apparent slip in Couette flow

An experimental investigation of Couette flow could be conducted to find Nusselt number values. Case C, where the stationary surface is patterned with ridges and held at constant temperature and the moving surface is adiabatic, would likely be the most tractable experimentally. Also, within the viscous sublayer of a turbulent flow, the viscous shear rate is approximated as constant as in the case of the Couette flow considered here. Since flow and heat transfer in the viscous sublayer play major roles in turbulent flows, the results of Chapter 2 may be relevant in elucidating the physics of turbulent flows over structured

surfaces. An analytical study of the heat transfer in the viscous sublayer where the wall is lined with parallel ridges could be undertaken. Lastly, numerical modeling of a plane steady Couette flow where the walls are lined with structured surfaces could be undertaken and Nusselt number values could be compared to analytical results.

6.2.2 Liquid cooling in a microgap

Future studies of microgap cooling should focus on running experiments in pressure-driven galinstan flows in channels lined with parallel ridges. The present work found that conditions favoring the Cassie state could be maintained when the channel was widened and the galinstan flow transitioned to a turbulent regime. Experimental studies could be done to quantify heat transfer both in the laminar and turbulent regimes and determine if the Cassie state can be maintained in a turbulent regime and to what extent.

Also the methodology presented here could be extended to explore an optimum geometry for water-based cooling of a microchannel lines with structured surfaces. The approach should quantify conjugate heat transfer as was done by Hodes et al. [69] in combination with the analysis which includes the wetting interactions required to maintain the Cassie state.

6.2.3 Secondary Effects at Menisci

There are several directions which could be taken for further analytical study of effects of evaporation and condensation. First, channel level modeling of heat transfer to the flow should be done to include a liquid-vapor interface temperature that changes with the streamwise coordinate. The heat transfer coefficient used for slip length calculation is a function of liquid-vapor interface temperature and the slip length could be calculated accordingly. Second, consideration of higher rates of interfacial heat flux than allowed by Eq. 4.59 could be incorporated into the analysis done here. This would further complicate the Robin boundary condition due to the use of an $\tilde{h}$ which varies along the meniscus and a method to handle this

would need to be developed. Third, the mass transfer which occurs during evaporation and condensation implies a non-zero velocity normal to the meniscus, its effect on hydrodynamic slip should be explored. Finally, a study of an open system where net heat transfer across the meniscus exists would be a valuable contribution to the understanding of heat transfer across structured surfaces.

There are also several opportunities for further analytical work regarding the effect of meniscus curvature. Future work should develop thermal slip lengths for constant temperature boundary conditions and over a wider range of protrusion angles and solid fractions. Additionally, the radius of curvature of the meniscus will vary with the pressure drop along the channel. A channel level study which accounts for this change in curvature should be undertaken.

The effect of thermocapillary stress was not considered here and may potentially alter hydrodynamic slip lengths. Thermocapillary stresses arise due to the dependence of surface tension on temperature. Consequently, the temperature field affects the flow field adjacent to the liquid-gas interface. Additionally, the effect of temperature dependence of the surface tension on the shape of the meniscus could be studied as this may potentially change hydrodynamic and thermal slip lengths.

Future work should consider extending the slip length results for secondary effects to other geometries.

A numerical study which incorporates the three secondary effects mentioned above could be done on the scale of the microstructures or on the level of a channel flow. Additionally, future work should also consider addressing heat transfer in the presence of *apparent* slip in a turbulent regime. This would be applicable to using galinstan as a working fluid in a microgap and also facilitate the evaluation of the effect of *apparent* slip in large channels.

BIBLIOGRAPHY

[1] D. Quéré, "Non-sticking drops," *Reports on Progress in Physics*, vol. 68, pp. 2495–2532, Nov. 2005.

[2] E. N. Wang, M. a. Bucaro, J. A. Taylor, P. Kolodner, J. Aizenberg, and T. Krupenkin, "Droplet mixing using electrically tunable superhydrophobic nanostructured surfaces," *Microfluidics and Nanofluidics*, vol. 7, no. 1, pp. 137–140, 2008.

[3] L. S. Lam, M. Hodes, and R. Enright, "Analysis of galinstan-based microgap cooling enhancement using structured surfaces," To Appear in *Journal of Heat Transfer, Special Issue on Micro/Nanoscale Heat and Mass Transfer*, 2014.

[4] V. A. Lifton, J. A. Taylor, B. Vyas, P. Kolodner, R. Cirelli, N. Basavanhally, A. Papazian, R. Frahm, S. Simon, and T. Krupenkin, "Superhydrophobic membranes with electrically controllable permeability and their application to smart microbatteries," *Applied Physics Letters*, vol. 93, no. 4, p. 043112, 2008.

[5] A. B. D. Cassie and S. Baxter, "Wettability of porous surfaces," *Trans. Faraday Soc.*, vol. 40, pp. 546–551, 1944.

[6] M. Gad-el Hak, *The MEMS handbook*, vol. 17. CRC Press Llc, 2002.

[7] C. Navier, "Mémoire sur les du mouvement des fluids.," *Mémoires de l'Académie Royale des Sciences de l'Institut de France*, vol. 6, pp. 389–440, 1823.

[8] E. H. Kennard, *Kinetic Theory of Gases*. McGraw Hill Book Company, first ed., 1938.

[9] J. C. Maxwell, *Scientific papers*. Dover Publications, 1965.

[10] E. Sparrow and S. Lin, "Laminar Heat Transfer in tubes under slip flow conditions," *Journal of Heat Transfer*, pp. 362–369, 1962.

[11] L. M. Jiji, *Heat Convection*. Springer-Verlag, second ed., 2009.

[12] S. Colin, "Gas Microflows in the Slip Flow Regime: A Critical Review on Convective Heat Transfer," *Journal of Heat Transfer*, vol. 134, no. 2, p. 020908, 2012.

[13] Y. Cheng, C. Teo, and B. Khoo, "Microchannel flows with superhydrophobic surfaces: Effects of reynolds number and pattern width to channel height ratio," *Physics of Fluids*, vol. 21, p. 122004, 2009.

[14] J. P. Rothstein, "Slip on superhydrophobic surfaces," *Annual Review of Fluid Mechanics*, vol. 42, no. 1, pp. 89–109, 2010.

[15] J. Philip, "Flows satisfying mixed no-slip and no-shear conditions," *Journal of Applied Mathematics and Physics (ZAM P)*, vol. 23, pp. 353–372, 1972.

[16] J. Philip, "Integral properties of flows satisfying mixed no-slip and no-shear conditions," *Journal of Applied Mathematics and Physics (ZAM P)*, vol. 23, pp. 960–968, 1972.

[17] E. Lauga and H. Stone, "Effective slip in pressure-driven Stokes flow," *Journal of Fluid Mechanics*, vol. 489, pp. 55–77, 2003.

[18] J. Ou, B. Perot, and J. P. Rothstein, "Laminar drag reduction in microchannels using ultrahydrophobic surfaces," *Physics of Fluids*, vol. 16, no. 12, p. 4635, 2004.

[19] J. Ou and J. Rothstein, "Direct velocity measurements of the flow past drag-reducing ultrahydrophobic surfaces," *Physics of Fluids*, vol. 17, p. 103606, 2005.

[20] N. V. Priezjev, A. A. Darhuber, and S. M. Troian, "Slip behavior in liquid films on surfaces of patterned wettability," *Physical Review E*, vol. 71, p. 041608, 2005.

[21] R. Truesdell, A. Mammoli, P. Vorobieff, F. van Swol, and C. Brinker, "Drag Reduction on a Patterned Superhydrophobic Surface," *Physical Review Letters*, vol. 97, no. 4, pp. 1–4, 2006.

[22] C. Lee, C.-H. Choi, and C.-J. Kim, "Structured Surfaces for a Giant Liquid Slip," *Physical Review Letters*, vol. 101, no. 6, pp. 1–4, 2008.

[23] C. Ybert, C. Barentin, C. Cottin-Bizonne, P. Joseph, and L. Bocquet, "Achieving large slip with superhydrophobic surfaces: Scaling laws for generic geometries," *Physics of Fluids*, vol. 19, no. 12, p. 123601, 2007.

[24] T. Salamon, W. Lee, M. Hodes, P. Kolodner, R. Enright, and A. Salinger, "Numerical simulation of fluid flow in microchannels with superhydrophobic walls," in *IMECE Conference Proceedings*, no. 42215, pp. 819–829, ASME, 2005.

[25] D. Maynes, K. Jeffs, B. Woolford, and B. W. Webb, "Laminar flow in a microchannel with hydrophobic surface patterned microribs oriented parallel to the flow direction," *Physics of Fluids*, vol. 19, no. 9, p. 093603, 2007.

[26] J. Davies, D. Maynes, B. W. Webb, and B. Woolford, "Laminar flow in a microchannel with superhydrophobic walls exhibiting transverse ribs," *Physics of Fluids*, vol. 18, no. 8, p. 087110, 2006.

[27] C. J. Teo and B. C. Khoo, "Flow past superhydrophobic surfaces containing longitudinal grooves: effects of interface curvature," *Microfluidics and Nanofluidics*, vol. 9, no. 2-3, pp. 499–511, 2010.

[28] A. Steinberger, C. Cottin-Bizonne, P. Kleimann, and E. Charlaix, "High friction on a bubble mattress.," *Nature materials*, vol. 6, no. 9, pp. 665–8, 2007.

[29] R. Enright, M. Hodes, T. Salamon, and Y. Muzychka, "Isoflux Nusselt number and slip length formulae for superhydrophobic microchannels," *Journal of Heat Transfer*, vol. 136, no. 1, 2014.

[30] R. Enright, M. Hodes, T. Salamon, T. Krupenkin, P. Kolodner, T. Dalton, and C. Eason, "Friction Factors and Nusselt Numbers in Microchannels With Superhydrophobic Walls," in *Proceedings of the Fourth International Conference on Nanochannels, Microchannels and Minichannels, Limerick Ireland, ASME, ICNMM2006-96134*, pp. 599–609, 2006.

[31] D. Maynes, B. W. Webb, and J. Davies, "Thermal Transport in a Microchannel Exhibiting Ultrahydrophobic Microribs Maintained at Constant Temperature," *Journal of Heat Transfer*, vol. 130, no. 2, p. 022402, 2008.

[32] D. Maynes, B. Webb, J. Crockett, and V. Solovjov, "Analysis of laminar slip-flow thermal transport in microchannels with transverse rib and cavity structured superhydrophobic walls at constant heat flux," *Journal of heat transfer*, vol. 135, no. 2, p. 021701, 2013.

[33] D. Maynes and J. Crockett, "Apparent Temperature Jump and Thermal Transport in Channels With Streamwise Rib and Cavity Featured Superhydrophobic Walls at Constant Heat Flux," *Journal of Heat Transfer*, vol. 136, no. 1, 2014.

[34] R. M. Inman, "Laminar Slip Flow Heat Transfer In A Parallel-Plate Channel or A Round Tube with Uniform Wall Heating," *NASA Technical Note D-2393*, 1964.

[35] M. M. Yovanovich, "Spreading resistance of isoflux rectangles and strips on compound flux channles," *Journal of Thermophysics and Heat Transfer*, vol. 13, no. 4, p. 495, 1999.

[36] C.-O. Ng and C. Y. Wang, "Temperature Jump Coefficient for Superhydrophobic Surfaces," *Journal of Heat Transfer*, vol. 136, no. 6, p. 064501, 2014.

[37] V. P. Carey, *Liquid-Vapor Phase-Change Phenomena.* Hemisphere, New York, NY (United States), 1992.

[38] R. W. Schrage, *A Theoretical Study of Interphase Mass Transfer.* Columbia University Press, 1953.

[39] R. Enright, N. Miljkovic, A. Al-Obeidi, C. V. Thompson, and E. N. Wang, "Condensation on superhydrophobic surfaces: the role of local energy barriers and structure length scale.," *Langmuir: The ACS Journal of Surfaces and Colloids*, vol. 28, no. 40, pp. 14424–32, 2012.

[40] K. Rykaczewski, "Microdroplet Growth Mechanism during Water Condensation on Superhydrophobic Surfaces," *Langmuir: the ACS journal of surfaces and colloids*, vol. 28, no. 20, pp. 7720–7729, 2012.

[41] N. Miljkovic, R. Enright, and E. N. Wang, "Effect of droplet morphology on growth dynamics and heat transfer during condensation on superhydrophobic nanostructured surfaces.," *ACS nano*, vol. 6, no. 2, pp. 1776–85, 2012.

[42] L. Bocquet and J.-L. Barrat, "Flow boundary conditions from nano- to micro-scales," *Soft Matter*, vol. 3, no. 6, p. 685, 2007.

[43] M. Sbragaglia and A. Prosperetti, "A note on the effective slip properties for microchannel flows with ultrahydrophobic surfaces," *Physics of Fluids*, vol. 19, no. 4, p. 043603, 2007.

[44] J. Hyväluoma and J. Harting, "Slip Flow Over Structured Surfaces with Entrapped Microbubbles," *Physical Review Letters*, vol. 100, no. 24, p. 246001, 2008.

[45] D. Crowdy, "Slip length for longitudinal shear flow over a dilute periodic mattress of protruding bubbles," *Physics of Fluids*, vol. 22, no. 12, p. 121703, 2010.

[46] A. M. J. Davis and E. Lauga, "Geometric transition in friction for flow over a bubble mattress," *Physics of Fluids*, vol. 21, no. 1, p. 011701, 2009.

[47] C. J. Teo and B. C. Khoo, "Effects of interface curvature on Poiseuille flow through microchannels and microtubes containing superhydrophobic surfaces with transverse grooves and ribs," *Microfluidics and Nanofluidics*, 2014.

[48] C.-O. Ng and C. Y. Wang, "Stokes shear flow over a grating: Implications for superhydrophobic slip," *Physics of Fluids*, vol. 21, no. 1, p. 013602, 2009.

[49] D. Tuckerman and R. Pease, "High-performance heat sinking for vlsi," *Electron Device Letters, IEEE*, vol. 2, no. 5, pp. 126–129, 1981.

[50] R. J. Phillips, "Microchannel Heat Sinks," *The Lincoln Laboratory Journal*, vol. 1, no. 1, pp. 31–48, 1988.

[51] D. Liu and S. V. Garimella, "Investigation of Liquid Flow in Microchannels," *Journal of Thermophysics and Heat Transfer*, vol. 18, no. 1, pp. 65–72, 2004.

[52] P.-S. Lee, S. V. Garimella, and D. Liu, "Investigation of heat transfer in rectangular microchannels," *International Journal of Heat and Mass Transfer*, vol. 48, no. 9, pp. 1688–1704, 2005.

[53] J. Li and G. Peterson, "3-Dimensional numerical optimization of silicon-based high performance parallel microchannel heat sink with liquid flow," *International Journal of Heat and Mass Transfer*, vol. 50, no. 15-16, pp. 2895–2904, 2007.

[54] G. Vogelpohl, "Die Temperaturverteilung in Schmierschichten zwishen parallen warmendurchlassigen Wanden," *Zeitschrift fur angewandte Mathematik und Mechanik*, vol. 31, pp. 349–356, 1951.

[55] J. Hudson and S. Bankoff, "Heat transfer to a steady Couette flow with pressure gradient," *Chemical Engineering Science*, vol. 20, no. 5, pp. 415–423, 1965.

[56] S. Bruin, "Temperature distributions in Couette flow with and without additional pressure," *Int. Journal Heat and Mass Transfer*, vol. 15, pp. 341–349, 1972.

[57] E. J. Davis, "Exact Solutions for a Class of Heat and Mass transfer problems," *Canadian Journal of Chemical Engineering*, vol. 51, pp. 562–572, 1973.

[58] A. El-Ariny and A. Aziz, "A numerical solution of entrance region heat transfer in plane Couette flow," *Journal of Heat Transfer*, no. 76, pp. 427–431, 1976.

[59] J. Šesták and F. Rieger, "Laminar heat transfer to a steady Couette flow between parallel plates," *Int. Journal of Heat and Mass Transfer*, vol. 12, pp. 71–80, 1969.

[60] R. Schamberg, The fundamental differential equations and the boundary conditions for high speed slip-flow, and their application to several specific problems. PhD thesis, 1947.

[61] W. Marques Jr., G. Kremer, and F. Sharipov, "Couette flow with slip and jump boundary conditions," *Continuum Mechanics and Thermodynamics*, vol. 12, no. 6, pp. 379–386, 2000.

[62] Y. Fang and W. Liou, "Computations of the flow and heat transfer in microdevices using dsmc with implicit boundary conditions," *Journal of Heat Transfer-Transactions of the ASME*, vol. 124, pp. 338–345, 2002.

[63] F. Sharipov and J. L. Strapasson, "Benchmark problems for mixtures of rarefied gases. I. Couette flow," *Physics of Fluids*, vol. 25, no. 2, p. 027101, 2013.

[64] S. S. Milicev and N. D. Stevanovic, "A non-isothermal Couette slip gas flow," *Science China Physics, Mechanics and Astronomy*, vol. 56, no. 9, pp. 1782–1797, 2013.

[65] C. J. Teo and B. C. Khoo, "Analysis of Stokes flow in microchannels with superhydrophobic surfaces containing a periodic array of micro-grooves," *Microfluidics and Nanofluidics*, vol. 7, no. 3, pp. 353–382, 2008.

[66] B. Weigand, *Analytical Methods for Heat Transfer and Fluid Flow Problems*. Springer, 2004.

[67] R. Haberman, *Applied Partial Differential Equations with Fourier Series and Boundary Value Problems*. Pearson Prentice Hall, 4th ed., 2004.

[68] M. Greenberg, *Advanced Engineering Mathematics*. Prentice Hall, second ed., 1998.

[69] M. Hodes, R. Zhang, L. S. Lam, R. Wilcoxon, and N. Lower, "On the Potential of Galinstan-Based Minichannel and Minigap Cooling," *IEEE Transactions on Components, Packaging and Manufacturing Technology*, vol. 4, no. 1, pp. 46 – 56, 2014.

[70] R. M. Diagnostics, "Material safety data sheet for galinstan," 2006.

[71] L. C. Cadwallader, *Gallium safety in the laboratory*. Idaho National Laboratory, 2003.

[72] D. Evans and A. Prince, "Thermal analysis of ga-in-sn system," *Metal Science*, vol. 12, no. 9, pp. 411–414, 1978.

[73] T. Liu, P. Sen, C.-j. C. J. Kim, and A. C. A. Measurements, "Characterization of Nontoxic Liquid-Metal Alloy Galinstan for Applications in Microdevices," *Journal OF Microelectromechanical Systems*, vol. 21, no. 2, pp. 443–450, 2012.

[74] D. Quéré, "Wetting and Roughness," *Annual Review of Materials Research*, vol. 38, no. 1, pp. 71–99, 2008.

[75] C.-O. Ng and C. Wang, "Apparent slip arising from stokes shear flow over a bidimensional patterned surface," *Microfluidics and Nanofluidics*, vol. 8, no. 3, pp. 361–371, 2010.

[76] G. Rosengarten, C. Stanley, and F. Kwok, "Superinsulating Heat Transfer Surfaces for Microfluidic Channels," *Int. J. Transport. Phenomena*, vol. 10, pp. 293–306, 2008.

[77] E. M. Sparrow, T. S. Lundgren, and S. H. Lin, "Slip flow in the entrance region of a parallel plate channel," in *Proceedings of the Heat Transfer and Fluid Mechanics Institute*, pp. 223–238, 1962.

[78] E. M. Sparrow, S. H. Lin, and T. S. Lundgren, "Flow Development in the Hydrodynamic Entrance Region of Tubes and Ducts," *Physics of Fluids*, vol. 7, no. 3, p. 338, 1964.

[79] R. W. Barber and D. R. Emerson, "The influence of Knudsen number on the hydrodynamic development length within parallel plate micro-channels," *Advances in Fluid Mechanics IV*, pp. 207–216, 2002.

[80] Z. Duan and Y. S. Muzychka, "Slip flow in the hydrodynamic entrance region of circular and noncircular microchannels," *Journal of Fluids Engineering*, vol. 132, no. 1, p. 011201, 2010.

[81] E. Lemmon, M. McLinden, and D. Friend, "Thermophysical properties of fluid systems," in *NIST Chemistry WebBook, NIST Standard Reference Database Number 69* (P. Linstrom and W. Mallard, eds.), Gaithersburg, MD, 20899: National Institute of Standards and Technology. http://webbook.nist.gov, (retrieved August 31, 2011).

[82] V. Y. Prokhorenko, V. V. Roshchupkin, M. A. Pokrasin, S. V. Prokhorenko, and V. V. Kotov, "Liquid Gallium : Potential Uses as a Heat-Transfer Agent," *High Temperature*, vol. 38, no. 6, pp. 991–1005, 2000.

[83] Q.-S. Zheng, Y. Yu, and Z.-H. Zhao, "Effects of hydraulic pressure on the stability and transition of wetting modes of superhydrophobic surfaces.," *Langmuir: the ACS journal of surfaces and colloids*, vol. 21, no. 26, pp. 12207–12, 2005.

[84] E. J. Lobaton and T. R. Salamon, "Computation of constant mean curvature surfaces: Application to the gas-liquid interface of a pressurized fluid on a superhydrophobic surface.," *Journal of colloid and interface science*, vol. 314, no. 1, pp. 184–98, 2007.

[85] S. Moulinet and D. Bartolo, "Life and death of a fakir droplet: Impalement transitions on superhydrophobic surfaces," *The European Physical Journal E*, vol. 24, no. 3, pp. 251–260, 2007.

[86] A. Lafuma, D. Quere, *et al.*, "Superhydrophobic states," *Nature materials*, vol. 2, no. 7, pp. 457–460, 2003.

[87] A. Cassie and S. Baxter, "Wettability of porous surfaces," *Transactions of the Faraday Society*, vol. 40, pp. 546–551, 1944.

[88] R. Wenzel, "Resistance of solid surfaces to wetting by water," *Ind. Eng. Chem*, vol. 28, no. 8, pp. 988–994, 1936.

[89] D. Nield, "Forced convection in a parallel plate channel with asymmetric heating," *International Journal of Heat and Mass Transfer*, vol. 47, no. 25, pp. 5609–5612, 2004.

[90] W. R. Smythe, *Static and Dynamic Electricity*. New York: McGraw-Hill, 3rd ed., 1968.

[91] M. Yovanovich and E. Marotta, "Thermal spreading and contact resistances," in *Handbook of Heat Transfer* (A. Bejan and A. D. Kraus, eds.), pp. 261–394, John Wiley and Sons, 2003.

[92] R.-Y. Chen, "Flow in the entrance region at low Reynolds numbers," in *American Society of Mechanical Engineers, Winter Annual Meeting, New York, N. Y*, p. 1972, 1972.

[93] R. Shah and A. London, *Laminar flow forced convection in ducts*. Academic Press, 1978.

[94] M. Hodes, P. Kolodner, T. Krupenkin, W. Lee, A. Lyons, T. Salamon, J. Taylor, and D. Weiss, "Techniques for microchannel cooling," Apr. 17 2007. US Patent 7,204,298.

[95] A. M. J. Davis and E. Lauga, "Hydrodynamic friction of fakir-like superhydrophobic surfaces," *Journal of Fluid Mechanics*, vol. 661, pp. 402–411, 2010.

[96] A. Cowley, D. Maynes, and J. Crockett, "Effective temperature jump length and influence of axial conduction for thermal transport in superhydrophobic channels," *International Journal of Heat and Mass Transfer*, vol. 79, pp. 573–583, 2014.

[97] M. Hodes, L. Steigerwalt Lam, and S. MacLachlan, "Effect of evaporation and condensation at menisci on apparent thermal slip," Under Review *Journal of Heat Transfer*, 2014.

[98] F. M. White and I. Corfield, *Viscous fluid flow*, vol. 3. McGraw-Hill New York, 1991.

[99] B. B. Mikic and W. M. Rohsenow, "Thermal contact resistance," tech. rep., MIT Dept. of Mechanical Engineering, Cambridge, MA, 1966.

[100] L. Steigerwalt Lam, C. Melnick, M. Hodes, G. Ziskind, and R. Enright, "Nusselt Numbers for Thermally Developing Couette Flow With Hydrodynamic and Thermal Slip," *Journal of Heat Transfer*, vol. 136, no. 5, p. 051703, 2014.

[101] Y. Cheng, J. Xu, and Y. Sui, "Numerical study on drag reduction and heat transfer enhancement in microchannels with superhydrophobic surfaces for electronic cooling," *Applied Thermal Engineering*, pp. 1–11, 2014.